Helically confined Charged Particles: Dynamics and Vibrational Band Structure

Dissertation

zur Erlangung des Doktorgrades

an der Fakultät für Mathematik,

Informatik und Naturwissenschaften,

der Universität Hamburg,
Fachbereich Physik

vorgelegt von

Alexandra Zampetaki

geboren am 13.02.1990 in Athen

Hamburg

2015

Tag der Disputation: 09.02.2016

Folgende Gutachter empfehlen die Annahme der Dissertation:

Erstgutachter: Herr Prof. Dr. Peter Schmelcher
Zweitgutachter: Herr Prof. Dr. Michael Potthoff

To the memory of my grandmother Olympia

Zusammenfassung

In dieser Arbeit werden die dynamischen und Gleichgewichtseigenschaften identisch geladener Teilchen, deren Bewegung auf helixartige Mannigfaltigkeiten eingeschränkt ist, untersucht. Ausgehend von dem trivialen Fall der Einschränkung auf ein Liniensegment, untersuchen wir die statistischen Eigenschaften des Vielteilchensystems. Wir identifizieren einen Übergang von einer kristallinen zu einer clusterartigen Phase bei steigender Temperatur und ein nichtextensives Verhalten der thermodynamischen Funktionen, begründet durch den langreichweitigen Charakter der Wechselwirkung. Wird die Fallengeometrie nichttrivial, ergibt sich eine fundamentale Änderung der Zweikörperwechselwirkung, die im Fall der Einschränkung auf eine homogene Helix eine oszillatorische Form annimmt, was die Entstehung gebundener Paare ermöglicht. Für eine inhomogene helikale Falle koppeln die Schwerpunkts- und Relativbewegung zweier Ladungen und induzieren einen Energietransfer zwischen der kollektiven und der relativen Bewegung, was die Aufspaltung eines anfänglich gebundenen Zustands in einem Streuprozess ermöglicht. Im Vielkörperproblem führt die Einschränkung gleichartiger geladener Teilchen auf eine geschlossene Helix zur Entstehung verschiedener Gleichgewichtszustände. Bei verträglichen Füllungsfaktoren verursacht eine Vergrößerung des Helixradius eine Pitchfork-Bifurkation des Grundzustands von einer symmetrischen Polygonanordnung zu einer zickzackartigen Konfiguration. Bemerkenswerterweise bewirkt die Veränderung des Helixradius unterhalb des Bifurkationspunkts eine unkonventionelle Verformung des Vibrationsspektrums, wobei nacheinander Parameterbereiche mit entartetem und invertiertem Spektrum durchlaufen werden. Das entartete Linearisierungsspektrum ermöglicht eine im Wesentlichen unabhängige Bewegung der einzelnen Teilchen und damit die Existenz lokalisierter Anregungen, die sich ohne signifikante räumliche Ausbreitung in der Zeit entwickeln. Neben der Dynamik kleiner Schwingungen ist auch die Entwicklung nichtlinearer Anregungen stark beeinflusst durch die Geometrie. Speziell erfährt eine anfänglich breite Anregung im Laufe der Dynamik einen fokussierenden oder defokussierenden Effekt, je nach Wahl des Helixradius. Dieses geometrisch kontrollierte nichtlineare Verhalten kann im Rahmen eines effektiven diskreten nichtlinearen Schrödingermodells verstanden werden, was darüber hinaus das Auffinden intrinsisch lokalisierten Anregungen des Systems ermöglicht.

Abstract

In this thesis the equilibrium and dynamical properties of identical charged particles confined in different helical manifolds are studied. Starting from the trivial case of a confinement on a line-segment we investigate the statistical properties of the many-body system of charges. We detect a crossover from a crystalline to a cluster phase with increasing temperature and a non-extensive behaviour of the thermodynamic functions, owing to the long-range character of the interactions. The two-body interactions change fundamentally when the trapping geometry becomes curved, acquiring an oscillatory form in the case of trapping on a homogeneous helix, allowing for the creation of bound pairs. For an inhomogeneous helical trap, the center-of-mass and the relative motion of two charges couple, and induce an energy transfer between the collective and the relative motion, making possible a dissociation of initially bound states through scattering. In the many-body case, the constraint of equally charged particles on a closed helix leads to the emergence of different equilibrium states. At commensurate fillings, the ground state undergoes a pitchfork bifurcation from a symmetric polygonic to a zigzag-like configuration with increasing radius of the helix. Remarkably, below the bifurcation point, the vibrational frequency spectrum deforms in an unconventional manner with the increment of the helix radius, passing through subsequent stages of degeneracy and inversion. The degenerate spectrum allows for an essentially independent motion of the individual particles resulting in localized excitations which can propagate in time without significant spreading. Apart from the dynamics of small amplitude excitations, also the dynamics of nonlinear excitations is crucially affected by the geometry. In particular, a broad excitation is found to undergo a focusing or defocusing during the time evolution, depending on the values of the helix radius. This geometrically controlled nonlinear behaviour can be understood within an effective discrete nonlinear Schrödinger model, which also allows for identifying some breather-like excitations in the system.

Contents

Preface

Thesis Outline

The present cumulative dissertation is based on the publications [O1–O4]. In these works we have explored structural and dynamical properties of one dimensional systems consisting of singly charged particles, confined in different helical manifolds (including also degenerate cases of helical geometry, as the straight line). Characteristic elements of our systems are the long-range Coulomb interactions among the particles and the non-trivial geometry induced by the confinement. On the one hand, these link our studies to the physics of cold ions and other Coulomb systems. On the other hand they establish a connection to other systems of a complex geometry such as curved nanostructures and biological molecules. We provide an introduction in these fields in Chapter 1, including also an outline and a brief discussion of our scientific contributions. A full presentation of these contributions, as a collection of the corresponding research papers, can be found in Chapter 2. Finally Chapter 3 contains our overall conclusions and a short outlook for further investigations.

We note that when referring to our scientific contributions throughout the current thesis we will always use the reference index of our corresponding publication, instead of addressing its position within Chapter 2.

List of publication on which this dissertation is based:

[O1] A. V. Zampetaki, F. K. Diakonos, and P. Schmelcher. Finite-temperature crossover from a crystalline to a cluster phase for a confined finite chain of ions. *Phys. Rev. E*, 87(4):042116, 2013.

[O2] A. V. Zampetaki, J. Stockhofe, S. Krönke, and P. Schmelcher. Classical scattering of charged particles confined on an inhomogeneous helix. *Phys. Rev. E*, 88(4):043202, 2013.

[O3] A. V. Zampetaki, J. Stockhofe, and P. Schmelcher. Degeneracy and inversion of band structure for Wigner crystals on a closed helix. *Phys. Rev. A*, 91(2):023409, 2015.

[O4] A. V. Zampetaki, J. Stockhofe, and P. Schmelcher. Dynamics of nonlinear excitations of helically confined charges. *Phys. Rev. E*, 92(4):042905, 2015.

Background and personal contributions to the publications [O1–O4]

The first work [O1] originated as an attempt to gain insight into the statistical behaviour of one-dimensional (1D) Coulomb systems in the most simple case of a confining box trap. I have performed all the numerical simulations (classical Monte-Carlo) and the analysis and written the manuscript. I have also worked out myself the analytical proof of the appendix.

The idea for the second work [O2] was to examine a two-body helical system which does not provide a separation of the center-of-mass from the relative coordinate. Preliminary results in this direction were obtained within a previous bachelor project of Michel Jüngling. I have checked, analyzed and extended those preliminary results through numerical simulations. I have carried out all the numerical calculations and analysis as well as written the corresponding manuscript. The analytical proof of the appendix, was mainly worked out by Jan Stockhofe and Sven Krönke.

Towards the extension of the two-body problem to the many-body case, I came up with the idea of studying a system of charged particles confined in a closed helix. I have conceptualized, therefore, the projects [O3, O4], performed all the numerical and analytical calculations and written both manuscripts.

Chapter 1

Introduction

Our perception of the physical world, ranging from the universe to objects of our everyday life to systems of the microcosm, attributes to space the properties of a Euclidean geometry in three dimensions. The deeper understanding of many physical phenomena, however, crucially depends on their natural description within fewer dimensions embedded in three-dimensional (3D) space. Indeed, the behaviour of generic particles or waves will inevitably feature imprints of their motional constraint onto 1D lines or 2D surfaces. Intriguing differences to the unconstrained motion arise, in particular, when such spatial manifolds are curved or twisted, owing to geometry-induced modifications already in the external potential for noninteracting systems. The impact of the confinement on *interacting* particles is even more dramatic, since new effective interactions may emerge as a result of the reduced dimensionality equipped with a non-trivial geometry. The aim of the present work is to explore the triptych of dimensionality, geometry, and interactions, in systems where the three are intimately related, and to demonstrate the consequences of their interplay at a fundamental level. In the following, we start by addressing theoretical and experimental aspects of each constituent alone as well as combined in order of increasing complexity.

While low-dimensional systems may easily be conceived as simply occupying certain submanifolds of 3D space, their experimental realization at the microscopic level is in general a challenging task. Confinement of particle motion at the nanoscale has only become possible over recent decades, with the ever increasing precision owing to radical technological advances in material science as well as, e g., novel techniques in the trapping and cooling of atoms. The constructed low-dimensional systems not only allow for a more lucid view on 3D physics, but also exhibit unprecedented physical effects absent in their 3D counterparts. A prominent example in this direction is the celebrated quantum Hall effect showing the quantization of resistance under a magnetic field for a 2D electron gas confined at a semiconductor heterojunction [1]. Regarding electrons in 2D materials, another system with spectacular properties is graphene [2, 3]. Its planar hexagonal arrangement of carbon atoms leads to an analogue of quantum electrodynamics within condensed matter, allowing for the study of effects that are energetically inaccessible in elementary particle physics. Furthermore, graphene can be rolled up in various ways, forming quasi-1D structures known as carbon nanotubes [4, 5]. These nanostructures apart from inheriting peculiar bandstructure features from graphene [4], they display also an extraordinary thermal conductivity as well as advantageous mechanical and electrical properties [5, 6]. Systems of even lower dimensionality, such as 0D quantum dots, have also been an object of intense research the last decades as prototype elements to reveal effects of quantum coherence and due to their tunable optical and transport properties [7].

The properties of effectively low-dimensional systems are altered significantly by the presence of a non-trivial geometry in the confinement, as in the case of electrons moving along curved layers or quantum wires [8]. In contrast to its classical analogue, a single quantum particle constrained to a curved 2D or 1D space always acquires some knowledge how the confining manifold is embedded in the surrounding 3D space. This fact is expressed by the appearance of a curvature-induced potential [8–10]. Such a *geometric potential* is found to induce localized bound states for particles confined on curved waveguides [8, 11–16] which can turn into resonances with an application of an external electric or magnetic field [8]. Furthermore, in the special case of a helical waveguide, the geometric potential can induce an effective transverse electric field leading to charge separation [17, 18].

Most of the aforementioned systems and effects can be described adequately within an effective single-particle picture and in terms of the corresponding energy spectra. Depending on the type of confinement, interactions between the trapped particles are often responsible for a qualitatively different system behaviour. Already their inclusion at an elementary level in the the theoretical description may explain correlated particle effects, an example being Coulomb blockade of electronic transport through quantum dots as captured by the constant interaction model [7, 19]. Many-body interactions are also considered as the origin of the fractional quantum Hall effect [20] which complements its integer version when a 2D electron gas is in a relatively condensed state. Further effects relying on interacting particles confined in low dimensions are encountered in the field of cold ion [21, 22] and cold atom [23] physics. These include, for example, crystallization and structural phase transitions (linear-to-zigzag) [22, 24] for cold ions as well as exotic phases (Tonks-Girardeau gas) [25, 26] and quantum phase transitions (Mott-to-superfluid) [27] for cold atoms. Apart from an almost arbitrary shaping of trapping potentials [28–31], most of these nearly defect-free systems possess the additional advantage of permitting a large tunability of the interaction strength by external fields [23, 32, 33].

From the above considerations a compelling question arises: What would be the combined effect of a non-trivial geometry and interactions in a low dimensional system? Studies in this direction, including strongly interacting particles confined on toroidal, circular, or helical traps, have demonstrated the occurrence of geometry- and interaction-induced effects such as phase slips between persistent current states [34] or peculiar energy spectra described within molecular models [35]. In the particular case of long-range interacting particles constrained on a helical wire, formations of electron pairs [36] and zero-temperature second order liquid-gas transitions [37] have been predicted. Long-range interactions play a key role for the dynamics of particles in curved geometries: Since the interparticle Euclidean distances enter the 3D interaction potentials, the particles indirectly become ‘aware’ of the geometry of the curved manifold, without the necessity of a spatially extended wave function. In other words, classical systems of point charges are capable of exhibiting characteristic geometry-induced effects due to long-range interaction. A remarkable case is the formation of an oscillatory effective two-body potential for equally charged or polar particles confined on a uniform helical manifold [36, 38, 39]; this allows for the creation of bound states consisting of same (repulsively interacting) charges [36, 38] or characteristic dipolar chains [39], respectively. Already for a few particles the potential landscape of such systems is very complex, supporting multiple stable configurations with increasingly distorted symmetries [38]. These findings have led us to the quest for answering the multiple generated questions regarding the low energy structure, the excitation spectra and the statistical behaviour of many-body systems consisting of helically confined interacting particles.

Objectives of this thesis

In view of the complexity and richness of helical long-range interacting systems, the present thesis theoretically explores the equilibrium properties and classical dynamics of identical charged particles confined in different helical manifolds. Our major findings include

- the finite-temperature crossover from a crystalline to a cluster phase for a finite number of identical charges confined in a straight 1D box (a limiting case of a helical segment), [O1]
- the dissociation of initially bound states in a scattering process due to the energy transfer between the collective and relative motion for two identical charges confined on an inhomogeneous helix, [O2]
- unconventional deformations of the vibrational band structure for crystals formed by repulsive charged particles (Wigner crystals) confined on a closed helix when tuning the helix radius [O3], and
- the self-focusing of an initially broad excitation for Wigner crystals on a toroidal helix of a specific geometry, accompanied by the existence of breather-like excitations [O4].

While the first case explores structure formation in an uncurved many-body Coulomb system, in the latter three cases the geometry plays a fundamental role and provides the means for controlling the response of the strongly interacting system.

We set out in this section with a brief overview of trapped ion physics in Sec. 1.1, focusing on the crystalline structures and structural transitions observed in such systems, as being particularly relevant to our work. In the same context, we continue in Sec. 1.2. with a discussion of our first contribution, concerning the statistical behaviour of an ion chain in a 1D box. Having then obtained the necessary information about the physics of Coulomb systems, we proceed to a justification of the choice of the helix as a confining manifold for the rest of our studies. To this end, Sec. 1.3 presents characteristic examples of the emergence of helical spatial structure in nature as well as various interesting effects arising from an enforced helical confinement. We focus on the physical properties of long-range—especially Coulomb—interacting particles confined on a helical manifold in Sec. 1.4. Finally, Sec 1.5 outlines the major part of our scientific contributions concerning helically confined charges, giving in each subsection the motivation for the respective work and a summary of our results.

1.1 Trapped ions and other Coulomb systems

The earliest trapping of ions was achieved by Kingdon already in 1923 [40] during his study of electrical discharges between a thin filament cathode and a cylindrical anode and led to a great advance in precision spectroscopy. The developments of the Penning [41] and Paul [42, 43] traps followed, the first employing again the electrical discharges between coaxial cylinders but under the presence of an additional axial magnetic field and the second by exploiting the electric field created by radio-frequency (rf) potentials applied to four hyperbolic electrodes in pairs. Their discovery allowed for high precision mass spectroscopy [44–46] as well as for an estimation of the electron g-factor [47]. The real breakthrough in the ion trapping came, however, in 1980s with the advent of laser cooling [48–52]. The kinetic energy of ions was so reduced, permitting essentially a spectroscopy on stationary ions and improving dramatically their confinement both in Penning and in Paul traps [53–57]. Thus, as expected, it paved the way for the development of what is known as cold ion physics.

Cold ions constitute a prototypical example of strongly correlated systems with long-range interactions. Being essentially a collection of identical charged particles, they share common properties and terminology with a cold electron gas. Such a gas, due to the strong long-range interactions, was predicted to crystallize and form a lattice at sufficiently small densities, known as Wigner crystal [58]. If the transition to the crystalline structure occurs at $T = 0$, it is of quantum nature and arises as zero-point fluctuations decrease, following the decrease in the density. On the other hand, it is possible to have a classical transition to the crystal, caused by the reduction of thermal fluctuations. We will refer to this second, classical transition to a crystalline stage from now on, unless stated otherwise. In either case, at the stage of Wigner crystal the mean potential (Coulomb) energy, being orders of magnitude larger than the mean kinetic energy, dominates the behaviour of the system, allowing for a classical estimation of the crystalline structure [1]. Nevertheless, quantum effects are important for an accurate description of certain classes of Coulomb (Wigner) crystals. In particular, the quantumness of a Coulomb crystal can be estimated by the ratio $\chi = \Lambda/a$, where $\Lambda = h/\sqrt{2\pi m k_B T}$ denotes the deBroglie wavelength and a stands for the average interparticle distance [59]. If $\chi \geq 1$, as is usually the case for electrons confined in nanostructures, the corresponding crystal can be regarded as quantum, whereas in the

---

[1] This can be obtained in the standard manner, by minimizing the full interaction potential.

opposite case ($\chi < 1$), holding for trapped ions, the Wigner crystal can be treated as classical. This distinction between quantum electrons and classical ions will be assumed throughout this section.

Apart from quantumness, another property characterizing Coulomb crystals is their dimensionality. Systems of a reduced dimension can be obtained by "freezing out" one or more dimensions. This can be experimentally achieved by the combined effect of very low temperature and a strong confining potential. For suitable parameters, the excitation energy of the particles in one ore more directions becomes much higher than their average thermal energy, resulting in the corresponding dimensions being effectively frozen out. The ensuing Coulomb crystals of different dimensions self-organize in different structures. Usually, such a crystalline structure is in 3D a bcc (body-centered-cubic) in 2D a hexagonal and in 1D an equispaced lattice. Whereas these structures are considered as optimal for infinite Coulomb systems, the inclusion of external trapping potentials leads to changes in each case, mostly by introducing some degree of inhomogeneity. A more detailed presentation of the most common structures for Wigner crystals in different confining potentials and dimensions is provided below.

1.1.1 Wigner crystals

The most prominent example of an ideal infinite 3D Coulomb system, is that of a one component plasma (OCP). This is essentially a system consisting of identical point charges, free to move in a uniform neutralizing background. It is characterized by the ratio Γ of the average Coulomb energy to the average kinetic energy, known as the coupling constant. If $\Gamma > 1$ the plasma is strongly coupled, however, Γ has to be of the order of 100, in order to observe the formation of a bcc Wigner crystal through a liquid-to-solid transition [60–64]. Under the influence of an isotropic harmonic trapping potential, which is a very good approximation of the confining potential created by a quadrupole (Paul) trap, small plasma clouds are found to form concentric spherical shells with constant inter-shell distances and a hexagonal surface structure [65, 66]. As the clusters get larger the two forms of ordering (shell structure and bcc) start to compete, and beyond some critical value of the particle number, the bcc structure dominates in the interior of the crystal, resembling the case of the OCP [63, 67].

Surprisingly enough, it was not in 3D but in 2D where the first experimental observation of Wigner crystallization was achieved, during the study of electrons on the surface of liquid-He [68, 69]. For $\Gamma = 137 \pm 15$ the transition to a hexagonal (or triangular) crystalline structure occurred, as expected for a 2D OCP [70]. An inclusion of an isotropic harmonic confinement, was found to change this picture similarly to the 3D case: Small Coulomb clusters would crystallize in circular shells [71], while larger ones in an inhomogeneous structure whose interior formed a hexagonal lattice [72].

Among others, 2D offer the possibility of considering confining manifolds with a finite curvature, such as a sphere or a torus. The interest on crystallization in such surfaces dates back to Thomson and his classical problem to find the ground state of N identical charges confined on a sphere [73]. A hexagonal lattice is precluded in such a case from topological considerations [74] and defects are expected to appear on top of the sixfold coordination lattice, adding up to at least 12 fivefold disinclinations. The ground state structures are thus very complex, including usually many defects (especially for large number of particles) and many metastable states arise with very small energy difference from the ground state [74–78]. The toroidal surface, although not prevented from topology to support a hexagonal crystalline structure, it leads as well to a formation of inhomogeneous crystals, due to the tendency of the particles to occupy its outer part, which provides a larger interparticle separation [74, 78, 79]. Both cases of curved confining manifolds support interesting dynamics in the process of melting, involving also annihilations of dislocations [74, 78].

The 1D case

Recently, particular interest was dedicated to the study of 1D Coulomb systems [80–93]. This can be primarily attributed to the exceptionally strong correlations of the 1D Coulomb chains, which contribute to the total energy of the system at the same order as the mean field energy, prohibiting their exclusion and making Coulomb chains a unique condensed matter system [81, 88].

The first prediction of Wigner crystallization for electrons in 1D was done by Schulz [80]. Using the bosonization technique, he showed that a 1D electron gas with long-range Coulomb interactions, possesses, for arbitrarily weak Coulomb repulsion, density-density correlations which signify the existence of a Wigner crystal structure. In particular, the correlations at the wave vector $4k_F$, with k_F the Fermi momentum, were found to decay extremely slowly, matching the behaviour of correlations for an equidistant classical Wigner crystal. The slow decay prohibits the existence of a true long-range order which is expected to be destroyed in 1D systems due to quantum fluctuations [94]. A direct experimental observation of such a 1D Wigner crystal has only recently been achieved in the hole gas of semiconducting carbon nanotubes [86].

Concerning cold ions, the experimental advances in trapping techniques have early allowed for the creation of a 1D Coulomb chain [95, 96], which, in the above line of arguments, can be regarded as another form of a 1D (classical) Wigner crystal. Theoretical studies of 1D Coulomb chains under a harmonic confinement have shown that both correlations and long-range interactions are essential in extracting the density of the crystalline structure [81]. This structure is inhomogeneous with the density being higher in the center of the chain and lower towards the edges, following an approximately parabolic law. Both the length L and the energy E of the chain depend on the number of particles N in a non-extensive way (they do not increase linearly with N) as can be seen in the following expressions [81]

$$L^3(N) = \frac{3q^2N}{m\omega^2}\left(\gamma - \frac{13}{5} + \ln(6N)\right), \quad E(N) = \frac{3}{10}Nm\omega^2L^2(N), \tag{1.1}$$

where q is the charge of each ion, m its mass, ω the trapping frequency and γ the Euler constant. These rather unconventional results have motivated the theoretical study of the dynamical and thermodynamical properties of the 1D Coulomb chain in a harmonic potential [82–84]. It was shown analytically that the 1D crystal supports not-phonon-like eigenmodes and that the thermodynamic quantities deviate from extensivity, with the dependence of the specific heat on the number of ions as a representative example. Thus, the 1D trapped Coulomb chains behave fundamentally different from their 3D counterparts and constitute an exceptional system in the framework of statistical physics. These outcomes were the major motivation for our first work [O1] where we have also explored some statistical properties of 1D chains but under a confinement in a hard wall potential, instead of a harmonic. Our results also show an inhomogeneity of the ion chain, -but different from that for harmonic confinement-as well as, a non-extensivity of macroscopic quantities.

The case of Wigner crystallization in 2D curved manifolds discussed earlier, suggests that the exploration of their 1D analogue could reveal interesting physical effects. However, studies of 1D Wigner crystals in different confining geometries are rather rare in literature. Most attention has been given to the study of 1D homogeneous Coulomb chains in periodic lattices [85,90,93], which bear similarities with the Frenkel-Kontorova model [97], exhibiting a sliding-pinning transition that leads to the formation of incommensurate crystals. These systems are considered as good candidates for studying dry friction and energy transport. Their experimental realization is often linked to the possibility of optical ion trapping which has been recently achieved for a single ion [98]. A real confinement on a 1D curved manifold was considered in [91], where Wigner crystals trapped in 1D snaked nanochannels were explored and found to exhibit a very similar behaviour to the ions in a periodic lattice [85]. The major part of our scientific contributions in this thesis aims to expand our knowledge of Coulomb systems in 1D curved geometries, through the study of Wigner crystals formed on a toroidal helix [O3, O4] revealing, indeed, interesting equilibrium and dynamical properties.

Before closing this paragraph, let us mention a last example of Coulomb crystals, this time consisting of cold ions confined in linear octupole traps. In such a case, except for the standard harmonic term, there is also an rf contribution to the potential $V_{rf} \sim r^6$, with r the distance from the trap axis [99] [2]. This pushes the ions away from the center of the trap, leading to fundamentally different structures from those formed in a quadrupole trap. In particular, instead of ion chains along the trap axis, hollow cylindrical structures are created, based on one or multiple rings, or exhibiting emergent chirality [101–104]. Crucial for the character of these crystalline forms is the existence of specific "magic numbers" which determine the number of ions needed for a perfect pattern to be created for given trap parameters [103, 104]. Away from the magic numbers the creation of defects is inevitable.

1.1.2 Structural phase transitions

We have seen that a plethora of different crystalline structures emerge for Coulomb systems, depending on the dimensionality and the external trapping potential. Melting is the principal mechanism leading to the dissolution of such crystals, through the incre-

---

[2] For a general multipole trap with $2k$ electrodes the respective rf contribution is $V_{rf} \sim r^{2k-2}$ [100].

ment of temperature. Apart from that, in systems with tunable parameters there are also other ways for inducing deformations of a given structure, or transitions between different crystalline patterns, termed as structural phase transitions [105]. For cold ion systems (at zero temperature) such tunable parameters are usually the particles' density or a characteristic parameter of the trapping potential.

In the first case, for ions confined in 2D and subjected to an external harmonic potential, an increment of the particle density causes transitions of the linear ion chain to structures with an increased number of chains [106]. In particular, in an attempt to maximize the interparticle distances, the single ion chain bifurcates to a zigzag structure (two chains), beyond some critical density, followed by successive transitions to three, four, five and six chains, tending thus to cover the full plane. These lead to a rich phase diagram consisting of both continuous and discontinuous structural phase transitions. A similar case, exhibiting even more structural complexity, is provided for cold ions confined in a cylindrically symmetric harmonic potential [107]. The linear chain along the trapping axis, formed for low densities, destabilizes above a critical density due to the strong repulsion, giving its place to a zigzag pattern. Further increment in density causes the formation of helical structures with increasing number of ions per turn, followed by a tetrahedral structure and ending with the formation of shell structures covering the full 3D space as those described in the previous subsection. The first experimental confirmation of the above theoretical predictions was direct [95] and performed with the use of $^{24}\mathrm{Mg}^{+}$ ions in a quadrupole storage ring.

Ionic structures of different geometries have also been experimentally observed when tuning the trapping frequency and in particular, the radial to axial aspect ratio $\alpha = \frac{\omega_r}{\omega_z}$ of a quadrupole (Paul) trap [108–110]. Among others, a structural transition from a spheroidal string structure [108] to an array of disks configuration, as well as, a formation of crystals of different shapes, ranging from a cigar-shape to a pancake-shape have been demonstrated [109, 110]. Linear ion chains in a quadrupole trap have also been found to destabilize during a decrease of the transverse-to-longitudinal aspect ratio $\alpha = \frac{\nu_t}{\nu}$, leading to the succeeding formation of zigzag [24, 111–113] and helical structures, in analogy to the results discussed above. The linear-to-zigzag structural transition (Fig. 1.1 (a)) can be described theoretically within a standard Ginzburg-Landau model [24, 112]. We will outline below some of the basic features of this transition.

Linear-to-zigzag transition

The two major reasons for the occurrence of a linear-to-zigzag transition as already discussed are the increment of the particle density or the decrease of the trap aspect ratio α. We will focus here on the second case, described in [24], but point out that the first one exhibits the same characteristics [106,112] as well. Under the approximation of an equidistant chain, valid in the central region of Paul traps or for ions on a ring, the classical equilibrium positions are given by $x_j^{(0)} = ja$, $y_j^{(0)} = z_j^{(0)} = 0$, where a stands for the interparticle spacing. A harmonic approximation of the potential around these positions yields the longitudinal $\omega_{\parallel}(k)$ and transverse $\omega_{\perp}(k)$ dispersion relations [24]

$$\begin{aligned}\omega_{\parallel}(k)^2 &= 4\left(\frac{2q^2}{ma^3}\right)\sum_{j=1}^{N}\frac{1}{j^3}\sin^2\frac{jka}{2}\\ \omega_{\perp}(k)^2 &= \nu_t^2 - 2\left(\frac{2q^2}{ma^3}\right)\sum_{j=1}^{N}\frac{1}{j^3}\sin^2\frac{jka}{2},\end{aligned} \tag{1.2}$$

where q is the charge of each ion, m its mass and $k = 2\pi n/Na$, $(n = 0, \pm 1, \pm 2, \ldots)$ denotes the wave-vector. Evidently, the transverse branch can become imaginary ($\omega_{\perp}(k)^2 < 0$) below a critical transverse trapping frequency ν_t^c, rendering the linear chain unstable.

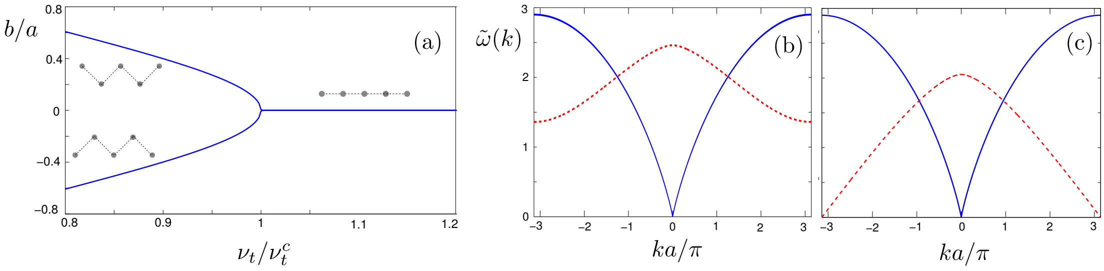

Figure 1.1: (a) Transverse equilibrium displacement b in units of interparticle distance a as a function of the transverse trapping frequency ν_t, measured in units of ν_t^c (b),(c) Dispersion relations $\tilde{\omega}(k)$ ($\tilde{\omega}$ is the dimensionless frequency given by $\tilde{\omega} = \omega\sqrt{ma^3/Q^2}$) for different values of the transverse frequency: (b) $\nu_t = 1.2\nu_t^c$ and (c) $\nu_t = \nu_t^c$. In the figures are depicted both the longitudinal branches $\tilde{\omega}_{\parallel}(k)$ (solid blue lines) and the transverse branches $\tilde{\omega}_{\perp}(k)$ (dashed red lines). The wave-vector k is measured in units of π/a.

The lowest frequency $\omega_{\perp}$ is found at $k = \frac{\pi}{a}$ (Figs. 1.1 (b),(c)), determining the value of ν_t^c (Eq. 1.2) and the soft mode of the transition (corresponding to the eigenmode of $k = \frac{\pi}{a}$ given by the expression $y_j = (-1)^j b/2$). Such a mode induces alternate transverse displacements of the particles, leading to the final zigzag structure, identified as the ground state for $\nu < \nu_t^c$ (Fig. 1.1 (a)). A rigorous analysis according to the Landau theory [24] shows that the effective potential in the critical region has a biquartic form with a single minimum for $\nu > \nu_t^c$ corresponding to the equidistant chain, whereas for $\nu < \nu_t^c$ it attains a Mexican hat form with degenerate minima corresponding to degenerate zigzag configurations. This signifies a symmetry breaking mechanism (or pitchfork bifurcation), characteristic of a second order phase transition in the thermodynamic limit $N \to \infty$.

Summarizing, in an intuitive picture, as the transverse trapping frequency decreases, the dimensionality of the available space increases from 1D to quasi-1D, making it advantageous for the particles to form a zigzag structure. A measure of the energy cost to occupy the transverse dimension is given by the minimum transverse eigenfrequency $\omega_{\perp}(\pi/a)$, which tends gradually to zero. At the critical point $\omega_{\perp}(\pi/a) = 0$ (Fig. 1.1 (c)) , meaning that the corresponding transverse motion (zigzag) is given for free and the system enters the zigzag phase. Note that during this procedure the longitudinal frequency spectrum $\omega_{\|}(k)$ remains unchanged (Figs. 1.1 (b),(c)) .

As a last remark, let us briefly comment on the quantum version of the zigzag transition. It is found that such a transition is possible in the quantum regime and maps to the quantum Ising model in a transverse field [114, 115]. The major effect of the quantum fluctuations is then to shift the critical transverse frequency to lower values, extending thus the regime of the disordered (linear) phase [114]. In the zigzag regime the number of the relevant neighbouring contributions is increased with respect to the linear one, from two to four, resulting in a rich phase diagram [87, 116].

The last paragraph of this section is devoted to one of its most important parts, namely the physical and technological applications of the cold ion systems. We aim at this point only at a brief overview of their major applications in science, with our list being far from complete. More information on ion traps and their applications can be found in [21, 22, 29].

1.1.3 Applications of trapped ions

Having discussed about some physical aspects of the cold ion systems, it is the time to provide an answer to the crucial question of their applications. As it should have already become clear, cold ions constitute a prototype of a strongly correlated condensed matter system which is almost defect free and very dilute in comparison to the standard systems. Even more, its dimensionality can be easily tuned, leading to interesting structural transitions and to a unique form of matter (1D Wigner crystals) with particularly enhanced correlations.

The internal structure of the ions permits them to be in different internal states (in analogy to spins) controlled by laser fields, allowing thus for a mapping of cold ionic systems to different quantum Ising models [117]. This gives to ion chains the ability to act as quantum simulators [117–122] simulating, among others [123, 124], spin-spin interactions. Experiments with a few number of ions (spins) have been carried out [121, 125–127] which have demonstrated clear signs of a theoretically predicted quantum phase transition. However, a real many-body experiment has not yet been realized [120, 121] in this context. Along with the realizations of quantum simulators, come the proposals for implementations of quantum information processors [120, 128–139]. These rely again on the mapping of each ion to a qubit and take advantage of the strong coupling, the controlled manipulation, and the detection efficiency provided for cold ion chains. Entanglement can be achieved through the ions' coupling to external fields and thus multiple quantum gates can be constructed. Once more, the great challenge is to scale such systems up to a large number of ions [134, 136–138].

On the other hand, a small number of ions seems to be advantageous for applications in spectroscopy and metrology, which are fields historically connected with the development of ion trapping [140, 141]. The combination of the ion trapping technology with the laser cooling technique -giving the ability to study even a single trapped ion- led to very high precision frequency standards [53–57, 142–146] and even permitted nonlinear spectroscopy [147], a synchronization of ionic motion [148] and spectroscopy of interacting quasi-particles [149]. The control and the accuracy in measurements performed in cold ionic systems have also led to advances in metrology [136, 150–154] with the most prominent one being the accurate measurement of the g-factor of an electron via the so-called continuous Stern-Gerlach effect [44, 152, 154, 155].

Last but not least, trapped ions, due to the long-range character of their interactions, present very interesting nonlinear dynamics [84, 156–163] including a transition to chaos [156, 157], a phase locked motion [158], a pattern formation [160] and many bifurcations accompanied with kink formations [161, 162]. The formation of kinks in trapped ionic systems permits the study of structural defects formed during a second order phase transition [164, 165] and provide means to test the predictions of the Kibble-Zurek mechanism, initially developed in the context of cosmology [166–168]. Other applications of cold ions in testing cosmological effects such as particle formation can also been found in the literature [169–171].

This section has provided us with an overview of the major aspects and applications of cold ionic systems, to which all of our systems, consisting of identical charged particles, naturally belong. Having gathered all the necessary information, we now proceed to an outline of our first scientific contribution, concerning the statistical properties of an ion chain confined in a 1D box.

1.2 Outline of scientific contribution I: *Ion chain in a 1D box*

As we have pointed out several times in the previous section, the 1D Coulomb systems consisting of singly charged particles are exceptional, in the sense that they possess very strong correlations which cannot be safely neglected. We proceed on a simple qualitative demonstration of this fact, following the arguments of [81]. For a d-dimensional system of volume L^d with N identical charged particles of charge q, the mean Coulomb energy E_M scales roughly as $E_M \sim q^2N^2/L$, since we have N particles interacting with each other in pairs which are separated on average by a distance L. Now the energy associated with the discreteness of the system, identified as the correlation energy E_C, is limited on the level of the nearest-neighbour pairs. Since the average interparticle spacing is of the order of $a \sim (L^d/N)^{1/d}$ and there are only N such pairs we arrive at the conclusion that $E_C \sim Nq^2/a = q^2N^{1+1/d}/L$, leading to $E_C \sim N^{1/d-1}E_M$. For $d > 1$, as $N \to \infty$, the correlation energy E_C becomes negligible compared to E_M. If $d = 1$, however, it turns that $E_C \sim E_M$ meaning that the two contributions are of the same order.

This fact has led to many studies of 1D Coulomb chains, the majority of them [81–84] being exposed to an external harmonic potential, acting as a trap (quadrupole trapping), and found to exhibit an inhomogeneity in the structure and a non-extensivity in the thermodynamic functions. We have posed in our work similar questions about the structure and the thermodynamics, regarding again a 1D Coulomb system, but under the presence of a 1D box potential. As this potential is simpler than the harmonic one, possessing also a clear length scale (the size of the box L), our study provides clarifying results, complementary to those already existing in literature.

Specifically, in our study, we have explored with the use of Monte-Carlo techniques the structural and statistical behaviour of the 1D ion chain at different temperatures [O1]. For low temperatures the ions form inhomogeneous chains with an almost constant density at the center and an accumulation of the particles at the edges of the box. This is directly opposite to the inhomogeneity of the chains for harmonic confinement [81] and can be attributed to the fixed size of the box in contrast to that of a harmonic trap. We prove that this is the only possible minimum configuration (apart from particle permutations), opposite to the case of 2D and 3D which support multiple equilibrium states. As the temperature increases the particles start to form randomly clusters of different sizes, keeping however a fixed average interparticle distance.

The thermodynamic behaviour of the system was found to be best described by the characteristic distributions and correlations of the interparticle distances, whereas quantities that depend on the absolute positions of the particles were shown to provide poor estimates, as they are almost unaffected by the temperature. In contrast, the distribution of the interparticle distances was found to undergo a great change when increasing the temperature. While for low temperatures it consists of a number of discrete peaks, it smooths out as the temperature increases, passing through a symmetric shape and acquiring finally an exponential form. Thus, starting from a crystalline form, more and more configurations become gradually accessible, due to the increased supply of thermal energy, leading to the formation of clusters. At ultra-high temperatures almost any configuration can be accessed and the particles behave as if they were non-interacting. Therefore, by observing the distribution of the spacings, we identify a crossover from a crystalline to a cluster phase in our system, reminiscent of a solid-to-liquid transition. We are also able to estimate its critical temperature by analyzing the behaviour of the distributions' skewness.

The dependence of the mean energy and the heat capacity on the temperature supports the picture of the observed crossover, with the latter exhibiting an increment at the corresponding region. Moreover ,the mean energy of the system at low temperatures is found to scale as

$$\langle E \rangle \propto \frac{N^2 \log(N)}{L}, \tag{1.3}$$

which is non-extensive due to the additional $N\log(N)/L$ factor. Note that to leading order this is the same kind of non-extensivity found for the harmonic confinement (Eq. 1.1), if one takes into account also the N-dependent length. Through this expression for the energy we are able to define, by using the Tsallis concept of entropy for non-extensive systems [172], a finite thermodynamic limit for our system of particles confined in a box, allowing us to make estimations about other 1D Coulomb systems as well. As a last remark, let us mention that the phenomenology attached to the crossover observed in this work is quite general, and could be applied also to other 1D interacting systems which at zero temperature support a single stable state.

In the rest of our scientific contributions (Sec. 1.5) we continue with the exploration of 1D classical Coulomb systems, but we assume a trapping manifold with a non-trivial geometry, namely a helix. Before we move on, we find it therefore essential to discuss briefly the exceptional position of the helical geometry in nature, justifying our choice of it as a trapping manifold.

1.3 The importance of the helical geometry

From a mathematical viewpoint, the helix constitutes a unique curve in 3D space possessing both a constant curvature and torsion. Being the only curve generated by a screw operation (combined translation and rotation), the characteristic isometry of a 3D Euclidean space, it has a special position among the curves in 3D, analogous to that of a circle (generated by rotation) in the 2D space. It is also periodic and chiral -meaning that there exist right and left handed helices which can only map to each other through reflection- and it provides the shortest path between two points on a cylindrical surface.

Apart from its mathematical interest, the helical geometry appears very commonly in nature as an emergent structure in different systems. The most celebrated examples come from biology and include the famous double-helix of the DNA molecule and the α-helix appearing in the secondary structure of several proteins and other macromolecules. The reason for the occurrence of such structures is multifold. For the DNA it is primarily a matter of stability and balance among the forces exerted between different constituents of the nucleotides such as the hydrophilic charged phosphates and the hydrophobic bases, embedded in the water environment of a cell [173]. For proteins, the reason for attaining a helical form can be even more complicated, related again to the stability and bonding of their elements, but also associated with properties of optimal packing and folding [174–180].

Helical patterns emerge naturally also in inorganic matter, such as at silicon and carbon nanotubes [181, 182], at self assembled configurations of charged particles on nanofibers [183–185], at magnetically trapped non-neutral plasma [186,187], as well as, at self-organizations of complex plasma [188]. In the latter case, the helical conformations can display features which bear similarities with those usually attributed to living matter such as memory and self-duplication. Another example of helical arrangement is provided by trapped ions which can form helical Wigner crystals through structural phase transitions [107, 111, 113].

The catalog of helical structures in organic and inorganic matter is, as it can be inferred from the few examples above, almost endless. This fact raises, apart from questions about their origin, also questions about their functionality. To this extent, the behaviour of particles or fields under the existence of a pre-established helical structure, acting as a constraint, is frequently studied in the literature as well.

One of the earliest applications of a helically confined motion was the Drude model for optical activity, consisting of a single electron confined on a helix and used in order to explain the optical activity of helical molecules [189–192]. Helical molecules, simulated by an equidistant ionic crystal confined on a helix, have also been found to induce an unconventional spin-orbit (SO) coupling on an electron passing through them, allowing thus for an efficient spin selective transport [193–195].

The advances in micro-/nano-fabrication, allowing for the creation of semiconductor nanohelices and helical arrays [196–200] have generated a further possibility for a helical confinement which has triggered several studies [13, 17, 18, 201–207]. First of all, the modeling of chiral carbon nanotubes as an equidistant chain of carbon atoms, situated along a helix, has permitted some preliminary estimations of the electronic band structures of fullerene tubules [201] as well as prediction of nonlinear and chiral electron transport effects [202]. Furthermore, quantum particles bound on helical tube surfaces were shown to feel an effective periodic potential, inducing energy band structures of geometrical origin [17, 204], whereas under a confinement to a helicoidal ribbon they were found to form localized states along its rim [18]. If the particle under consideration is charged it can exhibit superlattice properties under a helical confinement and the presence of a transverse electric field [203, 205, 206]. Even more intriguing, is the effect of circularly polarized light on helical wires. It can induce a steady current [13], as well as a dissipationless electron transport without Joule heating [207], relying on the broken time reversal symmetry of the system. This broken symmetry permits a medium constructed by many helical wires to exhibit gyrotropic properties [13] and when the helices are arranged in a honeycomb lattice it can even lead to the formation of what is known as a Floquet topological insulator [208].

Last but not least, there have been recent proposals relating to experimental realizations of helical traps for ultra-cold atoms [209, 210]. These employ either the interference pattern created by two counter-propagating Laguerre-Gaussian beams [209] or the evanescent field surrounding an optical nanofiber [210, 211]. In the latter case, an efficient trapping on a 1D helical manifold can be achieved for realistic experimental parameters by sending three circularly polarized light fields [3] through the nanofiber. This technique offers the possibility to create a homogeneous helical potential along the entire length of the nanofiber, as well as, to impose local modifications on the radius or the pitch of the helix.

In view of the exceptional features and the common appearance of the helical geometry in organic and inorganic matter, we deal in the major part of our scientific contributions [O2–O4] with the properties of identical charged particles under a helical confinement. These systems differ fundamentally from most cases already discussed, since they involve long-range interacting classical particles, combining thus the strong correlations present in the low dimensional Coulomb systems (Sec. 1.1) with a non-trivial geometry of great interest. The basic background of our work, as well as related studies dealing with strongly interacting particles constrained in helical manifolds are the subject of the following section.

---

[3] The two of them are counter-propagating and far red-detuned concerning the atomic transition whereas the last one is far blue-detuned

1.4 Interacting particles under helical confinement

The systems which we will discuss in the present and the following sections share common characteristics of consisting of identical particles interacting via long-range interactions, and being confined on helical manifolds. The general Lagrangian of such a system is given by

$$L(\{\mathbf{r}_i, \dot{\mathbf{r}}_i\}) = \frac{1}{2} m \sum_{i=1}^{N} \dot{\mathbf{r}}_i^2 - \frac{1}{2} \sum_{i,j=1, i \neq j}^{N} W\left(|\mathbf{r}_i - \mathbf{r}_j|\right),$$

where N is the number of particles, m denotes their mass and W refers to the two-body potential depending only on the Euclidean interparticle distance.

We consider the particles as being confined on a smooth curve $\mathbf{r} : \mathbb{R} \to \mathbb{R}^3$ parametrized by the parameter u. The position of each particle is given then by $\mathbf{r}_i = \mathbf{r}\left(u_i\right)$ and the Lagrangian attains the form

$$L(\{u_i, \dot{u}_i\}) = \frac{1}{2} \sum_{i=1}^{N} m \left|\partial_{u_i} \mathbf{r}(u_i)\right|^2 \dot{u}_i^2 - \frac{1}{2} \sum_{i,j=1, i \neq j}^{N} W\left(\left|\mathbf{r}\left(u_i\right) - \mathbf{r}\left(u_j\right)\right|\right).$$

This Lagrangian, which describes the confined motion of the interacting particles, has the peculiarity of possessing a kinetic term which depends, except for the particle velocities $\dot{u}_i$, also on their coordinates u_i. The additional term $m \left|\partial_{u_i} \mathbf{r}(u_i)\right|^2$ can be interpreted as an effective mass depending on the particle position. This can be removed if we choose the arc length parametrization, s, which is defined as

$$s : u \mapsto s(u) = \int_0^u \left|\partial_{u'} \mathbf{r}(u')\right| du', \tag{1.4}$$

with the Lagrangian reading finally

$$L(\{s_i, \dot{s}_i\}) = \frac{1}{2} m \sum_{i=1}^{N} \dot{s}_i^2 - \frac{1}{2} \sum_{i,j=1, i \neq j}^{N} W\left(\left|\mathbf{r}\left(s_i\right) - \mathbf{r}\left(s_j\right)\right|\right).$$

The cost of this parametrization is that we are left in general with a more complicated (even no explicit) form of the potential term, originating from the non-trivial dependence of s on u (Eq. 1.4).

The two-body potential, $W\left(\left|\mathbf{r}\left(s_i\right) - \mathbf{r}\left(s_j\right)\right|\right)$, is in principle a complicated function of s_i, s_j, not solely depending on their difference $s_i - s_j$. This means that the confinement on a curve generally induces a coupling of the relative coordinates, $\tilde{s}_i = s_{i+1} - s_i$, to the center-of-mass one $\tilde{S} = \frac{1}{N} \sum_{i=1}^{N} s_i$. The separation of the coordinates $\tilde{s}_i$ and S is achieved only in the restricted case of a confinement on a uniform helical curve or a degenerate case of it (circle or line), as we have proven in [O2]. This fact provides further motivation for studying the confined motion of interacting particles on a helical manifold.

The standard parametrization of a uniform right handed helix reads

$$\mathbf{r}(u) = \left(r\cos(u), r\sin(u), \frac{h}{2\pi}u \right) \tag{1.5}$$

where h denotes the pitch and r the radius of the helix (Fig. 1.2 (a)). In the limit $\frac{h}{r} \to 0$ the helix degenerates to a circle whereas in the opposite limit $\frac{h}{r} \to \infty$ it degenerates to a straight line.

Before proceeding in the description of our own scientific contributions, we discuss cases of interacting, helically confined systems that are found in literature, We first outline the results for systems of polar particles and finally, consider the case of charged particles which is directly relevant to our studies.

Prior to that, it is instructive to mention another interesting example of repulsively interacting particles which form helical arrangements. This is the so-called Levitov model [212] used in the field of phyllotaxis (study of mathematical regularities in plants) in order to explain the evolution of plants like cacti [213]. In this model, long-range repulsively interacting particles on the surface of a cylinder are assumed to form an equidistant helical chain. The optimal helical configuration changes as the linear particle density increases with the emergent instabilities following a number-theoretical law (Farey sequence [214]), leading asymptotically to an incommensurate helical structure related with the golden ratio ϕ. Such models can explain the structure of several cylindrical plants like cactus species and can be used to simulate their growth by simple mechanical models [213].

Polar particles

The existing studies of dipoles confined in helical traps [37,39,215] consider them to be aligned along the axis of the helix by means of an electric field. Under this assumption and for low enough pitch-to-radius ratio, the two-body potential $W(u_i, u_j)$ is repulsive for short distances and attractive for large ones, exhibiting minima -in terms of the relative angle $u = u_i - u_j$- at multiples of 2π. The classical many body system described by such a potential is found to self-organize into a number of chains, as a result of the interplay between the head-to-tail attraction and the side-by-side repulsion between the dipoles [39]. These chains destabilize and lead to clusterization as the number of particles increases. The picture of the chain formation is also supported by the few-body quantum analogue of the system [215].

A different aspect of the quantum system of helically confined dipoles is studied at [37]. The motivation of this paper is the similarity of the dipoles' effective two-body potential with the Lennard-Jones potential, used in thermodynamics in order to model thermal liquid-gas transitions. Based on this, the authors examine the phase diagram of a 1D gas of helically confined dipoles for different interaction strengths controlled by the magnitude of the external aligning electric field. They identify a zero-temperature second-order liquid-gas transition, taking place at a critical value of the electric field. This is a rather unconventional finding, considering especially that at absolute zero the systems are usually in a condensed phase, which has normally the lowest energy.

Charged particles

One of the most surprising and important features of identical charged particles constrained on a helix is their effective two-body interaction potential [36, 38]. Namely, under the helical constraint (Eq. 1.5) the Coulomb potential between two particles acquires the form

$$W(u_i, u_j) = \frac{g}{|\mathbf{r}(u_i) - \mathbf{r}(u_j)|} = \frac{g}{\sqrt{2r^2\left(1 - \cos(u_i - u_j)\right) + \left(\frac{h}{2\pi}\right)^2 (u_i - u_j)^2}}, \qquad (1.6)$$

with g the coupling constant between the interacting particles (In standard Coulomb systems $g = q^2/(4\pi\varepsilon_0)$.). The transformation to arc-length coordinates is in this case of confinement very simple, given just by a scaling factor $s_i = \sqrt{r^2 + (h/2\pi)^2}u_i$. Evidently, the effective two-body potential is only a function of the relative coordinates $u_i - u_j$ (or equivalently $s_i - s_j$), leading to center-of-mass separation, in agreement to [O2]. Similarly to the dipolar case, it has an oscillatory character with a tunable number of minima, depending on the pitch-to-radius ratio $\frac{h}{r}$ (Fig. 1.2 (b)). In particular, both the number and the depth of the minima increase as $\frac{h}{r}$ decreases. This behaviour can be explained by the fact that for decreasing $\frac{h}{r}$ the helix (Eq. 1.5) behaves less as a straight line and more as a circle. Opposite to the case of dipoles, for charges all the $\frac{h}{r}$ provide a repulsion at short distances and the value of the potential minima decreases with the distance (Fig. 1.2 (b)).

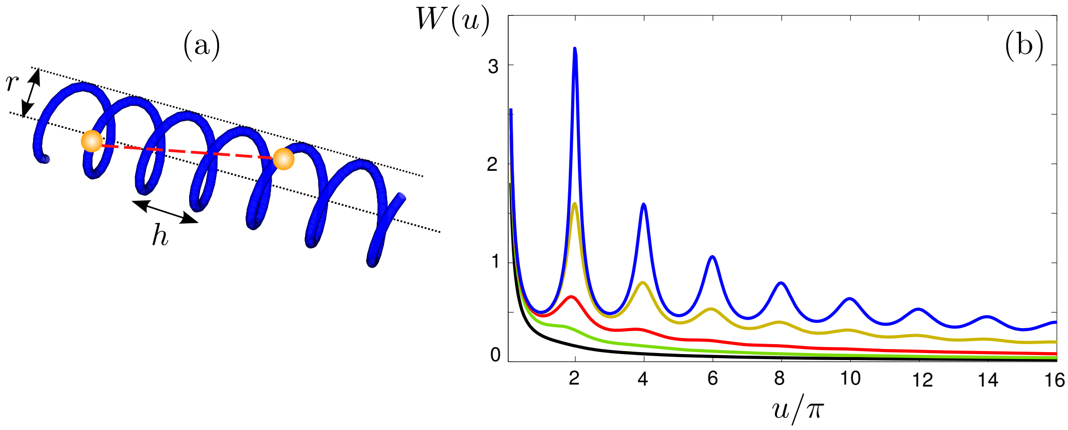

Figure 1.2: (a) Two particles confined on a homogeneous helix of radius r and pitch h. The red dashed line illustrates the Euclidean interparticle distance. (b) The effective two-body potential W as a function of the angular separation $u = u_i - u_j$ measured in units of π for different values of the geometrical parameters corresponding from bottom to top to $\frac{h}{r} = 2\pi$ (black line), π (green line), $\pi/2$ (red line), $\pi/5$ (dark yellow line), $\pi/10$ (blue line)

Although the underlying interactions are purely repulsive, the helical constraint allows, by inducing minima to the two body potential, for the creation of classical bound states. These occur at angular separations which are approximately odd multiples of π with maxima arising for even multiples (Fig. 1.2 (b)). This fact generically prohibits the formation of chains for more than two particles, since an equidistant chain configuration would cause the second neighbours to be in a potential maximum. The many body problem, therefore, is expected to be very complex, with a plethora of different stable configurations appearing already in the few particle case [38]. Moreover, the two-body quantum case reveals (following the arguments of the classical problem) that electron pairs can be formed, which can tunnel through the potential barriers [36]. However, the tunneling probability is very small, except for extreme values of $\frac{h}{r}$, making such a system a good candidate for studying, among others, a Bose gas of stable bi-electron molecules.

To summarize, we have seen that a helical confinement of long-range interacting particles can lead to very interesting phenomena closely connected with the appearance of a rather unconventional two-body potential of oscillatory character (Fig. 1.2 (b)), hardly found in other systems. This form of the potential can be viewed as a result of the interplay between the confined motion on a 1D manifold and the interactions taking place in the full 3D space, a fact allowed due to the non-trivial geometry of the system (Fig. 1.2 (a)). Especially for repulsively interacting charged particles, this can lead to the formation of bound pairs, a rather surprising result. Motivated by these findings we have studied some extensions of such systems, consisting of different confining manifolds of helical character, as well as, of a large number of charged particles. The outline and a brief discussion of our results will be the subject of the next section, whereas our full works can be found in Chapter 2.

1.5 Outline of scientific contribution II: *Charges on helical manifolds*

We will now review the main part of our scientific contribution, concerning the dynamics and equilibrium of singly charged particles confined in different helical traps. As mentioned above, these constitute low dimensional systems with strong long-range interactions, which, although rarely studied in the literature, are found to exhibit intriguing properties, the most striking one being the tunable oscillatory form of the two-body potential felt by two charges confined on a homogeneous helix. Starting again with a two-body problem of charges, though now confined on an inhomogeneous helix [O2], we study their scattering properties and the possibility of pair formation in the system (Sec. 1.5.1). Already for two ions, the dynamical processes induced by the geometrical inhomogeneity are very complex and allow for an energy exchange between the center-of-mass and the relative degree of freedom.

We then proceed to studies of the many-body system [O3, O4] by increasing the number of trapped charges. The complexity, as measured by the number of the possible equilibrium states, is now vastly increased, making it extremely challenging to identify the true ground state of the system for arbitrary parameters. This task becomes more feasible for certain commensurate fillings of the helix, on which we then focus, in our analysis. We here find that the system undergoes a linear-to-zigzag transition by tuning the geometry of the trap (Sec. 1.5.2), bearing similarities with the structural transitions found in other trapped ion systems (Sec. 1.1.2). A study of the linearized behaviour of the system in the parameter region below the transition shows that the vibrational band structure deforms in a most unconventional manner during the change of the trap geometry, passing through a stage of large degeneracy for certain parameters. Remarkably, such a degeneracy permits small-amplitude localized excitations to propagate in time without significant spreading.

Motivated by this rich linear behaviour, we continue in Sec. 1.5.3 by examining the response of our system to nonlinear excitations. Since the physics connected to nonlinear phenomena is quite different from that of the more known linear case, we provide a brief introduction to the field in the beginning of this section, focusing on studies of non-linear models with a non-trivial geometry. We then proceed with discussing our findings [O4], which reveal qualitatively different features in the nonlinear regime. In particular, we show that different nonlinear behaviours can be encountered depending on the trap geometry, the most notable being the focusing of a broad excitation at the point of degeneracy of the setup. Within the same parameter regime an effective discrete nonlinear Schrödinger model is constructed, allowing for the insightful identification of a number of breather-like excitations.

1.5.1 Two-body scattering of charges on an inhomogeneous helix

As previously mentioned, the homogeneous helix (including the circle and straight line limits) is the only motional constraint which enables separation of center-of-mass from relative coordinates for two particles interacting in dependence of their Euclidean distance. This is proven in our work in Ref. [O2], to be reviewed in this subsection. The proof is based on the fact that, for the separation to occur, the confining curved manifold should be generated by a sign preserving isometry of three-dimensional Euclidean space, denoted $\mathbb{R}^3$. The only available sign preserving isometries in $\mathbb{R}^3$, also called Euclidean moves, are the screw operation (combined translation and rotation), the rotation, and the translation, generating a homogeneous helix, a circle, and a line, respectively.

In the case of confinement on a uniform helix we saw that an effective oscillatory two-body potential emerges and that the charges can form classical bound states. The natural question which then arises is what the effects of a confinement on an inhomogeneous helix would be, especially the effect caused by the coupling of the center-of-mass to the relative coordinates. Our investigations here aim at an answer to this question.

We study a system of two identical charges confined on a helix with a Gaussian deformation of its radius $r = r(u)$ [4] and a constant pitch h (Eq. 1.5). Such a helix is almost homogeneous away from the the localized hump around the center. The geometric parameters r, h are chosen such that the effective interaction potential exhibits three minima in terms of the relative coordinate s in the homogeneous regime. The full

---

[4] To maintain coherence in this introductory section, we use r to denote the radius of the helix instead of R as in Ref. [O2].

potential landscape is bent downwards for small values of the center-of-mass coordinate S, following the behaviour of the helix inhomogeneity.

We start in the homogeneous regime with a bound pair of particles of zero relative velocity ($\dot{s}$=0) located in the minimum of the first potential well, and record the outcome of their scattering through the hump after a long time for different values of their center-of-mass velocity $\dot{S}$. Without the inhomogeneity, we would expect the particles to remain bound forever in the minimum of the potential well. The local deformation, however, allows for a region (inside the inhomogeneity) of coupling between the center-of-mass and relative coordinates, causing an energy transfer between the two degrees of freedom. Thus, a part of the initial center-of-mass kinetic energy can be transfered to the relative motion, giving enough energy to the particle pair to become unbound after passing through the deformation. We have found that the initial center-of-mass kinetic energy should lie within a certain interval of intermediate values for this dissociation to occur. For smaller values there is not enough energy supply, whereas for larger values the dwell time in the inhomogeneous region is too small to permit a substantial coupling. Due to the time reversal symmetry of our Hamiltonian system, this leads to the conclusion that, for certain initial conditions, unbound charged particles can become bound to each other during their motion. In other words, particles can form bound pairs while being scattered through the helix, which is a counterintuitive fact, especially regarding the long-range repulsive character of the underlying interactions.

The regimes of dissociation (in terms of initial center-of-mass energy) are identified for different initial conditions and found to exhibit similar features. An important outcome of this analysis is that the energy transfer mechanism depends in a very complex manner on the initial conditions: Indeed, it does not take place in a single step; it is rather the final result of a continuous energy redistribution during the time interval in which the particles remain inside the inhomogeneity. We complete our analysis of this two-body problem with a study of its phase space. Since the system is Hamiltonian with two degrees of freedom, we employ Poincaré surfaces of section, which, taking advantage of the conservation of energy, permit to illustrate 2D cuts of the phase space. For low total energies, exclusively regions of regular bounded motion within the hump are found. As the total energy increases, escaping trajectories emerge which reside within disconnected empty regions in the Poincaré surfaces of sections. Except for certain localized bound states inside the inhomogeneity, we also identify "resonant trajectories", i.e. trajectories that remain inside the hump performing an oscillatory motion for a large time interval and finally escape into the homogeneous region.

These intriguing results on two-body dynamics of charged particles in a helical trap call for a study of many-body systems trapped in helical geometries. This examination is carried out in the following subsections, using as confining manifold a closed helix in order to simplify the theoretical framework for the many-body system.

1.5.2 Many-body problem of charges on a closed helix I: *Equilibrium and linearized behaviour*

Having demonstrated the many aspects of the two-body problem of helically confined charges, both in presence (Sec. 1.4) or absence (Sec .1.5.1) of separation of center-of-mass from relative coordinates, we now gradually proceed to the study of its many-body counterpart. As a many-body problem of singly charged trapped particles, such a system is intrinsically connected with the physics of cold ions and Wigner crystals (Sec. 1.1). In fact, any crystalline equilibrium configuration of the system, and especially its ground state, may be considered as a type of Wigner crystal.

The study of Wigner crystallization for a finite number of particles requires a finite trap. In the present context, such a trap could be provided by a finite helical segment, equivalent to a box potential, or by an external harmonic potential imposed on the infinite regular helix. As seen in the simplest 1D case of a line (Sec. 1.1.1, Sec 1.2), however, these approaches both induce a non-trivial inhomogeneity in the Wigner crystal, prohibiting, among others, the existence of phononic excitations. In our attempt to study the simplest possible many-body system of helically confined charges free from any finite-size effects, we have therefore chosen a closed helix as the confining manifold. Specifically, we consider a *toroidal* helix which has, in addition to the helix radius r and pitch h, one more geometrical parameter, the (major) radius of the torus R controlling the overall size of the manifold [O3, O4]. Such an unconventional system geometry can in fact be found naturally in the DNA of viruses, plasmids or mitochondria [216, 217], in the form of DNA condensates [218], in bacteriophages [219] or proteins [220]. It is also connected to optimal packing [221] and gyrotropic behaviour [222], making it an relevant structure in material science.

In our work in Ref. [O3] we assume N identical particles interacting via Coulomb interactions and constrained to move on such a toroidal helix. In the limit of vanishing helix radius ($r = 0$) we obtain the geometry of a ring. In this case, a separation of the center-of-mass is provided and the system possesses a single stable state (up to global translations) consisting of an equidistant polygonic configuration of charges. For finite values of the radius r, the situation is radically different. The center-of-mass couples to the relative coordinate and a plethora of different equilibrium states emerge, depending on the parameters h, r, R. These crystalline configurations are generally non-periodic and contain multiple defects, that is localized formations deviating from the surrounding order. There exist, however, particular cases where the symmetry does allow for a periodic equilibrium configuration, similar to the one in the ring limit. These satisfy the requirement of commensurability between the number of particles N and the number windings $M = 2\pi R/h$ so that $M = nN,\ n = 1, 2, 3, \ldots$. For a fixed filling $\nu = 1/n$, a specific value of the pitch h and a fixed number of particles, the helix radius r becomes the only free parameter of the problem. We thereby study the ground state configurations of such commensurately filled closed helices as a function of r.

We find that the polygonic configuration of the ring persists as an equilibrium state of the system for any r. For small values of r it constitutes the ground state, with the particles located along the outer circle of the torus. As the helix radius increases, this state loses its stability at a critical point r_{cr} and bifurcates to a zigzag configuration. Thus, by tuning a parameter of our trap (the radius r) we encounter a zigzag transition. This is reminiscent of the structural zigzag transitions encountered for cold ions in Paul traps by tuning the aspect ratio of the confinement (Sec. 1.1.2), with a fundamental difference: In the usual Paul traps, the zigzag transition is driven by an increment of dimensionality of the system from 1D to quasi-1D, controlled by the transverse trapping potential. In contrast, the system examined here, although interacting via 3D space, always remains strictly 1D in terms of the single-particle configuration space. This fact has significant impact on the low energy excitations of the system, namely the phonon spectrum, as discussed next.

In the absence of a second dimension, the phonon spectrum, extracted by a linearization of the many-body potential around the ground state configuration, consists only of longitudinal branches. Below the critical radius r_{cr} it consists of a single branch, whereas after the pitchfork bifurcation takes place, it forms two branches reflecting the broken symmetry of the new ground state. In contrast to what is seen in usual cold ionic systems (Fig. 1.1 (b),(c)), the longitudinal phonon branch varies drastically with the tuning parameter (the helix radius r). Starting from the ring case ($r = 0$) with a gapless center-of-mass mode, portraying the separation from the relative motion, for increasing r the phononic band structure deforms opening a gap and decreasing its overall width. At a special value $r = r_d$ the width of the spectrum becomes so concentrated (with width of the order of 10^{-4} compared to 10^{-1} for $r = 0$) that it is practically degenerate, and the corresponding band structure is flat. Above r_d the band structure inverts with the out-of-phase mode becoming energetically favourable. The spectral width then increases again up to the critical point r_{cr} where the out-of-phase mode reaches zero, thereafter crossing the imaginary axis and generating the zigzag transition.

Such a band structure deformation, controlled by the trapping geometry, is rather unconventional for Wigner crystals, since it requires the interaction and the motion to take place in spaces of different dimensionality. Here, the interaction space is 3D, making a zigzag structure energetically favourable beyond a critical radius. A transition to a zigzag phase is usually achieved by a softening of the out-of-phase mode of the transverse branch of the frequency spectrum, which has always an inverted form (Fig. 1.1 (b),(c)). This branch shifts and changes its width, with the out-of-phase mode reaching zero at the critical point (Fig. 1.1 (c)), while the longitudinal branch remains unchanged. In our system a transverse branch is missing due to the reduced dimensionality of the single-particle motion. Thus, the longitudinal branch, being the only allowed, needs to undergo a significant change, including an inversion, in order to lead to the transition.

A remarkable effect of the geometry is the deformation of the band structure through the point of very large degeneracy (flatness) for $r = r_d$. At this radius the interactions are effectively screened and the charges act almost as independent within linear approximation. Consequently, a localized excitation with small amplitude can remain localized up to long times in this configuration without propagating to the other particles in the crystal. This is opposite to what is encountered for different values of the radius r or to what is expected for a crystalline structure in general. The connection of the propagation speed of a small localized excitation to the radius of the helix results from the connection of the latter to the phononic spectrum. In particular, the propagation speed is found to depend monotonically on the overall width of the linear spectrum. As a last remark, we note that most results described in this section have been produced with $N = 60$ particles and filling $\nu = 1/2$. Predictions about the thermodynamic limit can be found in Ref. [O3] and in the Appendix, where also different fillings are treated.

Having constructed a system with such a peculiar linear behaviour, controlled by a geometrical parameter, we continue with examining its response to nonlinear excitations for different geometries. An overview of our findings in Ref. [O4] as well as a brief introduction to the physics of relevant nonlinear systems will be the subject of the following section.

1.5.3 Many-body problem of charges on a closed helix II: *Dynamics of nonlinear excitations*

Already the linear dynamics of the system were seen to display remarkable features such as a geometry-dependent deformation of the linear spectrum with a region of very high degeneracy. It is then natural to ask how the many-body system responds to *nonlinear* excitations. We here outline the results concerning the dynamics of nonlinear excitations for charged particles confined along a toroidal helix. As in the setup described in the previous section, the helix is commensurately filled with charges and the helix radius attains values below the critical one for the zigzag transition, i.e. the ground state of the system is the equidistant polygonic configuration. Before proceeding to an overview of our results, we first briefly outline basic relevant aspects of nonlinearity, focusing on the discrete nonlinear Schrödinger (DNLS) equation which we use as an effective model in this work.

Nonlinearity and the DNLS Equation

Whereas a linear behaviour leads in general to a simple description of a system dynamics in terms of its constituents based on the principle of superposition, nonlinearity causes a complex dynamical behaviour in which often the cause and its effect cannot be separated. Such feedback loop processes are inherent in nonlinear systems and can lead to effects such as self-focusing (or self-trapping) of initial wave packet excitations [223,224] or to the existence of spatially localized excitations which do not spread in the course of evolution such as breathers and kinks [225,226]. In contrast, for linear systems the time evolution of excitations is always characterized by some degree of dispersion and the only elementary excitations are phonon-like extended modes.[5] It is the counteraction of the nonlinearity to the linear dispersion that makes a self-focusing effect possible. Such an interplay between nonlinearity and dispersion was first examined in studies of

---

[5] The discussion in this paragraph refers only to periodic systems. The inclusion of disorder is known to lead to excitation localization, termed Anderson localization, even in linear systems.

continuous integrable models such as the Korteweg-de-Vries (KdV), the sine Gordon (sG) and the nonlinear Schrödinger (NLS) equations.

Studies of nonlinear discrete systems were found to exhibit similar effects, allowing for even more complex dynamics, due to the boundedness of their frequency spectra. A prototype model of such systems is the DNLS equation [227], consisting, in analogy to its continuous counterpart (NLS), of a linear coupling ϵ and a cubic nonlinear term (γ), reading in 1D

$$i\frac{d\Psi_n}{dt} = \epsilon\left(\Psi_{n+1} + \Psi_{n-1}\right) + \gamma\left|\Psi_n\right|^2 \Psi_n. \tag{1.7}$$

This equation describes the time evolution of the amplitude of the excitation envelope $\{\Psi_n\}$ for a simple lattice model of coupled anharmonic oscillators. It can lead to different dynamical behaviours depending on the relative sign between the dispersion and the nonlinear coefficient. In particular, if $\epsilon\gamma > 0$ it describes a self-focusing dynamics (focusing DNLS) supporting bright solitons (localized solutions in form of density peaks), whereas if $\epsilon\gamma < 0$ it leads to defocusing (defocusing DNLS) and is found to support dark solitons (localized solutions in a uniform background, forming density dips). The focusing case can be understood as a result of the so-called attractive nonlinearity counteracting the dispersion, contrary to the defocusing case where the so-called repulsive nonlinearity enhances the dispersion effect.

Apart from cases of nonlinear oscillator chains, the DNLS equation is also used to model different systems such as coupled optical waveguides [228, 229], Bose-Einstein condensates [230, 231], or even the dynamics of DNA molecules [232–234]. In the latter case an explanation of the denaturation of the DNA is attempted by relating the local openings of the double helical strand to localized solutions (intrinsic localized modes) supported by the so-called Peyrard-Bishop model [234].

In all these models a trivial lattice geometry is commonly assumed, given in 1D by a straight equidistant chain with couplings restricted to nearest-neighbours. The consideration of different lattice geometries in the context of long-range interacting oscillators on a curved substrate [235], curved polymer chains [236], or descriptions of the DNA dynamics which take into account its prominent helical structure [237], have shown that the interplay between nonlinearity and geometry can lead to striking phenomena including the emergence of multistability or the enhancement of the stability of discrete breathers. Moreover, a non-trivial geometry was even found capable of inducing nonlinearity in harmonic oscillator chains [238, 239]. It is therefore of fundamental interest to study the way in which geometry affects nonlinearity in a system with a non-trivial geometry, as realized here in the charges-on-a-helix system. An outline of our results concerning its response to nonlinear excitations [O4] can be found below.

Nonlinear effects in the many-body toroidal helix model

In the parameter regime where the ground state configuration is that of equidistant repulsive particles on the toroidal helix, we excite the system by giving some relatively small initial kinetic energy to the particles. The energy distribution of the excitation is relatively broad with a Gaussian spatial profile. We then examine how this excitation evolves within the system at long times for different values of the helix radius, covering all regions with qualitatively different linear spectra: from the ring limit to the degeneracy and the inversion regime (see Sec. 1.5.2).

Our numerical results [O4] show that the excitation evolves in a very distinct manner in the different geometries. For small helix radii, it spreads into the whole crystal while periodically refocusing at time instants where its left and right parts meet and superimpose at the diametrically opposite point of the toroidal helix. In contrast, for a narrow range of helix radii where the multiply degenerate linear spectrum was encountered, the excitation self-focuses after a long time interval and finally fragments into a number of highly localized excitations. Beyond this regime, the excitation is again gradually dominated by dispersion, thereby defocusing and spreading into the crystal. The self-focusing of the excitation at the degenerate geometry signifies, according to the discussion above, the existence of a strong nonlinearity in the system.

In order to identify and quantify the leading orders of such a nonlinearity, we perform a Taylor expansion of the full interaction potential around the equilibrium configuration up to fourth order. The resulting Euler-Lagrange equations contain quadratic and cubic nonlinear forces in addition to the harmonic ones. At the ring limit ($r = 0$), where the separation of the center-of-mass holds, these equations are of the Fermi-Pasta-Ulam type [240] with long-range couplings. Close to the regime of degeneracy, the equations are dominated by the linear diagonal term. By use of the rotating-wave and the nearest-neighbour approximations, we here derive an effective DNLS equation with additional nonlinear couplings describing the time evolution of the excitation envelope. The predictions of this equation for the time evolution of the excitation capture nicely the results of our full model. Indeed, within the degeneracy region the DNLS is of the focusing type with a very large effective nonlinearity, whereas beyond this region it becomes of the defocusing type, in accordance with our observations. Crucial for this effect is the contrast between the robustness of the nonlinear coefficient and the variability of the linear coupling. The latter crosses zero at the degeneracy, thus shifting the weight of the dynamics to the nonlinear terms, and becomes negative beyond it, leading to the defocusing dynamics. Finally, with the effective DNLS model we are able to identify certain breather-like excitations in our system of charges for the degenerate geometry. These excitations oscillate in time but retain their localized profile during the evolution, adding to the nonlinear dynamical features of the system.

Chapter 2

Scientific contributions

2.1 Ion chain in a 1D box

PHYSICAL REVIEW E **87**, 042116 (2013)

Finite-temperature crossover from a crystalline to a cluster phase for a confined finite chain of ions

A. V. Zampetaki,[1] F. K. Diakonos,[2] and P. Schmelcher[1,3]

[1]*Zentrum für Optische Quantentechnologien, Universität Hamburg, Luruper Chaussee 149, 22761 Hamburg, Germany*
[2]*Department of Physics, University of Athens, GR-15874 Athens, Greece*
[3]*Hamburg Centre for Ultrafast Imaging, Luruper Chaussee 149, 22761 Hamburg, Germany*

(Received 22 September 2012; revised manuscript received 29 March 2013; published 17 April 2013)

Employing Monte Carlo simulation techniques we investigate the statistical properties of equally charged particles confined in a one-dimensional box trap and detect a crossover from a crystalline to a cluster phase with increasing temperature. The corresponding transition temperature depends separately on the number of particles N and the box size L, implying nonextensivity due to the long-range character of the interactions. The probability density of the spacing between the particles exhibits at low temperatures an accumulation of discrete peaks with an overall asymmetric shape. In the vicinity of the transition temperature it is of a Gaussian form, whereas in the high-temperature regime an exponential decay is observed. The high-temperature behavior shows a cluster phase with a mean cluster size that first increases with the temperature and then saturates. The crossover is clearly identifiable also in the nonlinear behavior of the heat capacity with varying temperature. The influence of the trapping potential on the observed results as well as possible experimental realizations are briefly addressed.

DOI: 10.1103/PhysRevE.87.042116 PACS number(s): 05.20.−y, 64.60.an, 64.70.−p, 37.90.+j

I. INTRODUCTION

Within the past decade, we have witnessed enormous progress with respect to the controlled manipulation of ions. This is in particular due to the application of the dynamics of ionic systems to spectroscopy [1,2], the implementation of quantum simulations [3,4], and the realization of quantum information processors [5,6]. In this context many trapping methods [7–11] have been suggested. Among the most widely used is the Paul trap [9], which allows one to monitor single ions [12] and study the stability of many ion crystals [13–15]. Experimental studies of ions confined in this type of trap have shown a transition from a cloud of ions to a crystalline structure with decreasing temperature [16,17].

Along with the experiments there have also been various theoretical investigations in the formation of Coulomb crystals in the presence of a trapping potential. An early study of the structure of spherical Coulomb crystals [18] showed that particles are arranged in concentric spherical shells with constant intershell distances and a hexagonal surface structure. Furthermore, for large systems a bcc lattice is formed in the interior [19] resembling the case of infinite Coulomb systems (One Component Plasma) [20]. The two-dimensional (2D) case has revealed even more exotic phenomena. Specifically, for the cylindrically confined Coulomb lattice a structural phase transition with increasing linear density has been found [21]. The finite 2D systems of charged particles confined in a parabolic potential or a box present an order-disorder phase transition with increasing temperature [22]. The density of the particles differs for the two potentials being almost constant in the inner region and decreasing while moving outwards for the parabolic case, whereas it increases radially forming distinct shells for the box.

Recently, particular interest was dedicated to the study of one-dimensional (1D) systems and especially cold ions confined in a corresponding harmonic potential [23–28]. Analytical approaches have been developed using perturbation theory around the classically minimum energy positions [25,26]. An interesting thermodynamic behavior different from both the 2D and three-dimensional (3D) cases has been observed due to the interplay between the long-range interactions and strong correlations. These observations include a deviation of thermodynamic quantities from extensivity, a nonuniform charge density, and a structural phase transition (linear to zig-zag) driven by the strength of the radial potential [27] and temperature [28].

Following the direction of the above studies, the present paper aims at describing classically the thermodynamic behavior of equally charged particles confined to an 1D box within a wide temperature range. Such a problem is usually treated by computing the partition function of the system:

$$Z(L,N,T) = Z_{\mathrm{KE}} Z_U,$$
$$Z_U = \int_0^L \cdots \int_0^L \exp[-\beta V_C(x_1,\ldots x_N)]dx_1 \ldots dx_N, \quad (1)$$

where Z_{KE} is the part of the partition function due to the kinetic energy of the particles, $\beta = 1/k_B T$, g^2 the coupling constant, and

$$V_C(x_1,x_2,\ldots x_N) = \frac{1}{2}\sum_{\substack{i=1\\ i\neq j}}^{N}\sum_{j=1}^{N}\frac{g^2}{|x_i - x_j|} \quad (2)$$

the Coulomb potential energy. Since Z_U is not analytically accessible, we will proceed here by utilizing Monte Carlo simulation techniques.

Examining the distributions of the spacing between the particles with increasing temperature, we will observe a transition from a discrete overall asymmetric form to a continuous exponential one. This fact can be interpreted as an evidence for a crossover from a crystalline to cluster phase at a transition temperature T_c, at which this distribution acquires a symmetric Gaussian form. The probability of forming clusters of increasing size increases with the temperature and finally saturates. We will then proceed and verify the crossover by the temperature dependence of the heat capacity. Our results indicate that the transition temperature T_c and consequently every thermodynamic quantity depends on the number of particles N and the length L of the box in an independent manner, thus presenting deviations from extensivity. An implementation of this nonextensivity in order to obtain finite quantities in the thermodynamic limit is attempted. We also discuss the effect of the trapping potential on the observed results.

The paper is organized as follows. In Sec. II we present, in some detail, the Monte Carlo methods used in our simulations. Section III contains our results and a discussion of the observables used to characterize the statistical mechanics of the Coulomb system. In Sec. IV we analyze the changes of the observed properties when trapping conditions are altered, focusing on the case of harmonic trapping. Finally, Sec. V provides a brief summary of our findings commenting on a possible experimental realization.

II. MONTE CARLO APPROACHES TO THE FINITE ION CHAIN

In order to explore the statistical properties of the finite Coulomb chain confined in a box we employ the Metropolis and Wang-Landau algorithms, each possessing a better efficiency with reference to the computation of different quantities in different temperature regimes. In order to be self-contained, we will provide below a brief description, discussing their advantages and deficiencies and explaining how they are employed in this work. Before doing so, it is important to notice that for a given number N of particles in the box the statistical properties of the Coulomb chain are determined by a single dimensionless parameter $\Lambda = \frac{g^2}{Lk_BT}$. This is seen by introducing the dimensionless variables $\xi_i = \frac{x_i}{L}$ in Eq. (2) and inserting the resulting expression in the partition function (1). In the following we will exclusively use the dimensionless position variables ξ_i. As a consequence the length of the box can be taken without loss of generality as $L = 1$.

For the Metropolis algorithm [29] we generate initially a random configuration $\{\xi_i\}$ of the location of the particles in the box. The configuration is sorted in an ascending order ($0 \leqslant \xi_1 \leqslant \xi_2 \leqslant \cdots \leqslant \xi_N \leqslant 1$). Then we choose for the jth particle a new position $0 \leqslant \xi_j' \leqslant 1$. The efficiency of the algorithm is greater if we impose the additional restriction $\xi_{j-1} \leqslant \xi_j' \leqslant \xi_{j+1}$. If $\Delta E = V_C(\xi_i') - V_C(\xi_i) \leqslant 0$ the new configuration is accepted, i.e., $\xi_j = \xi_j'$. Otherwise we accept the new configuration with a probability P given by the Boltzmann factor $P = e^{-\beta\Delta E}$. This procedure defines a Monte Carlo step and after a considerable number of repetitions the equilibrium state is reached. The Metropolis algorithm satisfies the property of detailed balance, and therefore it always converges, being also, as a Markov chain, very efficient in the evaluation of the equilibrium configuration of the particles. However, it presents also some well-known deficiencies. In the low-temperature regime, where the minimum of the potential dominates the statistical properties of the system, the acceptance ratio of Metropolis becomes very low, a fact that leads to a dramatic growth of the simulation time. The situation is even worse when the potential possesses many minima, since the particles can be trapped in one of them and never reach the global minimum. For the strongly correlated system presented here, the main problem arises in the calculation of inherently averaged macroscopic quantities like the heat capacity C_V. A large ensemble of configurations is needed in order to reduce statistical errors significantly, and thus the practical simulations are prohibited.

Recently another algorithm has been proposed in order to overcome these problems, namely, the Wang-Landau algorithm [30]. Contrary to the canonical ensemble-based Metropolis, this algorithm uses the concept of the microcanonical ensemble, and it intends to calculate the density of states (DOS) of a system as described below. First, we choose the range of accessible energies and then divide it into a number of bins M. We start, assuming that we have a uniform density of states $g(E)$, i.e., $g(E) = 1$ for every energy bin. We then proceed as follows. For the jth particle we choose a new position $\xi_{j-1} \leqslant \xi_j' \leqslant \xi_{j+1}$. If $g(E_2) \leqslant g(E_1)$ with $E_1 = V_C(\xi_i)$ and $E_2 = V_C(\xi_i')$, we accept the new configuration. Otherwise the new configuration is accepted with a probability $P = \frac{g(E_1)}{g(E_2)}$. Each time an energy bin is visited we update the corresponding density of states by multiplying the existing value by a modification factor f, i.e., $g(E) = f \cdot g(E)$. We choose $f = e^1 \approx 2.71828\ldots$. We also update the energy histogram $H(E) = H(E) + 1$. In the original version of the algorithm [30] for discrete systems, the above steps were repeated until a flat histogram was obtained [e.g., $\min(H(E)) \leqslant 0.8 \cdot \langle H(E)\rangle$, with $\langle H(E)\rangle$ being the mean value of the histogram]. In order to improve the accuracy which is of order $\ln f$ we decrease the modification factor $f = \sqrt{f}$ and repeat the procedure. When $\ln f \approx 10^{-8}$ the density of states does not any longer evolve any further and the simulation is stopped. The major problem of this algorithm is that it does not satisfy the detailed balance condition, and so its convergence cannot be strictly proved. Furthermore the method has been suggested originally for discrete systems with narrow energy landscapes. Nevertheless it has been used successfully in recent calculations also considering continuous systems [31–33]. If the low-energy spectrum of the system is complex, the criterion of the flatness of the histogram is never satisfied as some energy bins are never visited. To overcome this problem several alternatives have been proposed [33,34]. In our work we use the technique described in Ref. [34] excluding some boundary bins from the flatness check. The Wang-Landau algorithm has the special advantage that once the DOS is obtained, we can easily derive all the thermodynamic quantities [e.g., $Z = \sum_E g(E)e^{\beta E}$] from this function alone. Thus, the simulation time is significantly reduced when computing the temperature dependence of demanding quantities like the heat capacity C_V. However, for computing properties that depend on the position of the particles for systems with a complex, degenerate, and unbounded energy landscape as the one presented here, this method is in an inferior position in comparison to Metropolis. This is attributed to the large computational effort needed in order to find a representative sample of microstates for each energy E. In order to exploit the advantages of each algorithm avoiding its drawbacks, we use both of them and apply each one for the evaluation of different properties.

In the present study 1.5×10^7 MCs were required in order to reach equilibrium with the Metropolis algorithm and an ensemble of 200 configurations in order to obtain the mean energy $\langle E\rangle$ as a function of Λ and the number of particles

N. For quantities related to the positions of the particles at equilibrium the size of the ensemble was increased up to 10 000 configurations to achieve better statistics. The Wang-Landau algorithm has been realized with 2×10^7 MCs for each value of the modification factor until $\ln f \approx 10^{-8}$ as stated above. In most calculations the number of particles $N = 100$ is used unless stated otherwise.

The spatially resolved density and correlation functions, as well as $\langle E(N) \rangle$ have been computed with the Metropolis, whereas the heat capacity $C_L(\Lambda)$ has been determined using the Wang-Landau algorithm. As a check, the dependence of the mean potential energy $\langle E(\Lambda) \rangle$ on the parameter Λ has been computed with both approaches.

III. NUMERICAL RESULTS AND DISCUSSION

We present and describe in the following our basic results for the temperature-dependent behavior and properties of the ions in the box. Let us begin with the exploration of the minimum energy configuration (in the first subsection) and continue with its temperature dependence (in the second subsection). In the last subsection, which addresses the main results of this work, evidence for the crystalline-clustering crossover and the associated phenomenology is presented.

A. Minimum energy configuration

Some useful remarks on the minimum energy configuration of the ions in the box can be obtained simply by inspection of the corresponding Coulomb potential energy. First, $V_C(\xi_1,\xi_2,\ldots,\xi_N)$ is obviously a strictly increasing function of ξ_1 ($\frac{\partial V}{\partial \xi_1} > 0$) and a strictly decreasing function of ξ_N ($\frac{\partial V}{\partial \xi_N} < 0$). Thus, the first and the last particles always occupy the edges of the line segment, i.e., $\xi_1 = 0$ and $\xi_N = 1$. It is obvious that the problem possesses a symmetry axis with respect to the center of the box. As a result, if the number of particles N is odd, the central particle is positioned at the center of the line segment ($\xi_{\lfloor N/2 \rfloor + 1} = 1/2$, where $\lfloor x \rfloor$ denotes the floor function of the number x). Furthermore, for more than three particles the minimum energy configuration is not the equidistant one. In fact, the difference $\Delta_{\text{eq}}\xi_i = \xi_i^0 - \xi_i^{\text{eq}}$ with $\{\xi_i^0\}$ the equilibrium positions of the particles at zero temperature and $\{\xi_i^{\text{eq}} = \frac{i}{N-1}\}$ the equidistant positions is a discretization of a smooth function, inversion symmetric with respect to the center position $N/2$ possessing a minimal value at $i_{\min} \lesssim N/4$, a maximal value at $i_{\max} \gtrsim 3N/4$, and being almost linear within $[i_{\min}, i_{\max}]$ (Fig. 1). Due to the fixed length of the box and the long-range character of the interactions, the particles tend to accumulate at the edges of the box leaving larger interspace distances in its middle part [Figs. 2 and 3(a)]. This is opposite to the case of ions confined in an 1D harmonic potential [23,26] where the length of the chain is not fixed and the particles tend to accumulate in the inner region. Such a behavior could be expected as the 1D analog of the 2D system presented in Ref. [22]. In the specific case of the 1D system with the first and the last particle fixed at the edges, it can be proven (see the Appendix) that due to the ordering of positions, the lowest energy configuration presented here provides the only minimum of the potential energy. This is in contrast to systems in higher dimensions, such as 3D ionic systems under harmonic confinement, where many local minima and multiple isomers exist [35].

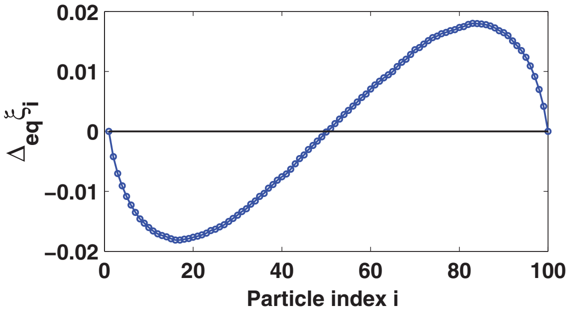

FIG. 1. (Color online) The difference of the expected equidistant position of each particle from its minimum energy position as a function of the index of the particle for $N = 100$ particles confined in a box with unit length $L = 1$.

B. Temperature dependence of the configurations and the densities of charges

To study the temperature dependence of the observables describing the properties of the charged particles in the box we have to vary the parameter Λ. We define $\frac{g^2}{L} = k_B T_0$ yielding $\tau = \frac{1}{\Lambda} = \frac{T}{T_0}$ as a reduced temperature. As τ increases, positions different from the minimum energy ones become accessible to the particles. At temperatures $\tau \gtrsim 10$ the particles start to form clusters of different sizes [Fig. 3(b)]. Thus the form of the possible particle configurations changes dramatically. However, if we consider the mean positions of the particles [Figs. 3(c) and 3(d)] over an ensemble of 10^4 configurations we observe that for the high-temperature case [Fig. 3(d)] the clustering is averaged out, and the resulting mean configuration resembles very much that of the low-temperature regime [Fig. 3(c)]. A slight difference, however, is that for high temperatures the positions seem closer to the equidistant ones with less accumulation at the edges of the box, which are no longer occupied.

The properties of the mean equilibrium configuration for different temperatures can be further explored by considering the temperature dependence of the quantity $\langle \Delta_{eq}\xi_i \rangle$ and the density function $\langle \rho(\xi) \rangle$. As seen in Fig. 4 for temperatures $\tau \leqslant 1$ the mean positions of the particles are identical with the minimum energy ones (Fig. 1). Even at $\tau = 10^2$ (black line

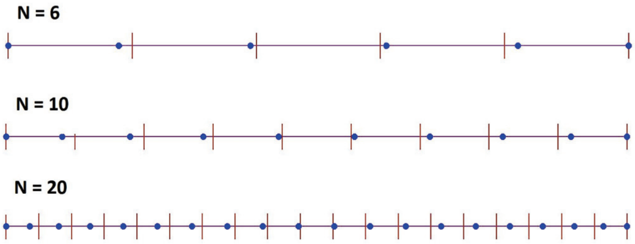

FIG. 2. (Color online) The minimum energy configurations of particles as obtained by the minimization of the potential $V_C(x_1,x_2,\ldots,x_N)$ for $N = 6, 10$ and 20. The particles are represented with the (blue) full dots, and the equidistant positions are marked with the (red) vertical line segments.

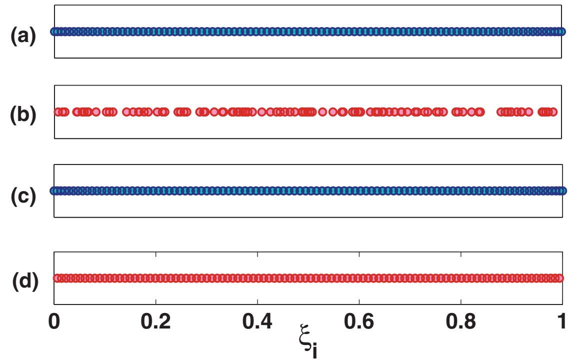

FIG. 3. (Color online) Particle configurations for $N = 100$: (a) A single configuration of particles at $\tau = 10^{-3}$, (b) the same for $\tau = 10^3$, (c) the mean configuration of particles for $\tau = 10^{-3}$, (d) the same for $\tau = 10^3$.

with circles) the form of $\langle \Delta_{eq}\xi_i \rangle$ is preserved except from a decrease in its magnitude and a deviation at the edges. However, for $\tau = 10^4$ the form becomes linear keeping the symmetry around the center but changing by an overall sign.

A reference to the density of the absolute positions ξ_i would be of no practical use since, due to the finite number of particles, the problem is discrete, and it would result only in a set of delta functions. In previous studies [23,25,26] there has been a particular interest in the quantity $\Delta\xi_i = \xi_{i+1} - \xi_i$ denoting the interspace distance between successive particles. It has been shown that its inverse is a smooth function of ξ_i and represents the density of ions per unit length. To improve statistics we use the ensemble average of $\Delta\xi_i$, i.e., $\langle \Delta\xi_i \rangle$. Through interpolation, we produce the density of charge $\langle \rho(\xi) \rangle$ in the continuum limit. Our results are presented in Fig. 5 for various temperatures. We clearly observe the nonuniformity at the outer areas (close to the edges) for temperatures $\tau \leqslant 1$ (opposite to what has been observed in Ref. [23]) and an almost uniform behavior for high temperatures except for the region close to the edges where the density becomes zero (not visible in Fig. 5). As expected, there exist large thermal fluctuations in the high-temperature regime.

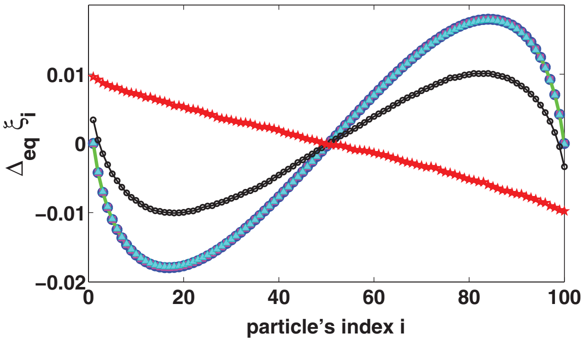

FIG. 4. (Color online) The mean difference $\Delta_{\text{eq}}\xi_i$ of the position of each particle from its expected equidistant position as a function of the particle's index i for temperatures $\tau = 10^{-5}$ (blue circles), 10^{-3} (green line), 10^{-1} (magenta squares), 1 (cyan triangles), 10^2 (black line with circles), and 10^4 (red stars). Note that the $\tau = 10^{-1}$, 1 curves for $\Delta_{\text{eq}}\xi_i$ are on top of those for $\tau = 10^{-5}$, 10^{-3}, and therefore hardly visible.

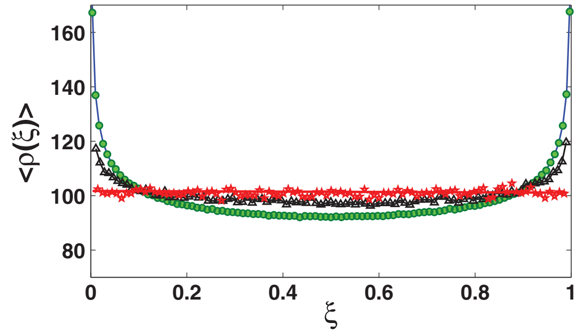

FIG. 5. (Color online) The density of charge $\langle \rho(\xi) \rangle$ as a function of the particles' positions ξ for temperatures $\tau = 10^{-5}$ (blue line), 1 (green circles), 10^3 (black line with triangles), 10^5 (estimated mean red line and fluctuations red stars). The particle number is $N = 100$.

C. Crossover from the crystalline to cluster phase

As has been stated above, the quantity $\Delta\xi_i$ is very useful in the determination of the density of charges $\rho(\xi)$, a continuum limit of the distribution of the equilibrium positions $\{\xi_i\}$. In this subsection we present the results for the distribution of $\Delta\xi_i$, $\rho(\Delta\xi_i)$ at various temperatures (Fig. 6). It turns out that this quantity contrary to $\rho(\xi_i)$ is well defined for this discrete system, and even more, it carries significant information for its thermodynamic behavior. It has been computed through the histograms of $\Delta\xi_i$ for 10^4 configurations and $N = 100$. For low temperatures [Figs. 6(a) and 6(b)] a crystalline structure is observed as $\rho(\Delta\xi_i)$ clearly contains a part formed by discrete peaks for small distances. Thus, the particles occupy well-defined positions leaving specific distances between each other. The mean value of $\Delta\xi_i$ for all the histograms approximately coincides with the equidistant spacing $\langle \Delta\xi \rangle \approx 0.0101 \approx \frac{1}{N-1}$. The most probable value (max $\Delta\xi_i \approx 0.0108$) is slightly larger than the mean, denoting an anticlustering effect and a crystallization of ions. The peaks are broadening and merging with an increase of the temperature, and the overall distribution becomes smoother [Fig. 6(c)]. More positions become accessible to the particles, and the most probable value decreases tending to the mean one. At $\tau = 10$ the form of $\rho(\Delta\xi_i)$ becomes almost symmetric [Fig. 6(d)], and its line shape resembles a Gaussian as is verified by a χ^2 fit (red line). Here max $\Delta\xi_i \approx 0.0097$ is slightly less but actually very close to $\langle \Delta\xi \rangle$. In the high-temperature regime we observe a clustering effect [Fig. 6(e)] directly opposite to that of the low-temperature case. The effect is strongly pronounced as can be seen by inspecting max $\Delta\xi_i \approx 0.0036$, which is much less than the mean $\Delta\xi_i$ value. This trend is enhanced for ultra-high temperatures ($\tau = 10^5$) as illustrated in Fig. 6(f). The most probable value of the spacing is almost zero, and the distribution is well described by an exponential (red line fit with a coefficient of determination $R^2 = 0.9962$ [36]). Its characteristic length scale is approximately 0.0096, which is also close to the equidistant spacing of the particles $\frac{1}{N-1}$. This reflects the fact that for high temperatures the particles have the opportunity to occupy almost every available position, and each particle's position is completely independent from the positions of the neighboring particles. The continuous change of $\rho(\Delta\xi_i)$ implying the transition from a crystalline to a cluster configuration with the change of temperature

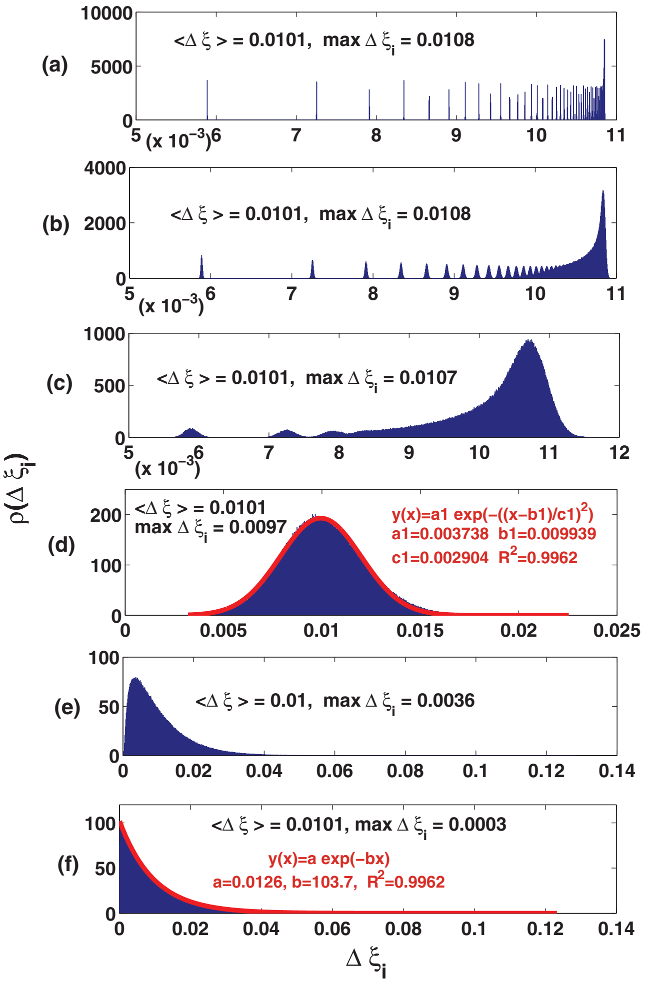

FIG. 6. (Color online) The distributions of $\Delta\xi_i$, $\rho(\Delta\xi_i)$, for different temperatures: (a) $\tau = 10^{-5}$, (b) $\tau = 10^{-3}$, (c) $\tau = 10^{-1}$, (d) $\tau = 10$ (the red line is a Gaussian fit), (e) $\tau = 10^3$, (f) $\tau = 10^5$ (the red line is an exponential fit). In each figure the mean value of the interspace distance $\langle\Delta\xi\rangle$ and its most probable value (max $\Delta\xi_i$) are provided.

is a strong indicator of a crossover occurring at a transition temperature $\tau_c \approx 10$, where the distribution becomes Gaussian [Fig. 6(d)].

Skewness. A more precise determination of the transition temperature can be achieved by examining the skewness γ_1 of the distributions $\rho(\Delta\xi_i)$ as a function of the temperature (Fig. 7). Skewness is a measure of the asymmetry of a probability distribution $\rho(x)$ and is defined as the third standardized moment:

$$\gamma_1 = \frac{\langle x - \langle x \rangle \rangle^3}{\sigma^3},$$

where σ is the standard deviation of $\rho(x)$. It is evident that in our case the skewness goes from negative to positive values as temperature increases (Fig. 7). Its absolute value possesses a minimum at a temperature $\tau_1 \approx 6$, which can be conceived as the critical one. At higher temperatures it saturates at the value 2, which is indeed the skewness of the exponential distribution.

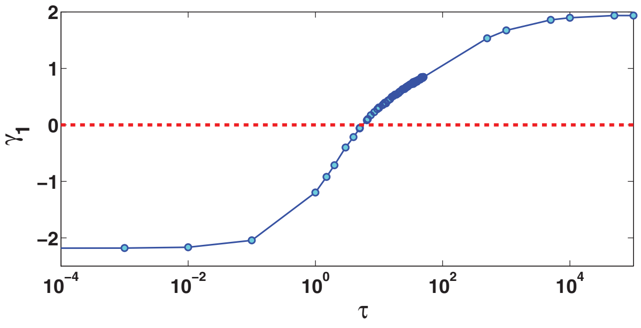

FIG. 7. (Color online) The skewness of the distributions $\rho(\Delta\xi_i)$ as a function of the temperature τ.

Cluster size and temperature. We have mentioned above that for temperatures $\tau > 10$ the particles tend to form clusters of various sizes. Let us now explore how the temperature affects the size of the clusters formed. In what follows we consider as cluster size 1 the size of a neighborhood which includes only one particle, i.e., the case when no cluster is formed. Furthermore, a particle i is assumed to belong to the same cluster as its previous neighbor $i - 1$ if they are separated by a distance smaller than a threshold d. The value of this threshold is taken to be the minimum interparticle distance $\Delta\xi_i$ of the mean configuration of particles at temperature τ. This choice helps in focusing on thermal fluctuations, thereby avoiding effects emerging from the specific structure of the crystal. Note that this quantity depends as well on the number of particles N. We observe (Fig. 8) that the probability of forming a larger cluster is generally increased with the increase of the temperature tending to a limiting form for ultra-high temperatures. This form coincides with the one obtained for randomly chosen configurations of particles confined in

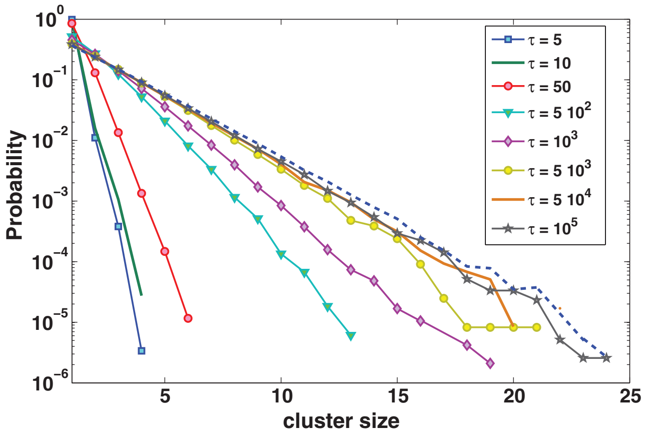

FIG. 8. (Color online) The probability distribution of cluster sizes for different temperatures (semilogarithmic scale): $\tau = 5$ (blue line with squares), $\tau = 10$ (green line), $\tau = 50$ (red line with circles), $\tau = 5 \times 10^2$ (cyan line with triangles), $\tau = 10^3$ (purple line with diamonds), $\tau = 5 \times 10^3$ (yellow line with circles), $\tau = 5 \times 10^4$ (brown line), $\tau = 10^5$ (black line with stars). The blue dashed line indicates the probability distribution of cluster sizes in the case of noninteracting particles confined in the box (purely random configurations).

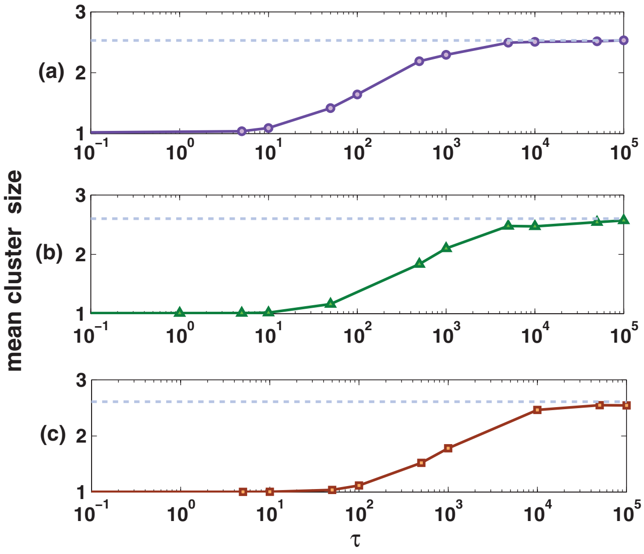

FIG. 9. (Color online) The mean cluster size as a function of the reduced temperature τ for systems with different numbers of particles: (a) $N = 50$, (b) $N = 100$, (c) $N = 200$. The horizontal dashed lines indicate the values of the mean cluster size for the respective numbers N of noninteracting particles confined in the box.

a box of length $L = 1$, i.e., for the noninteracting case. Therefore, for arbitrarily high temperatures the singularity of the Coulomb potential at small interparticle distances becomes irrelevant.

This behavior is also reflected in the dependence of the mean cluster size on the temperature, which is presented in Fig. 9 for the particle numbers $N = 50,100,$ and 200. The variation with the temperature is similar for the three cases being almost constant (one) for low temperatures, then increasing logarithmically, and finally saturating at a value close to 2.6, which is essentially the value of the mean cluster size of noninteracting particles confined in the box. For $N = 100$ the mean cluster size starts to increase around $\tau = 10$, which, as we have seen, is close to the transition temperature of the system. For $N = 50$ this temperature is slightly less (approximately $\tau = 4$), whereas for $N = 200$ it is around 30. Thus, we can make the crude statement that the transition temperature for this finite system increases (faster than linearly) with the number of particles.

Correlation functions. Concerning the correlation functions of the particles' positions

$$A(m) = \langle\langle \xi_{i+m}\xi_i \rangle\rangle - \langle\langle \xi_{i+m} \rangle\rangle \langle\langle \xi_i \rangle\rangle$$

(where $\langle\langle \ldots \rangle\rangle$ denotes the average both over the indices i and the ensemble of configurations), we encounter [Fig. 10(a)] a very slow decay with increasing distance m, taken as the magnitude of the difference of the particles' indices. The form of these functions is very close to a quadratic polynomial. A remarkable feature of the position correlation functions is that temperature does not affect them contrary to the typical case for most statistical systems (e.g., the spin correlation functions of the classical Ising model [37]). This, however, is in agreement with the fact that the mean configuration of the particles does not change much with the increase of temperature [Figs. 3(c) and 3(d)].

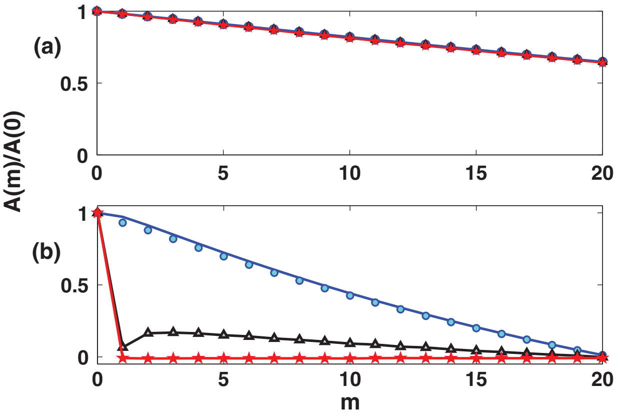

FIG. 10. (Color online) The normalized correlation functions $A(m)/A(0)$ for $\tau = 10^{-5}$ (blue line), $\tau = 10^{-1}$ (cyan circles), $\tau = 10$ (gray triangles with black line), $\tau = 10^{5}$ (red line with stars), and for two different quantities: (a) the absolute positions of the particles ξ_i, (b) the interspace distance $\Delta\xi_i$. Note that for (a) all the curves for different τ are on top of each other and therefore not distinguishable.

On the other hand, the correlation functions of the spacing between the particles

$$A(m) = \langle\langle \Delta\xi_{i+m}\Delta\xi_i \rangle\rangle - \langle\langle \Delta\xi_{i+m} \rangle\rangle \langle\langle \Delta\xi_i \rangle\rangle$$

exhibits a strong dependence on the temperature [Fig. 10(b)]. In particular, for low temperatures we observe a slower decay of the correlation function $A(m)$, whereas at high temperatures ($\tau \geqslant 10$) the decay is in general abrupt becoming practically zero for $m \geqslant 1$.

Energy dependence on N, T, L. The mean potential energy is in general a function of the temperature T, the length of the box L, and the number of particles N separately, i.e., $\langle E \rangle = f(T,L,N)$. In order to study numerically this dependence we need to deal with dimensionless quantities. We have already introduced the reduced temperature τ and the dimensionless positions $\{\xi_i\}$. The next step is to introduce the reduced specific mean energy $\langle \varepsilon \rangle \equiv \frac{L\langle E \rangle}{g^2 N}$, in analogy with the dimensionless reduced temperature τ, and to study the behavior of $\langle \varepsilon \rangle = h(\tau,N)$ keeping one of the parameters constant and varying the other. Note that the T, L dependence is reduced to a dependence on the single parameter τ, which exclusively determines the behavior of the system as discussed above. Following this procedure we have computed $\langle \varepsilon(\tau) \rangle$ for $N = 100$, using both the Metropolis and the Wang-Landau algorithm. Obviously [Fig. 11(a)] both algorithms give overall similar results, which can be interpreted as evidence for convergence. However, the Wang-Landau algorithm fails to describe the regime of ultra-high temperatures due to the predefined limited energy space available for the simulation. The reduced specific mean potential energy $\langle \varepsilon \rangle$ is almost constant for low τ, as the mean energy there is fully characterized by the minimum value of $\frac{V_C(\xi_1,\xi_2,\ldots,\xi_N)}{g^2}$ and increases almost linearly with the logarithm of the reduced temperature [$\langle \varepsilon \rangle \propto \log(\tau)$] for higher temperatures. Thus for low temperatures we obtain the familiar $\langle E \rangle \sim L^{-1}$ law for

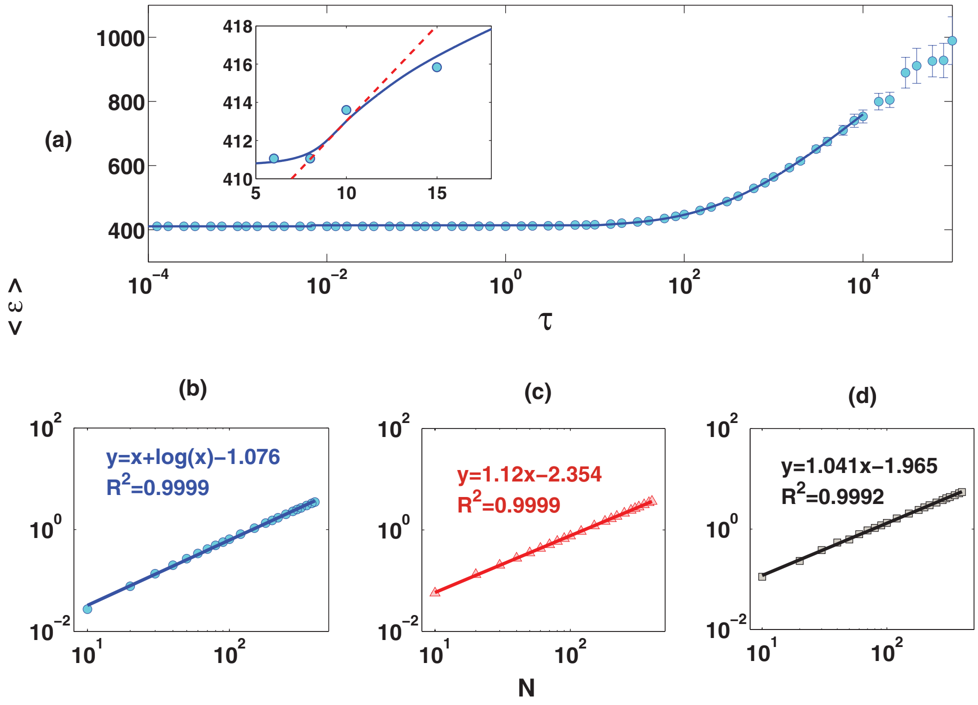

FIG. 11. (Color online) (a) The dependence of the dimensionless specific mean energy $\langle\varepsilon\rangle$ on the reduced temperature τ on a semilog scale for $N = 100$ (Metropolis: cyan circles; Wang-Landau: blue line). (b–d) The dependence of the dimensionless specific mean energy $\langle\varepsilon\rangle$ on N on a log-log scale for (b) $\tau = 10^{-2}$ (circles for numerical values, blue line fit), (c) $\tau = 10$ (triangles, red line linear fit), (d) $\tau = 10^5$ (squares, black line linear fit).

the Coulomb system. At temperatures close to $\tau_c \approx 10$ a weak change in the sign of the curvature can be observed [Fig. 11(a) (inset)], a fact that, as we will discuss below, leads to a smooth maximum in the heat capacity C_L. The dependence of $\langle E\rangle$ on τ (on both L and T) for higher temperatures can be interpreted as a consequence of the dependence of the transition temperature T_c on L, which is confirmed by the behaviour of C_L (see below).

We have used as well the Metropolis algorithm to obtain the dependence of $\langle\varepsilon\rangle$ on N for three reduced temperatures, characterized by a different qualitative behavior, corresponding to the low-, intermediate, and high-temperature regimes, respectively: $\tau = 10^{-2}$, 10, and 10^5. The diagrams of Figs. 11(c) and 11(d) show a linear relation on a log-log scale which indicates a power law relation between the involved quantities. The results of the linear fits lead us to the following conclusions. For Fig. 11(b) (low-temperature region) the fit contains not only a linear but also a logarithmic term, indicating a relationship $\langle\varepsilon\rangle \propto N\log(N)$. This logarithmic correction is expected for 1D Coulomb systems in this temperature regime [23], due to the formation of a crystal and the fixed particle positions. For larger temperatures the relation becomes linear, resulting in a characteristic exponent around 1.12 for $\tau = 10$ and 1.04 for $\tau = 10^5$, thus approaching 1 for high temperatures ($\langle\varepsilon\rangle \propto N$). It is clear that since the reduced mean specific energy $\langle\varepsilon\rangle$ depends on N extensivity is violated, a fact that is expected for systems with long-range interactions. In summary, the mean Coulomb energy scales roughly as $\langle E\rangle \propto \frac{N^2}{L}$, which coincides with our intuition for Coulomb systems, but looking more precisely at $T \to 0$ the scaling of the mean potential energy takes the form [Fig. 11(b)]:

$$\langle E\rangle \propto \frac{N^2\log(N)}{L}, \tag{3}$$

which will be used below in an attempt of interpreting the thermodynamic limit in such a system.

Specific heat capacity c_L. In order to proceed in our study of the temperature dependence of $\langle\varepsilon\rangle$ we have also calculated the specific heat capacity $c_L \equiv \frac{1}{N}(\frac{\partial\langle\varepsilon\rangle}{\partial\tau})_L$ of the Coulomb gas confined in a 1D box. Due to the fact that numerical differentiation usually encounters large errors, it is difficult to extract the heat capacity's values from the results of the Metropolis algorithm as shown in Fig. 11(a). A calculation of the heat capacity via the energy fluctuations

$$\frac{c_L}{k_B} = \frac{1}{N}\Lambda^2(\langle\varepsilon^2\rangle - \langle\varepsilon\rangle^2) \tag{4}$$

proved also to be insufficient with the use of the Metropolis' results, especially in the low-temperature regime. The main problem was again the large errors involved in the calculation of the energy's variance. When calculated with the jackknife method [37], they were found to have a value up to 70%, a fact that renders the results useless. Thus, we have used instead the density of states $g(\varepsilon)$ obtained from the Wang-Landau algorithm, in order to compute the quantities $\langle\varepsilon\rangle,\langle\varepsilon^2\rangle$ and finally the reduced specific heat capacity via the relation (4). We present our results for $N = 100$ in Fig. 12 using a semilogarithmic scale. A smooth maximum occurs which is located at $\tau \approx 11$, thus within the temperature region in

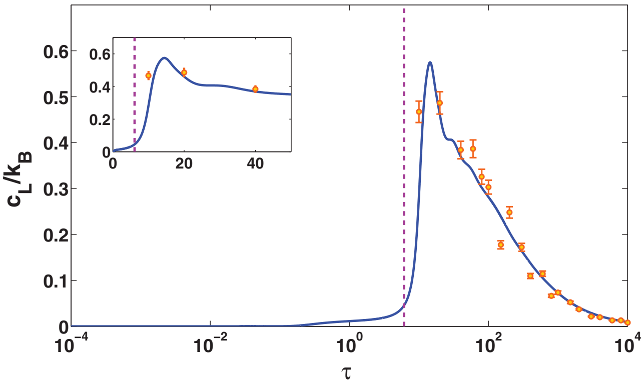

FIG. 12. (Color online) The temperature dependence of the specific heat capacity $\frac{c_L}{k_B}$ for $N = 100$ on a semilogarithmic scale: (blue line) Wang-Landau results, (orange circles) Metropolis results. The dashed purple line indicates the temperature τ_1 at which the skewness becomes zero.

which the histogram of the interparticle distance $\Delta\xi_i$ takes approximately a Gaussian form [Fig. 6(d)] at the transition point from the crystalline to cluster phase. The temperature τ_1 at which the skewness of the distributions becomes zero (dashed purple line) coincides with the temperature at which the caloric curve starts to increase significantly. The results of Metropolis for high temperatures are found to be in accordance with the Wang-Landau results. The complete behavior of c_L reinforces the evidence that in this temperature region around 10 there is a crossover, whose transition temperature T_c decreases as L^{-1} since for fixed $N = 100$ we obtain $\tau_c \approx 10 \Rightarrow T_c \approx \frac{10g^2}{k_B L}$.

The thermodynamic limit. As depicted in the dependence of the mean potential energy $\langle E\rangle$ on N, L [Eq. (3)] the system of ions confined in a 1D box presents strong deviations from extensivity. The statistical treatment of nonextensive systems is a challenging task, and many of its aspects remain still open questions. A detailed study of the handling of nonextensivity in order to obtain thermodynamic quantities and parameters that remain finite in the thermodynamic limit can be found in Ref. [38]. Although this procedure is beyond the scope of the present paper, which aims only at the description of finite systems, we present some basic results obtained with the methods discussed in Ref. [38].

The main idea is to normalize the thermodynamic quantities except the entropy S with the excessive powers of N, a fact that is justified in the context of finite systems and resembles the procedure we have followed to define dimensionless quantities independent of the system's size, like the reduced temperature. Assuming a uniform distribution of charges with $\rho = g^2 \frac{N}{L}$, the mean potential energy per particle scales roughly as

$$\frac{\langle E\rangle}{N} = \rho \int_1^N r^{-1}\, dr = \rho \log(N) = g^2 \frac{N \log(N)}{L}.$$

Note that this expression is the same as the one we have obtained for the low-temperature regime [Eq. (3)]. The excessive dependence N^* in N is then given by $N^* = N \log(N)$, and one can define a normalized energy $\langle E^*\rangle \equiv \frac{\langle E\rangle}{N^*}$, which is a pseudo-extensive quantity [38]. This is used in order to obtain the thermodynamic limit in the following way:

$$\lim_{N\to\infty} \frac{F(T,N)}{NN^*} = \lim_{N\to\infty} \frac{\langle E(T,N)\rangle}{NN^*} - \lim_{N\to\infty} \frac{T}{N^*}\frac{S(T,N)}{N}. \tag{5}$$

In order to keep entropy an extensive quantity we need to define a pseudo-intensive temperature $T^* \equiv \frac{T}{N^*}$, which leads to a normalized reduced temperature:

$$\tau^* \equiv \frac{\tau}{N^*} = \frac{\tau}{N \log(N)}. \tag{6}$$

This quantity is dimensionless and independent of the size (N, L) of the system; thus its use helps to interpret our results in the thermodynamic limit. The critical temperature of our system is then found to be

$$\tau_c^* = \frac{\tau_c}{N^*} \approx 0.022. \tag{7}$$

Since $\tau_c = 0.022N \log(N)$ we conclude that indeed τ_c increases with the number of particles N faster than linearly. What is more, for $N = 50$ we are led to a value $\tau_c \approx 4.2$, whereas for $N = 200$ the critical value is $\tau_c \approx 23$. These values are very close to the crude results obtained above from the study of the mean cluster size as a function of temperature (Fig. 9).

IV. THE INFLUENCE OF THE TRAPPING POTENTIAL

We have studied the statistical properties of a 1D chain of ions confined in a box. Let us now briefly investigate the effect of the trapping potential on these properties. We focus especially on the case of the harmonic trap since it is the most frequently used and convenient trapping potential. In the low-temperature regime 1D systems of ions under harmonic confinement have been extensively studied [23–28]. It has been found that a crystal is obtained whose length depends nontrivially on the number of particles. The crystalline structure represents a nonuniform ion distribution with the opposite behavior of the one encountered for the box trap (Fig. 5) since the ions tend to accumulate in the inner region rather than the edges. This leads to a discrete but positively skewed distribution of interparticle distances $\rho(\Delta\xi_i)$ even for ultra-low temperatures [Fig. 13(a)]. For temperatures until $T \approx 1$ the skewness γ_1 is almost constant. Then it starts to increase up to $T \approx 10^2$, and from then on it saturates at a value close to 7. No minimum or zero value exists. Although the distribution $\rho(\Delta\xi_i)$ still undergoes a transition from a discrete form to a continuous one with a maximum at $\Delta\xi_i$ approaching zero, it is not possible to identify a clear transition temperature by requiring this distribution to become symmetric. A clustering (most probable value: $\Delta\xi_i \to 0$) is observed for higher temperatures in the harmonic trap, but the form of the distribution does not tend to an exponential, but to one with a much longer tail as indicated by the very large value of the skewness. In general the deviation of the statistical behavior of the ions under harmonic confinement from the observed one for the box trap can to a large extent be attributed to the change of the chain's length with temperature [Fig. 13(b)]. In the low-temperature regime the length of the

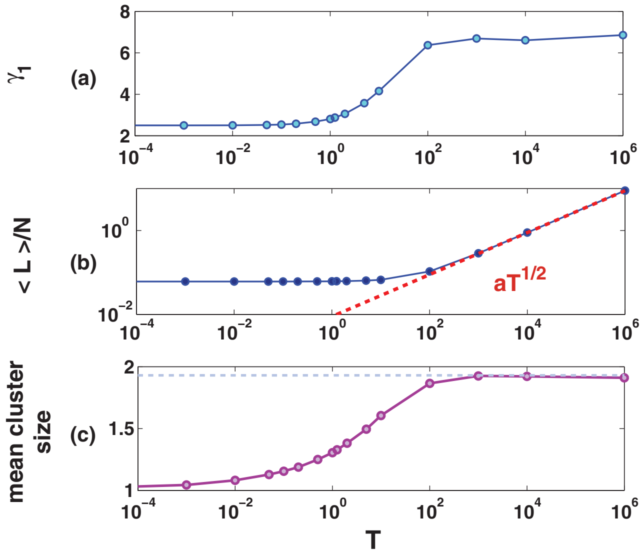

FIG. 13. (Color online) Statistical properties of a system of $N = 100$ ions confined in a harmonic trap with $m\omega^2 = 32$: (a) The skewness of the distributions $\rho(\Delta x_i)$ as a function of the temperature $k_B T$. (b) The temperature dependence of the chain's mean length $\langle L \rangle$. (c) The mean cluster size as a function of the temperature $k_B T$. The horizontal dashed line indicates the value of the mean cluster size for N noninteracting particles confined in the same harmonic trap.

chain is approximately constant with a value given by [23]

$$L_0(N) \approx 2\left[3N\log(N)\frac{g^2}{m\omega^2}\right]^{1/3}. \tag{8}$$

In our case this yields $L \approx 7$. For temperatures larger than $T \approx 10^2$ we encounter the behavior $\langle L\rangle \propto T^{1/2}$, which is clearly what would be obtained for noninteracting particles under harmonic confinement in one dimension. Thus for very large temperatures all the properties are dominated essentially by the trapping potential.

Concerning the formation of the clusters, sizes larger than one are possible even for comparatively low temperatures [Fig. 13(c)]. The mean cluster size increases with temperature and saturates finally at $T \approx 10^2$ at a value smaller than the respective one for the box (Fig. 9). In this case too, the saturation value coincides with the value of the mean cluster size obtained for an identical system in the absence of interactions, and it thus constitutes a feature completely determined by the size of the system and the trapping potential. A definition of a reduced temperature is not feasible since the Hamiltonian contains parts with different spatial dependencies. However, it is possible to use the relation obtained for the box $\tau^* = k_B T \frac{L}{N\log(N)}$ and substitute the length L of the box with the minimum length of the chain $L_0(N)$ [Eq. (8)]. We find then a critical temperature $k_B T_c \approx 1.4$. Close to this value the skewness and the mean length start to rise whereas the mean cluster size reaches half of its maximum value. Therefore, this could be interpreted as a critical temperature for the system of ions under harmonic trapping.

To conclude, the transition from a crystalline to a cluster phase holds independently of the trapping potential. All the statistical properties seem to be affected by temperature, in a way similar to the case of the box trap and thus using the appropriate length scale, the expression obtained for the critical temperature [Eq. (7)] provides us with valid results for different trapping potentials. However, the specific forms of the distributions $\rho(\xi_i), \rho(\Delta\xi_i)$ are affected by the change of the trapping, since the minimum configuration of the total potential $V = V_C + V_{\text{trap}}$, i.e., the shape of the crystal, is qualitatively different for each case. Furthermore, for high temperatures these distributions are predominantly characterized by the trapping potential, tending to the forms that would be obtained in the case of noninteracting particles confined in the same traps.

V. CONCLUSIONS

We have explored the statistical and thermodynamical properties of a system of equally charged particles confined in a box of length L. This finite system exhibits a crossover from a crystalline to a cluster phase at a transition temperature T_c, which depends on both the number of particles N and the length L of the box, as $T_c \propto \frac{N\log(N)}{L}$. This expression comes from an interpretation of the thermodynamic limit for nonextensive systems, where a normalized temperature τ^* is introduced scaling with the system's size in the same way as the mean potential energy per particle. The thermodynamic behavior of the finite system is properly described by the characteristic distributions and correlations of the scaled relative distances $\Delta\xi_i$ of the particles, whereas quantities based on the absolute positions of the particles are barely affected by the temperature. Concretely, the probability density of $\Delta\xi_i$ undergoes a marked transition from a discrete accumulative to an exponential form as the temperature increases. In the transition regime it acquires a symmetric form, and the corresponding heat capacity shows a maximum. For high temperatures the particles form clusters whose size grows with temperature and finally saturates. When the trapping conditions are altered a similar transition occurs, but the critical temperature is not clearly identifiable through the forms of the distributions as described above.

In order to relate the results of our simulations to concrete physical setups we need to assign specific values to the parameters. Thus, for example, the temperature measured in SI units (T^{SI}) is related to the normalized temperature τ^* through

$$T^{\text{SI}} = \frac{g^2 N\log(N)\tau^*}{k_B L} = \frac{Z^2e^2N\log(N)\tau^*}{4\pi\varepsilon_0 k_B L}$$
$$\approx 1.7\times10^{-5}Z^2\tau^*\frac{N\log(N)}{L}Km,$$

where Z is the charge of the ions. We find then from Eq. (7) that $T_c^{\text{SI}} = 3.7\times10^{-7}Z^2\frac{N\log(N)}{L}$ Km. For cold atomic ions, the formation of quasi-1D crystals with $L \approx 1$ mm [39], $N \approx 100$ ions, and, e.g., $Z = 1$ leads to a critical temperature $T_c^{\text{SI}} \approx 1.7\times10^{-1}$ K, which is easily accessible experimentally. Therefore, by tuning the values of L and N it is possible to study this crystalline-clustering crossover in laboratory experiments with cold ions assuming a 1D trapping geometry.

Let us now speculate about potential applications of our detected crossover and related phases to high energy collisional experiments of, e.g., highly charged nuclei. Although the geometry of the highly energetic colliding ions is quasi-2D, it is interesting to estimate some properties assuming roughly that the 1D picture explored here is not a misleading description. In nuclear systems the length scales are of order $L \approx 10^{-15}$ m which for $N = 100$ nucleons leads to $T_c^{\mathrm{SI}} \approx 10^{11}$ K, i.e., to a relative energy $E_c \approx 10$ MeV. The nuclear mean binding energy is of the order of 8 MeV per nucleon resulting in a total energy of 800 MeV for the nucleus, somewhat larger than E_c. Thus the nucleons confined in the colliding nuclei could be in the cluster phase. Finally, we remark that the crossover physics analyzed in this work could also appear in 1D systems showing other long-range interactions, such as dipolar chains [40].

ACKNOWLEDGMENTS

We thank B. Liebchen for stimulating discussions. A.Z. thanks the International Max Planck Research School for Ultrafast Imaging and Structural Dynamics for a PhD scholarship.

APPENDIX: UNIQUENESS OF THE POTENTIAL MINIMUM OF A FINITE 1D COULOMB CHAIN

Here we present a proof that the global minimum energy configuration is the only minimum that the potential of the finite 1D ion chain can acquire. We want only permutationally different configurations, so we assume that we have $N+2$ particles that are ordered in the sense that $\xi_0 < \xi_1 < \cdots < \xi_N < \xi_{N+1}$ (ξ_0 is the position of the first particle and ξ_{N+1} the position of the last one). We have shown (Sec. III A) that in order to obtain a minimum the first particle has to be fixed at the left edge of the segment, i.e., $\xi_0 = 0$, whereas the last particle should always occupy its right edge $\xi_{N+1} = 1$ (the length of box is $L = 1$). Thus, the potential is given by the expression

$$V = \sum_{i=0}^{N+1}\sum_{j=0}^{i-1}\frac{1}{\xi_i - \xi_j} = \sum_{i=1}^{N}\sum_{j=1}^{i-1}\frac{1}{\xi_i - \xi_j} + \sum_{i=1}^{N}\left(\frac{1}{\xi_i} + \frac{1}{1-\xi_i}\right).$$

Differentiating this expression with respect to ξ_k we obtain

$$\frac{\partial V}{\partial \xi_k} = -\sum_{i=1}^{k-1}\frac{1}{(\xi_k - \xi_i)^2} + \sum_{i=k+1}^{N}\frac{1}{(\xi_i - \xi_k)^2} - \frac{1}{\xi_k^2} + \frac{1}{(1-\xi_k)^2}.$$

A second differentiation with respect to ξ_l leads to

$$\frac{\partial^2 V}{\partial \xi_l \partial \xi_k} = \sum_{i=1}^{k-1}\frac{2}{(\xi_k - \xi_i)^3}\delta_{kl} - \sum_{i=1}^{k-1}\frac{2}{(\xi_k - \xi_i)^3}\delta_{il} - \sum_{i=k+1}^{N}\frac{2}{(\xi_i - \xi_k)^3}\delta_{il} + \sum_{i=k+1}^{N}\frac{2}{(\xi_i - \xi_k)^3}\delta_{kl} + \left[\frac{2}{\xi_k^3} + \frac{2}{(1-\xi_k)^3}\right]\delta_{kl}.$$

Therefore, we obtain for the Hessian matrix H of our potential V ($H_{ij} \equiv \frac{\partial^2 V}{\partial \xi_i \partial \xi_j}$)

$$H_{kk} = \frac{\partial^2 V}{\partial \xi_k \partial \xi_k} = \frac{2}{\xi_k^3} + \frac{2}{(1-\xi_k)^3} + 2\sum_{i \neq k}\frac{1}{|\xi_i - \xi_k|^3} > 0,$$

whereas the of-diagonal elements ($l \neq k$) are given by

$$H_{lk} = \frac{\partial^2 V}{\partial \xi_l \partial \xi_k} = -\frac{2}{|\xi_k - \xi_l|^3} < 0.$$

It is known from multivariate calculus that if for arbitrary $d\vec{\xi}, \vec{\xi}$ it holds that

$$d^2 V = 2\sum_{i=1}^{N}\sum_{j=1}^{N} H_{ij}(\vec{\xi})d\xi_i d\xi_j > 0,$$

then the function V is strictly convex and it possesses at most one minimum. In our case,

$$\begin{aligned} d^2 V &= \sum_{k=1}^{N} H_{kk} d^2\xi_k + \sum_{k=1}^{N}\sum_{\substack{l=1\\ l\neq k}}^{N} H_{lk} d\xi_k d\xi_l \\ &= 2\sum_{k=1}^{N}\left[\frac{1}{\xi_k^3} + \frac{1}{(1-\xi_k)^3}\right] d^2\xi_k \\ &\quad + \sum_{k=1}^{N}\sum_{\substack{l=1\\ l\neq k}}^{N}\frac{1}{|\xi_k - \xi_l|^3}(d\xi_k - d\xi_l)^2. \end{aligned}$$

It is obvious that $\sum_{k=1}^{N}\sum_{\substack{l=1\\ l\neq k}}^{N}\frac{1}{|\xi_k-\xi_l|^3}(d\xi_k - d\xi_l)^2 \geqslant 0$ and $\sum_{k=1}^{N}[\frac{1}{\xi_k^3} + \frac{1}{(1-\xi_k)^3}]d^2\xi_k > 0$ for $d\vec{\xi} \neq 0$, so the quantity d^2V is always positive and the potential a convex function with only one minimum.

In general if a trapping potential of the form $V_{\mathrm{trap}} = A\sum_{k=1}\xi_k^n$, with $A > 0$ and an even number $n \geqslant 2$ is chosen, it is evident from the above procedure that for the total potential $V = V_C + V_{\mathrm{trap}}$ it holds:

$$d^2 V = n(n-1)A\sum_{k=1}^{N}\xi_k^{n-2}d^2\xi_k + \sum_{k=1}^{N}\sum_{\substack{l=1\\ l\neq k}}^{N}\frac{1}{|\xi_k - \xi_l|^3}(d\xi_k - d\xi_l)^2,$$

which is also positive definite, and thus the total potential possesses again a single minimum.

[1] R. C. Thompson, Adv. At. Mol. Opt. Phys. **66**, 63 (1993).

[2] N. Hermanspahn, H. Häffner, H.-J. Kluge, W. Quint, S. Stahl, J. Verdú, and G. Werth, Phys. Rev. Lett. **84**, 427 (2000).

[3] M. Johanning, A. Braun, N. Timoney, V. Elman, W. Neuhauser, and C. Wunderlich, Phys. Rev. Lett. **102**, 073004 (2009).

[4] R. Blatt and C. F. Roos, Nat. Phys. **8**, 277 (2012).

[5] J. I. Cirac and P. Zoller, Phys. Rev. Lett. **74**, 4091 (1995).

[6] F. Schmidt-Kaler *et al.*, Nature (London) **422**, 408 (2003).

[7] K. H. Kingdon, Phys. Rev. **21**, 4008 (1923).

[8] F. M. Penning, Physica **3**, 873 (1936).

[9] W. Paul, Rev. Mod. Phys. **62**, 531 (1990).

[10] N. Yu, W. Nagourney, and H. Dehmelt, J. Appl. Phys. **69**, 3779 (1991).

[11] R. Blümel, Phys. Rev. A **51**, 30(R) (1995).

[12] W. Neuhauser, M. Hohenstatt, P. E. Toschek, and H. Dehmelt, Phys. Rev. A **22**, 1137 (1980).

[13] M. Drewsen, C. Brodersen, L. Hornekaer, J. S. Hangst, and J. P. Schiffer, Phys. Rev. Lett. **81**, 2878 (1998).

[14] N. Kjærgaard, K. Mølhave, and M. Drewsen, Phys. Rev. E **66**, 015401 (2002).

[15] N. Kjærgaard and M. Drewsen, Phys. Rev. Lett. **91**, 095002 (2003).

[16] F. Diedrich, E. Peik, J. M. Chen, W. Quint, and H. Walther, Phys. Rev. Lett. **59**, 2931 (1987).

[17] R. Blümel, J. M. Chen, E. Peik, W. Quint, W. Schleich, and H. Walther, Nature (London) **334**, 309 (1988).

[18] R. W. Hasse and V. V. Avilov, Phys. Rev. A **44**, 4506 (1991).

[19] H. Totsuji, T. Kishimoto, C. Totsuji, and K. Tsuruta, Phys. Rev. Lett. **88**, 125002 (2002).

[20] S. Ichimaru *et al.*, Rev. Mod. Phys. **54**, 4 (1982).

[21] R. W. Hasse and J. P. Schiffer, Ann. Phys. **203**, 419 (1990).

[22] V. M. Bedanov and F. M. Peeters, Phys. Rev. B **49**, 2667 (1994).

[23] D. H. E. Dubin, Phys. Rev. E **55**, 4017 (1997).

[24] J. P. Schiffer, J. Phys. B **36**, 511 (2003).

[25] G. Morigi and S. Fishman, Phys. Rev. Lett. **93**, 170602 (2004).

[26] G. Morigi and S. Fishman, Phys. Rev. E **70**, 066141 (2004).

[27] S. Fishman, G. DeChiara, T. Calarco, and G. Morigi, Phys. Rev. B **77**, 064111 (2008).

[28] Z.-X. Gong, G.-D. Lin, and L.-M. Duan, Phys. Rev. Lett. **105**, 265703 (2010).

[29] N. Metropolis *et al.*, J. Chem. Phys. **21**, 1087 (1953).

[30] F. Wang and D. P. Landau, Phys. Rev. Lett. **86**, 2050 (2001).

[31] M. S. Shell, P. G. Debenedetti, and A. Z. Panagiotopoulos, Phys. Rev. E **66**, 056703 (2002).

[32] J. J. de Pablo, Q. Yan, and R. Faller, J. Chem. Phys. **116**, 8649 (2002).

[33] P. Poulain, F. Calvo, R. Antoine, M. Broyer, and P. Dugourd, Phys. Rev. E **73**, 056704 (2006).

[34] A. Tröster and C. Dellago, Phys. Rev. E **71**, 066705 (2005).

[35] F. Calvo and E. Yurtsever, Eur. Phys. J. D **44**, 81 (2007).

[36] B. S. Everitt, *The Cambridge Dictionary of Statistics* (Cambridge University Press, Cambridge, 2002).

[37] M. E. J. Newman and G. T. Barkema, *Monte Carlo Methods in Statistical Physics* (Oxford University Press, New York, 1999).

[38] C. Tsallis, *Introduction to Nonextensive Statistical Mechanics: Approaching a Complex World* (Springer, New York, 2009).

[39] A. Dantan, M. Albert, J. P. Marler, P. F. Herskind, and M. Drewsen, Phys. Rev. A **80**, 041802(R) (2009).

[40] J. R. Armstrong *et al.*, arXiv:1112.6141v2 [cond-mat.quant-gas].

2.2 Charges on helical manifolds

2.2.1 Two-body scattering of charges on an inhomogeneous helix

PHYSICAL REVIEW E **88**, 043202 (2013)

Classical scattering of charged particles confined on an inhomogeneous helix

A. V. Zampetaki,[1] J. Stockhofe,[1] S. Krönke,[1] and P. Schmelcher[1,2]
[1]*Zentrum für Optische Quantentechnologien, Universität Hamburg, Luruper Chaussee 149, 22761 Hamburg, Germany*
[2]*The Hamburg Centre for Ultrafast Imaging, Luruper Chaussee 149, 22761 Hamburg, Germany*

(Received 27 August 2013; published 3 October 2013)

We explore the effects arising due to the coupling of the center of mass and relative motion of two charged particles confined on an inhomogeneous helix with a locally modified radius. It is first proven that a separation of the center of mass and the relative motion is provided if and only if the confining manifold represents a homogeneous helix. In this case, bound states of repulsively Coulomb interacting particles occur. For an inhomogeneous helix, the coupling of the center of mass and relative motion induces an energy transfer between the collective and relative motion, leading to dissociation of initially bound states in a scattering process. Due to the time reversal symmetry, a binding of the particles out of the scattering continuum is thus equally possible. We identify the regimes of dissociation for different initial conditions and provide an analysis of the underlying phase space via Poincaré surfaces of section. Bound states inside the inhomogeneity as well as resonant states are identified.

DOI: 10.1103/PhysRevE.88.043202 PACS number(s): 41.20.−q, 37.10.Ty, 37.90.+j, 05.45.−a

I. INTRODUCTION

The formation of helical patterns and structures is common in many natural systems ranging from DNA molecules and amino acids to non-neutral plasmas trapped in magnetic fields [1] and self-assembled configurations of charged particles confined in nanotubes [2]. Studying the motion of particles confined in a helix has proven to be a useful tool for the understanding of complex phenomena such as the optical activity of sugar solutions [3,4]. Certainly, the problem of the confined motion of particles in a helical manifold is of fundamental interest since it reveals many intriguing phenomena. Quantum particles confined in one dimension (1D) preserve some information of the surrounding three-dimensional (3D) space and thus experience an effective geometric potential which depends on the curvature of the confining manifold [5]. Such geometric potential effects lead to the formation of bound states in helical waveguides with a locally modified radius [6] or in twisting tubes [7]. In the presence of an electric field, superlattice properties can emerge for a confined charge carrier [8], whereas when the particles interact with dipolar forces a peculiar quantum phase transition from liquid to gas has been predicted [9].

In spite of their physical interest, helical traps have only recently been investigated experimentally. In nanotechnology, curved nanotubes such as rolls, spirals, and helices from thin solid films of silicon germanium can be constructed [10,11]. Helical traps can also be realized experimentally for cold atoms either via the interference of counterpropagating Laguerre-Gaussian beams [12–14] or via the evanescent field of a nanofiber [15–17] which creates a double-helix trapping potential. Such setups allow the creation of a homogeneous helical potential over the entire length of the nanofiber as well as local modifications of the radius and the pitch of the helix through local variations of the diameter of the nanofiber [17]. Beyond these, a plethora of trapping techniques also exist for (ultra)cold ions [18,19].

Motivated by the above, it is instructive to explore the classical behavior of ions or generally charged particles in a helical geometry. Surprisingly, this problem has not been studied extensively in the literature. In Ref. [20] it has been shown that the classical dynamics of a system of identical charged particles confined in a helical manifold presents very intriguing phenomena when the particles interact via long-range interactions such as the Coulomb interaction. In particular, the interplay between the 1D confined motion of the particles and their interactions via the full 3D space gives rise to an effective oscillatory force. This fact yields, in turn, stable equilibrium configurations despite the repulsive interactions between the particles and induces classical bound states whose number can be tuned by varying the parameters of the helix.

Following the direction of the above study, we explore in this work the two-body scattering dynamics off an inhomogeneity in a helical trap. As a first step, we rigorously prove that a separation of the center of mass (c.m.) and the relative motion is provided for an interaction potential which depends exclusively on the Euclidean distance between the particles $V(|\mathbf{r}_1 - \mathbf{r}_2|)$, if and only if the confining curve is a homogeneous helix. Then, we examine the case of an inhomogeneous helical trap with a locally modified radius, and explore effects due to the coupling of the c.m. and relative motion. It is shown that initially bound states can finally dissociate due to the modulation of the potential which leads to an energy transfer between the c.m. and the relative degrees of freedom. Due to time reversal symmetry, it is thus equally possible for two unbound charged particles to form a bond due to the local inhomogeneity. A phase space analysis provides us with bound states within the inhomogeneous region as well as with resonant states and completes the picture of the two-particle dynamics.

The paper is organized as follows. In Sec. II, we present the general Lagrangian for the problem of two interacting classical charged particles confined on a curve and we investigate the properties that the confining curve has to fulfill so that a separation of the c.m. and the relative degrees of freedom is provided. In Sec. III, we present our model of two charged particles confined to an inhomogeneous helix. Section IV contains our results for the scattering, whereas Sec. V provides our analysis of the respective phase space. Finally, Sec. VI represents a brief summary of our findings.

II. INTERACTING PARTICLES CONFINED TO A CURVED 1D MANIFOLD

We consider a system of two particles with masses m_1,m_2 interacting via a potential $V(|\mathbf{r}_1 - \mathbf{r}_2|)$ that depends only on the Euclidean distance between them. Their Lagrangian is given by

$$L(\{\mathbf{r}_i,\dot{\mathbf{r}}_i\}) = \frac{1}{2}\sum_{i=1}^{2} m_i \dot{\mathbf{r}}_i^2 - V(|\mathbf{r}_1 - \mathbf{r}_2|).$$

If the particles are confined onto a smooth, regular, and either closed or infinitely extended space curve $\mathbf{r} : \mathbb{R} \mapsto \mathbb{R}^3$ parametrized with the arbitrary parameter u, i.e., $\mathbf{r}_i = \mathbf{r}(u_i)$, the Lagrangian takes the form

$$L(\{u_i,\dot{u}_i\}) = \frac{1}{2}\sum_{i=1}^{2} m_i \left|\partial_{u_i}\mathbf{r}(u_i)\right|^2 \dot{u}_i^2 - V[|\mathbf{r}(u_1) - \mathbf{r}(u_2)|]. \tag{1}$$

If we choose the arc length parametrization [21]

$$s : u \mapsto s(u) = \int_0^u |\partial_{u'}\mathbf{r}(u')|du', \tag{2}$$

since the tangent vector $\mathbf{t}(s_i) = \partial_{s_i}\mathbf{r}(s_i)$ is a unit vector we arrive at the expression

$$L(\{s_i,\dot{s}_i\}) = \frac{1}{2}\sum_{i=1}^{2} m_i \dot{s}_i^2 - V[|\mathbf{r}(s_1) - \mathbf{r}(s_2)|]. \tag{3}$$

We thus observe that the kinetic energy term retains the Cartesian form in the arc length parametrization, leading to the familiar expressions for the conjugate momenta and the Euler-Lagrange (EL) equations of motion. Introducing the c.m. $S = (m_1 s_1 + m_2 s_2)/(m_1 + m_2)$ and the relative coordinate $s = s_1 - s_2$, as well as the total mass $M = m_1 + m_2$ and the reduced mass $\mu = \frac{m_1 m_2}{M}$, we are led to

$$L(\{s,S,\dot{s},\dot{S}\}) = \tfrac{1}{2}M\dot{S}^2 + \tfrac{1}{2}\mu\dot{s}^2 - \tilde{V}(S,s), \tag{4}$$

where

$$\tilde{V}(S,s) = V\left[\left|\mathbf{r}\left(S + \frac{m_2}{M}s\right) - \mathbf{r}\left(S - \frac{m_1}{M}s\right)\right|\right]. \tag{5}$$

This yields the following EL equations:

$$M\ddot{S} = -\frac{\partial\tilde{V}}{\partial S}, \quad \mu\ddot{s} = -\frac{\partial\tilde{V}}{\partial s}. \tag{6}$$

Evidently, a separation of the c.m. from the relative motion is provided if and only if $\frac{\partial\tilde{V}}{\partial S}$ is exclusively a function of S which is equivalent to

$$\frac{\partial^2\tilde{V}}{\partial s\,\partial S} = 0 \Leftrightarrow \tilde{V}(S,s) = V_1(S) + V_2(s) \tag{7}$$

with V_1, V_2 being arbitrary functions of S and s, respectively.

In order to analyze this condition further, we technically have to distinguish the two cases of a regular and a singular potential $\tilde{V}(S,s)$ at $s = 0$. For a regular potential, we obtain from (5) that $\tilde{V}(S,0) = V(0)$. Condition (7) then yields

$$V_1(S) = V(0) - V_2(0) = \text{const} \Rightarrow \frac{\partial V_1}{\partial S} = \frac{\partial\tilde{V}}{\partial S} = 0.$$

For a potential with a singularity at $s = 0$, as in the typical case of Coulomb interaction, choosing an infinitesimal value $\varepsilon > 0$ for the s coordinate, we are led through (5) to

$$\begin{aligned}\tilde{V}(S,\varepsilon) &= V\left[\left|\mathbf{r}\left(S + \frac{m_2}{M}\varepsilon\right) - \mathbf{r}\left(S - \frac{m_1}{M}\varepsilon\right)\right|\right]\\ &= V\left[\left|\mathbf{r}(S) + \frac{m_2}{M}\varepsilon\mathbf{t}(S) - \mathbf{r}(S) + \frac{m_1}{M}\varepsilon\mathbf{t}(S)\right|\right]\\ &= V[|\varepsilon\mathbf{t}(S)|] = V(\varepsilon)\end{aligned} \tag{8}$$

since $|\mathbf{t}(S)| = 1$. Thus, for arbitrary $S,\tilde{S}$

$$\tilde{V}(S,\varepsilon) = \tilde{V}(\tilde{S},\varepsilon) = V(\varepsilon)$$

and Eq. (7) for $s = \varepsilon$ leads to

$$V_1(S) = V_1(\tilde{S}) = V(\varepsilon) - V_2(\varepsilon)\,\forall S,\tilde{S} \in \mathbb{R} \Rightarrow \frac{\partial V_1}{\partial S} = \frac{\partial\tilde{V}}{\partial S} = 0.$$

Therefore, both cases lead to the condition $\frac{\partial\tilde{V}}{\partial S} = 0$ and we conclude that the c.m. and relative motion mutually separate for a potential that depends only on the interparticle Euclidean distance [Eq. (5)] if and only if $\frac{\partial\tilde{V}}{\partial S} = 0$. Furthermore, this is a necessary and sufficient condition for the conservation of the total momentum

$$P = \frac{\partial L}{\partial\dot{S}} = M\dot{S}$$

as follows from (4) and the EL equations (6), yielding a free particle motion for the c.m.

Introducing the function $R(s_1,s_2) = |\mathbf{r}(s_1) - \mathbf{r}(s_2)|$, with $s_1 = S + \frac{m_2}{M}s$, $s_2 = S - \frac{m_1}{M}s$, and $V'(R) = \frac{dV}{dR}\big|_{R=R(s_1,s_2)}$, we obtain

$$\frac{\partial\tilde{V}}{\partial S} = V'(R)\frac{\partial R}{\partial S} = V'(R)\big[\partial_{s_1}R(s_1,s_2) + \partial_{s_2}R(s_1,s_2)\big] \tag{9}$$

and we are thus led to the conclusion that a conservation of the total momentum as well as a separation of the c.m. from the relative coordinate is provided for interacting particles if and only if

$$\frac{\partial R}{\partial S} = \partial_{s_1}R(s_1,s_2) + \partial_{s_2}R(s_1,s_2) = 0, \quad \forall\, s_1,s_2 \in \mathbb{R}. \tag{10}$$

The results of [20] indicate that for the confining manifold being a homogeneous helix, i.e., a helix with a constant radius and pitch, the c.m. motion is separated from the relative one. In fact, the homogeneous helix, including also the limiting cases of the straight line and the circle, is the only curve allowing for such a separation, as follows from the proposition below.

Proposition. Condition (10) holds for a smooth, regular curve $\mathbf{r}(s)$ that is either closed or extends to infinity and is parametrized by its arc length $s \in \mathbb{R}$ if and only if the curve is a homogeneous helix.

The proof of this proposition is provided in the Appendix.

III. TWO CHARGED PARTICLES IN AN INHOMOGENEOUS HELICAL TRAP

In the following, we study the classical dynamics of two identical charged particles confined in a modified helix. The modification consists of a hump, i.e., a local change of

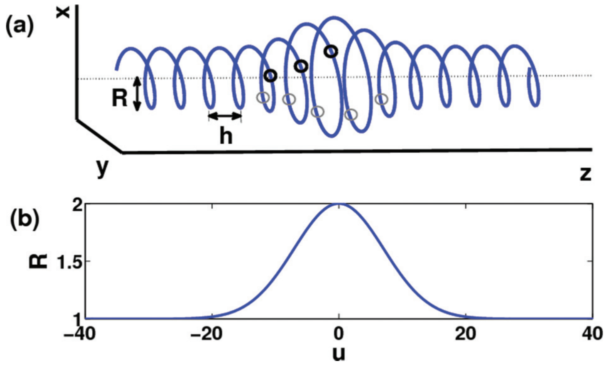

FIG. 1. (Color online) (a) Helix with a local modification of the radius $R(u)$ and a pitch h, as given by Eq. (11). (b) Local modulation of the radius as a function of the parameter u.

Gaussian form in the radius [Eq. (12)]. The interaction between the particles is given by a repulsive Coulomb potential

$$V(|\mathbf{r}_1 - \mathbf{r}_2|) = \frac{\lambda}{|\mathbf{r}_1 - \mathbf{r}_2|},$$

with $\lambda > 0$. We explore in particular the effects due to the coupling of the c.m. and relative motion in the presence of the helical hump.

The inhomogeneous helix parametrized by the angle parameter u is given by

$$\mathbf{r}(u) = \left(R(u)\cos(u), R(u)\sin(u), \frac{h}{2\pi}u\right) \tag{11}$$

with

$$R(u) = 1 + \epsilon \exp[-cu^2], \tag{12}$$

where both the modified radius $R(u)$ and the pitch of the helix h have been scaled with the radius of the corresponding uniform helix R_0. We use for the inhomogeneous helix the parameter values $\epsilon = 1$, $c = 0.01$, $h = 0.4\pi$. Figure 1 depicts the shape of such a helix and the localized radial modulation.

Since the particles are identical, $m_i = m$, we can choose dimensionless units by rescaling all quantities with m, λ, and R_0, i.e., introducing $\tilde m = \tilde\lambda = 1$ and

$$\tilde x = \frac{x}{R_0}, \quad \tilde t = t\sqrt{\frac{\lambda}{mR_0^3}}, \quad \tilde H = \frac{HR_0}{\lambda}, \quad \tilde p = p\sqrt{\frac{R_0}{m\lambda}}.$$

In the following, we omit for simplicity the tilde.

Performing then a Legendre transformation with $p_i = \frac{\partial L}{\partial \dot u_i}$, we obtain from (1) the Hamiltonian

$$H(\{u_i,p_i\}) = \frac{1}{2}\sum_{i=1}^{2} \frac{p_i^2}{[\partial_{u_i}\mathbf{r}(u_i)]^2} + \frac{1}{|\mathbf{r}(u_1) - \mathbf{r}(u_2)|}. \tag{13}$$

From this we deduce the equations of motion $\dot u_i = \frac{\partial H}{\partial p_i}$, $\dot p_i = -\frac{\partial H}{\partial u_i}$, which we solve numerically for different initial conditions with a Runge-Kutta method of fourth–fifth order with a variable time step size (ODE45). In order to study the dynamics in terms of c.m. and relative motion, it is desirable to have a Hamiltonian with a kinetic energy term of Cartesian form. This is achieved under the arc length parametrization (2) and leads to

$$H(\{s_i,\dot s_i\}) = \frac{1}{2}\sum_{i=1}^{2} \dot s_i^2 + \frac{1}{|\mathbf{r}(s_1) - \mathbf{r}(s_2)|}.$$

The s_i are obtained (numerically) via Eq. (2). Introducing c.m. $S = \frac{s_1+s_2}{2}$ and relative coordinates $s = s_1 - s_2$ yields the Hamiltonian

$$H(S,s,\dot S,\dot s) = \dot S^2 + \frac{\dot s^2}{4} + \frac{1}{|\mathbf{r}[u_1(S,s)] - \mathbf{r}[u_2(S,s)]|} \tag{14}$$

and the corresponding equations of motion

$$\begin{aligned} \ddot S &= -\frac{1}{2}\frac{\partial}{\partial S}\frac{1}{|\mathbf{r}[u_1(S,s)] - \mathbf{r}[u_2(S,s)]|}, \\ \ddot s &= -2\frac{\partial}{\partial s}\frac{1}{|\mathbf{r}[u_1(S,s)] - \mathbf{r}[u_2(S,s)]|}. \end{aligned} \tag{15}$$

We clearly observe here the coupling between S and s in the potential term. In the case of the uniform helix [20] the arc length integral can be solved analytically and the Hamiltonian can be written explicitly as

$$H(s,\dot S,\dot s) = \dot S^2 + \frac{\dot s^2}{4} + \frac{1}{\sqrt{2\left[1 - \cos\left(\frac{s}{a}\right)\right] + \left(\frac{h}{2\pi a}\right)^2 s^2}}, \tag{16}$$

with $a = \sqrt{1 + (\frac{h}{2\pi})^2}$.

For understanding the dynamics it is crucial to analyze the properties of the potential $V(S,s)$. Obviously, we have $\lim_{R\to\infty} V(R) = 0$. We focus first on the uniform helix for which $V = V(s)$ [see Eq. (16)] and thereafter we consider the case of the coupling of the c.m. and relative motion. Figure 2 shows the behavior of this potential curve for $s < 20$. We identify three potential wells which can support bound states and become shallower as s increases.

The potential $V(S,s)$, taking into account the hump, is illustrated in Fig. 3. Since it depends on both the c.m. S and the relative s coordinate, it represents a two-dimensional potential landscape.

We clearly observe two regions with a distinct behavior. The first, for large values of the c.m. coordinate $|S| \gtrsim 30$, presents a uniform behavior, approximately independent of S. It is affected only by the relative coordinate s in the same way as the

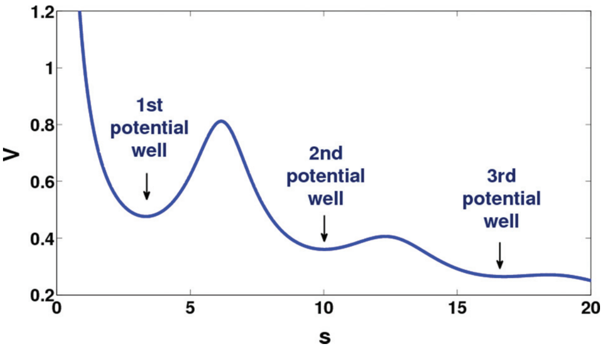

FIG. 2. (Color online) Potential curve for the uniform helix with parameters $h = 0.4\pi$ and $R = 1$. We observe three potential wells located at $s = 3.34$, 10.00, and 16.75 with minimum values $V = 0.48$, 0.36, and 0.26, respectively.

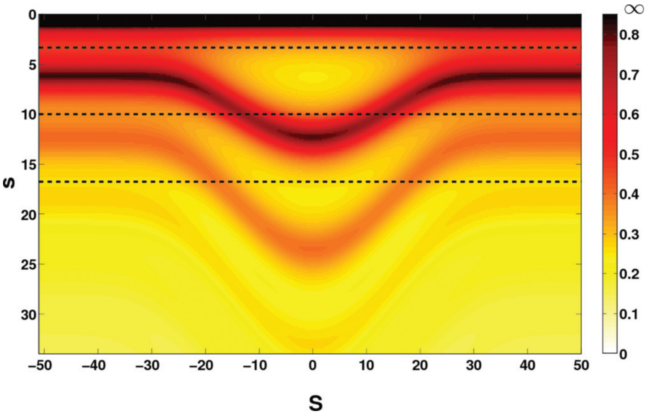

FIG. 3. (Color online) Contour plot of the potential $V(S,s)$ for the inhomogeneous helix. The dashed lines represent the positions of the minima of the three wells for the homogeneous case. The effect of the local modification of the radius is evident for $|S| \lesssim 30$.

potential of the homogeneous helix (Fig. 2), thereby presenting three wells for $|s| \approx 3,10,17$. In this uniform domain, the c.m. and the relative motion are thus decoupled. The second region, for $|S| \lesssim 30$, presents a strong dependence on the c.m. coordinate and thus constitutes a regime of strong coupling. The reader should note that the arc length (2) is taken w.r.t. the center of the hump and consequently regions with small S,s correspond to small s_i and lie in the inhomogeneous region of the helix.

Two effects are evident: each potential well becomes deeper and the contour lines bend in the regime of the inhomogeneity. Concerning the potential barriers, their maximum value decreases by ∼8% at the sides of the inhomogeneous region, whereas for $S \approx 0$ it retains the value of the homogeneous regime. All these effects can be explained by the modulation of the radius of the helix as discussed below.

Modulation of the radius and potential landscape. Since the pitch of the helix is much smaller than its circumference ($h < 2\pi R$) in both the homogeneous and the inhomogeneous regimes, the maximum and the minimum potential configurations occur for approximately constant values of the relative angle parameter $\tilde{u} = u_1 - u_2$, namely, for $\tilde{u}_{\max} = 2k\pi$ and $\tilde{u}_{\min} = (2k-1)\pi, k \in \mathbb{Z}$ [20], which for the first well ($k = 1$) correspond, respectively, to particles separated by one or half a winding of the helix (Fig. 4). The Euclidean distance between the particles at the minimum configuration increases substantially with the increment of the radius [Figs. 4(b) and 4(c)], reaching its maximum value at $S \approx 0$ [Fig. 4(c)] thereby resulting in a strong increase of the potential depth.

For the maximum configurations, the Euclidean distance increases as well off the center of the inhomogeneous region but, as it is shown in Fig. 4(b), this increment is small compared to that of the minimum configuration. At $S \approx 0$, the rate of change of the radius becomes small enough for the radius to be considered constant with twice the value of its homogeneous asymptotics [Fig. 4(c)]. However, the pitch h remains the same, resulting in the same Euclidean distance between the particles of the maximum configuration and thus leading to the same maximum potential values as that of the uniform domain [Fig. 4(c)]. The generalization to other potential wells (second, third) is evident in the regime $S \approx 0$: for the case of the maximum configuration, both particles are shifted by the same distance in the same direction whereas for the case of the minimum configuration by the same distance in opposite directions. This fact results both in an unaltered maximum value of the potential barrier and in a considerable increase of the potential depth.

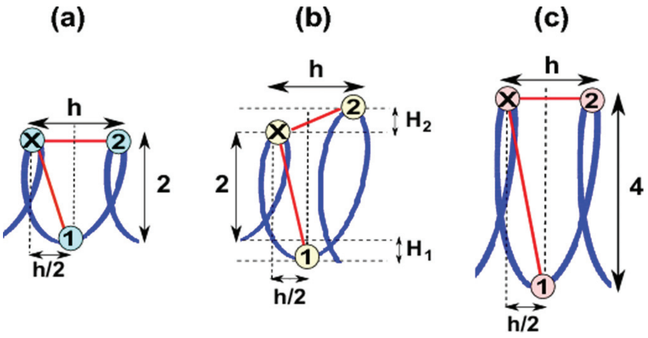

FIG. 4. (Color online) Euclidean distances of the particles for the minimum (⊗,①) and the maximum (⊗, ②) potential configurations of the first potential well for three different regions of the inhomogeneous helix: (a) the uniform domain of the helix with pitch h and radius $R = 1$, (b) the left side of the inhomogeneous region where the radius increases by H_1 at the bottom and by H_2 at the top, whereas the pitch remains the same, (c) the central part of the inhomogeneous domain $S \approx 0$, which since the modulation of the radius is stationary can be approximately treated as a part of a uniform helix with the same pitch h, but double radius $R = 2$.

Finally, we note that the contour lines of the potential bend inside the inhomogeneity towards larger s values as compared to the uniform domain. This effect is more pronounced for larger relative distances, i.e., for the third well as shown clearly in Fig. 3.

In the following sections, we will not discuss the dynamics of the system in terms of the trajectories $t \mapsto s_i(t)$ of two individual particles but rather in terms of that of a fictitious particle with two degrees of freedom, S and s, moving in the 2D potential of Fig. 3. This interpretation is suggested by the form of the Hamiltonian (14), which provides us with the respective equations of motion (15). Note, however, that these two degrees of freedom have different effective masses, a fact that needs to be taken into account when investigating the dynamics of the fictitious particle in terms of the potential gradients in the c.m. and the relative direction.

IV. SCATTERING OFF THE HELICAL HUMP

We analyze now the scattering behavior of a bound pair of charged particles confined in the inhomogeneous helix that has been described above. We assume that the particles start in the uniform domain, i.e., for $S \ll -30$ with $\dot{S} > 0$. We introduce S_h as the value of $|S|$ after which the helix as well as the potential are considered uniform. Specifically, we choose $S_h \approx 35.6$ for which the radius is identical to that of the homogeneous helix within 0.1%. The particles are further assumed to be initially bound, so their relative coordinate s lies within the region of one of the three wells discussed in Sec. IV. As they pass through the inhomogeneous region, energy is transferred between the c.m. and the relative degree of freedom due to the coupling. This transfer can lead to dissociation of the particles, which is reflected in the very low values of the interaction potential ($V \to 0$) at the end of the propagation (i.e., for $S \gg 30$).

We will initially discuss the case where the particles start with zero relative velocity $\dot{s} = 0$ at the minimum of each of the three wells (Sec. IV A) and then examine further the case of the first potential well for different initial conditions (Sec. IV B).

A. Initial conditions with zero relative momentum

First potential well. The particles are placed in the homogeneous domain ($S \ll 0$) of the helix, in the minimum of the first potential well $s = 3.34$ (Fig. 2), with $\dot{s} = 0$. We vary the initial values of the c.m. kinetic energy $T_S = \dot{S}^2$, over several orders of magnitude. The different initial conditions are propagated for a time period $t = 600$. After that time the particles have passed the region of inhomogeneity of the helix, the scattering process is in its asymptotic regime, and we can record the final values of the potential energy V, the relative energy $E_s = \frac{\dot{s}^2}{4} + V$, and the relative coordinate s. If the final value of V lies within the first potential well, i.e., $0.48 < V < 0.81$, then the particles have remained bound, whereas if V approaches zero they have dissociated through the scattering, which is also ensured by large values of the relative coordinate.

We clearly observe in Fig. 5(a) two regimes of finally bound configurations: $0 \leqslant T_S \leqslant 3.83$ and $T_S \geqslant 38.86$, separated by a region of dissociation $3.83 \leqslant T_S \leqslant 38.86$. For small T_S, below a critical value $T_{S_{c1}}$ it is expected that an energy transfer between the c.m. and the relative degree of freedom would not provide sufficient energy so that the particle can overcome the potential barrier. After $T_{S_{c1}} \approx 3.83$, dissociation becomes possible and it indeed occurs. However, the dissociation regime stops at a second critical value $T_{S_{c2}} \approx 38.86$, a fact that although counterintuitive from the point of view of the possible energy supply, can be explained by the limited range of the inhomogeneous region ($|S| \leqslant 30$). For very high c.m. velocities $\dot{S}$, the particles get through the inhomogeneity very fast, allowing for a very short interaction time only. The effect of the coupling is therefore very restricted, prohibiting a substantial energy transfer. In other words, the particles' motion is almost unaffected by the presence of the hump due to their large velocities. In the regime of bound states, the change of T_S induces a change of the s-oscillation phase at the end of the propagation ($t = 600$) leading to an oscillatory pattern of the final values of V and s. Another interesting feature of Fig. 5(a) is the behavior of the final relative energy E_s. In the middle of the dissociation region, it acquires values less than that of the potential barrier $V_{\max} \approx 0.81$, a fact that will be analyzed in Sec. IV B.

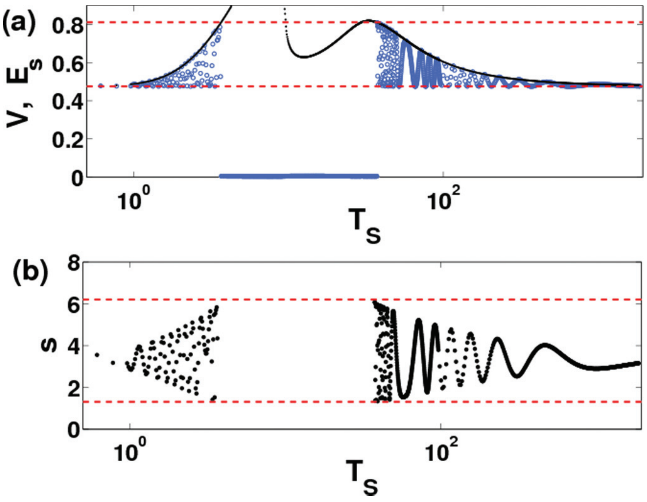

FIG. 5. (Color online) Overview of final bound and unbound states for initially bound states started in the first potential well: (a) Final potential values V [blue (gray) dots] and final relative energy values E_s (black dots) for different initial c.m. kinetic energies T_S. The dashed red lines represent the boundary potential values (minimum of well, maximum of barrier) of the first potential well. (b) Final relative coordinate values s (black dots) for different initial c.m. kinetic energies T_S. The dashed red lines represent the boundary values of those s which lie within the first potential well.

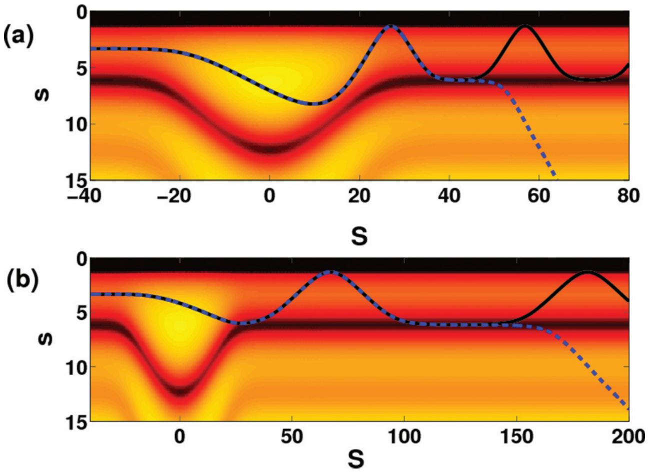

FIG. 6. (Color online) Finally bound (solid black line) and dissociated (dashed blue line) trajectories near (a) the first transition point $T_{S_{c1}} \approx 3.83$, (b) the second transition point $T_{S_{c2}} \approx 38.86$. The trajectories in each case [(a), (b)] differ in their c.m. velocities only by 0.001.

Let us next explore the behavior of the trajectories for T_S close to the critical values $T_{S_{c1}}, T_{S_{c2}}$, which will be referred to in the following as transition points. Our results are presented in Fig. 6. In both cases [Figs. 6(a) and 6(b)], a sharp transition from a bound to a dissociated final state occurs when T_S is fine tuned. This is depicted in the form of the corresponding trajectories which are essentially on top of each other for S less than a critical value S_c. This value is much larger for the second transition point with $T_{S_{c2}} > T_{S_{c1}}$, a fact that can be attributed to the larger value of the c.m. velocity. There is an evident transfer of energy to the relative degree of freedom depicted in the very large amplitude of the s oscillation of the fictitious particle for bound trajectories, after the scattering. With a slight increment of this transfer, the states dissociate after an oscillation. The trajectory of the fictitious particle is deflected inside the hump following the curved topology of the potential landscape until it comes across a large value of the potential barrier, where it becomes reflected backwards. From then on, it continues its regular path in the right homogeneous

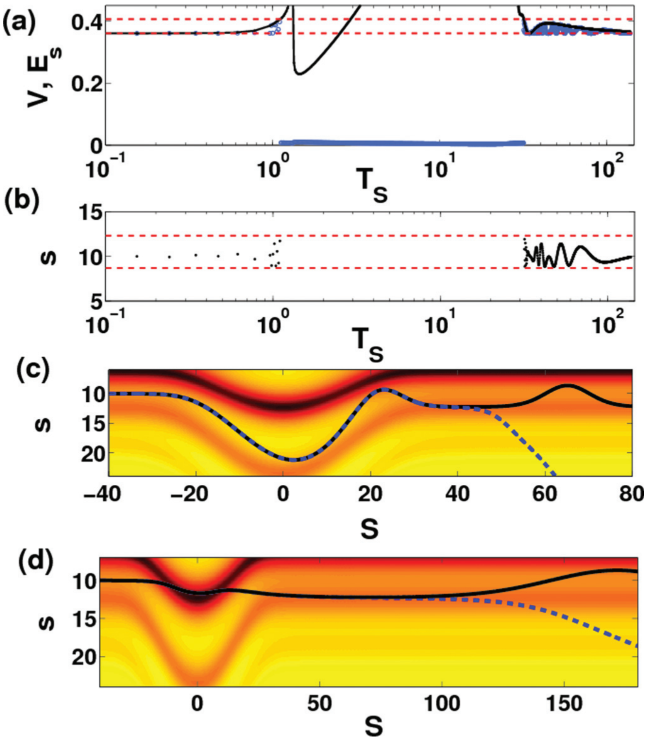

FIG. 7. (Color online) (a), (b) Same as in Fig. 5, but for particles starting in the second potential well. (c), (d) Same as in Fig. 6, but with (c) $T_{S_{c1}} \approx 1.15$, (d) $T_{S_{c2}} \approx 33.54$.

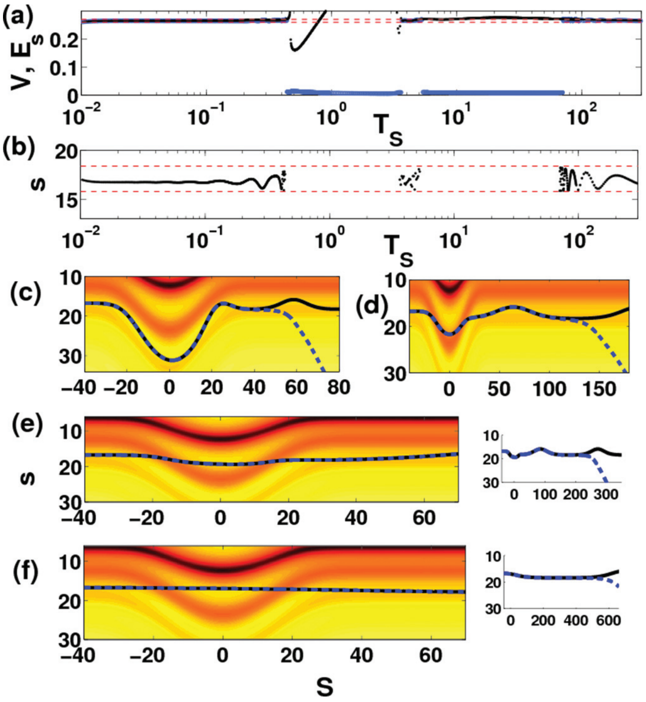

FIG. 8. (Color online) (a), (b) Same as in Fig. 5, but for particles starting in the third potential well. (c)–(f) Same as in Fig. 6, but with (c) $T_{S_{c1}} \approx 0.46$, (d) $T_{S_{c2}} \approx 3.76$, (e) $T_{S_{c3}} \approx 5.59$, (f) $T_{S_{c4}} \approx 70.35$. The small subfigures in (e) and (f) present the respective trajectories for large values of S, following them up to the point where the dissociative and bound trajectories separate from each other.

domain without any further energy transfer. As expected, the motion of the particle is much less affected (smaller angle of deflection) by the presence of the inhomogeneity for larger c.m. velocity [Fig. 6(b)] due to its inertia.

Second potential well. We now place the particles in the minimum of the second potential well $s = 10.00$ (Fig. 2) at the left homogeneous region, with zero relative velocity. Varying the c.m. kinetic energy T_S we observe again [Figs. 7(a) and 7(b)] a region of dissociation $1.15 \leqslant T_S \leqslant 33.53$ surrounded by regions of bound states, yielding two transition points: $T_{S_{c1}} = 1.15$ [Fig. 7(c)] and $T_{S_{c2}} = 33.53$ [Fig. 7(d)]. The dissociation region is overall shifted to lower values of T_S, compared to our previous results for the first potential well. From an energetical point of view, the shift of the first transition point $T_{S_{c1}}$ is expected since the potential barrier lowers, allowing for dissociation with less energy transfer. However, this argument alone would lead to a shift of $T_{S_{c2}}$ to larger values, contrary to what is observed here. The suppression of $T_{S_{c2}}$ seems to be a result of the bending of the potential landscape inside the hump. In particular, the straight line indicating the minimum of the second potential well in the homogeneous regime passes through the first potential well close to its barrier (Fig. 3). Trajectories with high enough c.m. kinetic energy $T_S \geqslant T_{S_{c2}}$ encounter this barrier and are forced to crest it [Fig. 7(d)], a fact that reduces abruptly the amount of the energy transfer and leads to extended binding. This effect is more pronounced in the case of the third potential well as discussed in the following.

Third potential well. Similarly to the previous cases, we now place the particles in the minimum of the third potential well $s = 16.75$ (Fig. 2) at the left homogeneous region, again with $\dot{s} = 0$. A variation of the c.m. kinetic energy T_S [Figs. 8(a) and 8(b)] provides us surprisingly with two distinct dissociation regimes $0.46 \leqslant T_S \leqslant 3.76$, $5.59 \leqslant \dot{S} \leqslant 70.35$, separated by a small region of bound states ($3.76 \leqslant T_S \leqslant 5.59$), leading to four transition points $T_{S_{c1}} = 0.46$, $T_{S_{c2}} = 3.76$, $T_{S_{c3}} = 5.59$, $T_{S_{c3}} = 70.35$ [Figs. 8(c)–8(f)].

This fact is a direct result of the bending of the potential landscape, which affects mainly the larger relative coordinates s, i.e., the third well. In particular, as depicted in Fig. 3, the straight line of the minimum of the third potential well passes, inside the hump, above the minimum of the second potential well. Due to the shallowness of the third potential well, only a very small amount of energy transfer ~0.01 is needed for the particles to overcome the barrier and dissociate, a fact that shifts the first transition point $T_{S_{c1}}$ to low values. When the fictitious particle has enough c.m. kinetic energy ($T_s \geqslant T_{S_{c2}}$), it crests the barrier of the second well, but since it gets directly deflected within it, it can not reach its inner region and the minimum [Fig. 8(d)]. This is similar to the case of the second transition point of the second potential well [Fig. 7(d)] and as in there, it is followed by a regime of bound states. However, if the c.m. velocity gets large enough ($T_{S_{c3}} = 5.59$), the fictitious particle is less deflected and can reach the region of the minimum of the second potential well [Fig. 8(e)], allowing for further energy redistribution between the two degrees of freedom. Thus, a second dissociation region occurs, which extends to very high values of $T_S \approx 70$, a fact that can also be attributed to the very small height of the potential barrier.

Nevertheless, even this height can not be overcome, when the fictitious particle acquires c.m. kinetic energy larger than $T_{S_{c4}}$, since the dwell time becomes very small, leading again to bound trajectories as in the cases of the other wells.

For this potential well, sharp transitions from a bound to an unbound state occur too at the four transition points as shown in Figs. 8(c)–8(f). It is evident that at the fourth transition point with a large value of T_S, the motion of the fictitious particle is only slightly affected by the inhomogeneity, tending to a straight line [Fig. 8(f)].

We emphasize that since the equations of motion of the system [Eq. (15)] possess a time reversal symmetry, the transitions from bound to unbound states can be directly mapped into transitions from free states to bound ones. The creation of bonds through scattering is surprising, especially in view of the fact that the particles interact via a repulsive Coulomb potential. For these reasons, we find it interesting to examine this process further below.

B. Initial conditions with nonzero relative velocity in the first potential well

We investigate now the scattering for arbitrary initial conditions, focusing on the first potential well. When the particles are in the uniform domain of the helix, inside the first well with a nonzero relative velocity, the fictitious particle performs an oscillation in the relative coordinate s. The phase of this oscillation when the fictitious particle enters the hump affects the energy transfer between the c.m. and the relative motion. Moreover, the value of the relative initial energy E_s plays a crucial role in determining which states become dissociated since states with higher E_s require less amount of energy transfer in order to overcome the potential barrier. Thus, for a complete description of the scattering process, we need except from the initial center of mass kinetic energy T_S to specify two other parameters, namely, the initial relative energy and the phase of the relative oscillation.

For reasons of convenience, we assume that the fictitious particle starts at a point $1.3 < s_{0L} \leqslant s_{\min} = 3.34$ of the first potential well in the uniform domain with zero relative velocity $\dot{s} = 0$. In other words, s_{0L} is the left turning point of the oscillation in the relative coordinate and is related to the total relative energy by $E_s = V(s_{0L})$, with V being the potential of the homogeneous regime given by Eq. (16). We denote the right turning point for the same energy with s_{0R}.

We represent the phase of the oscillation by the parameter $0 \leqslant \frac{t}{T} < 1$ which stands for the fraction of the period of the relative oscillation

$$T = 2\int_{s_{0L}}^{s_{0R}} \frac{ds'}{\sqrt{2[E_s - V(s')]}}$$

at which the particles enter the hump. In such a way, $\frac{t}{T} = 0$ corresponds to particles at s_{0L} with $\dot{s} = 0$ at the entrance point $S_{hL} = -S_h$, whereas $\frac{t}{T} = 0.5$ corresponds to particles at s_{0R} with $\dot{s} = 0$. This parameter can be adjusted by changing the initial c.m. coordinate S in the homogeneous region, while keeping $\dot{S}$ fixed. Due to our genuine interest in the scattering properties with varying phase, the absolute phase dependence induced by the arbitrariness of S_h is rendered irrelevant.

Our results are presented in Fig. 9 for nine representative values of s_{0L}, ranging from energies close to the potential minimum ($s_{0L} \approx 3.3$) to close to the potential barrier height ($s_{0L} \approx 1.3$). Each such value produces a slice which imprints the dependence of the property under consideration on the other two parameters: T_S and $\frac{t}{T}$.

Figure 9(a) provides us with the finally bound and unbound states for the different initial conditions. For $s_{0L} \approx 3.3$, close to the minimum, we observe that the phase of oscillation $\frac{t}{T}$ does not affect the behavior of the system, as expected, and we regain the results of Sec. IV A with a single dissociation region of a rectangular shape for different c.m. kinetic energies T_S. The shape of this regime is deformed as we go to higher relative energies (smaller s_{0L}) and it develops a dip. By increasing further E_s the dissociation area breaks into two parts for a certain regime of initial phases $\frac{t}{T}$, providing us with two dissociation regions with varying T_S. As we approach the threshold energy for passing the potential barrier ($s_{0L} \approx 1.3$), we observe an alternating sequence of bound and dissociation regions, even at very low c.m. kinetic energies. This is a surprising feature which makes the dissociation process sensitive to even small changes of the underlying parameters, such as the initial value of T_S in the scattering process.

In Fig. 9(b), we present our results for the relative amount of gain or loss of the maximum relative kinetic energy $(T^s_{\max_f} - T^s_{\max_i})/E_s$ through the scattering. Clearly, the regions of high positive $(T^s_{\max_f} - T^s_{\max_i})/E_s$ match exactly with the dissociation regions of Fig. 9(a). Most regimes show almost zero total gain of kinetic energy, but surprisingly enough there are also regimes where the kinetic energy of the relative motion is decreased after the scattering. These regions of loss predominately appear between the different regimes of dissociation and are characterized by particles becoming more tightly bound in the course of scattering. A further interesting observation can be made in Fig. 9(c), which shows the difference $E_{s_f} - V_{\max}$ of the final relative energy E_{s_f} and the maximum value of the potential barrier of the first well $V_{\max}$. In particular, this difference is negative not only for the finally bound states, but also for some of the finally dissociated ones. The dissociation regions consist of states with $E_{s_f} \geqslant V_{\max}$ at their boundaries and of ones with $E_{s_f} \leqslant V_{\max}$ at their center. The dissociated states with $E_{s_f} \leqslant V_{\max}$ might seem counterintuitive but, as it will be shown below, these result from trajectories for which the particles dissociate within the hump, where the coupling of the c.m. and relative motion is still substantial. Since the potential barrier in this region is bent (Fig. 3), the fictitious particle overcomes it with its total amount of energy $E = T_s + T_S + V(S,s)$, and thus its final relative energy can be less than $V_{\max}$. Such a phenomenon has already been encountered in our investigations of Sec. IV A.

Trajectories. As we have seen throughout this section, the initially bound trajectories are divided into two different categories: those which remain finally, i.e., after scattering, bound and those which are led to dissociation. It is evident that the finally dissociated trajectories can be further classified into those that dissociate after reaching the uniform region (type A) and those that dissociate within the hump (type B). Since they reach the homogeneous domain (Fig. 10), the dissociated trajectories of type A have more features in common with the bound ones

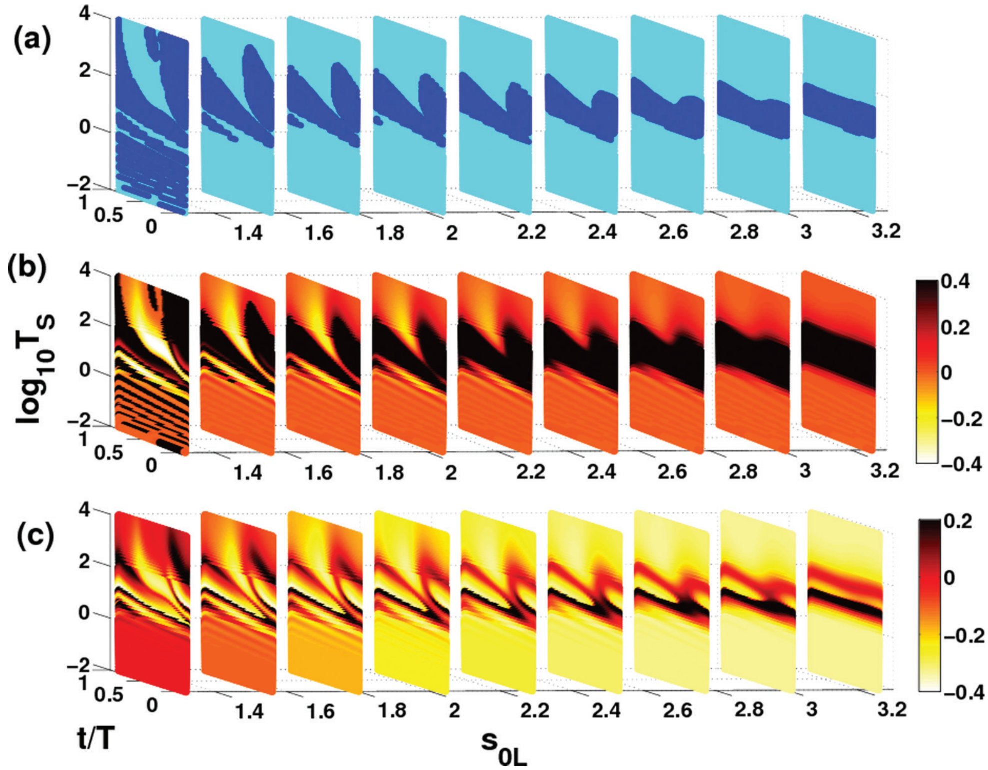

FIG. 9. (Color online) (a) States that after scattering remain bound [cyan (light gray) regions] and states that are led to dissociation [blue (dark gray) regions], (b) color encoded values of the relative difference between the final and the initial maximum kinetic energy of the relative motion $(T^s_{\max_f} - T^s_{\max_i})/E_s$, (c) color encoded values of the difference between the final relative energy E_{s_f} and the maximum value of the potential barrier of the first well $V_{\max}$ for different s_{0L} (x axis), $\frac{t}{T}$ (y axis), and $\log_{10} T_S$ (z axis).

and this is the reason why they always occur close to the transition points. States of type B, on the other hand, are fundamentally distinct (Fig. 10) and occur only in the middle of the dissociation regions [Fig. 9(c)]. The main difference of A and B trajectories is imprinted in the energy transfer. Type A trajectories have always final relative energy greater than the potential barrier and overall can be thought as cases where a substantial amount of energy has been transferred from the c.m. to the relative motion. However, the trajectories of type B pass the potential barrier with their total amount of energy E. Since they remain in the inhomogeneous regime for some time after dissociation, a redistribution of energy between the c.m. and the relative motion is still possible, leading to a sequence of loss and gain of relative energy. Therefore, their final relative energy E_s can be lower than the height of the potential barrier [Fig. 9(c)].

Figures 10 and 11 specify the above line of arguments and identify in particular the different types of trajectories. For a constant value of s_{0L}, sufficiently away from the potential minimum, one can induce transitions of the form

$$A \rightarrow B \rightarrow A \rightarrow \text{bound states} \rightarrow \text{A}$$

by varying either the c.m. kinetic energy [increasing T_S, Fig. 10(a)], or the phase of the relative oscillation [decreasing $\frac{t}{T}$, Fig. 10(b)].

Figure 11 provides us with the complementary information of how the change of the initial relative energy E_s, imprinted in s_{0L}, affects the evolution of the trajectories. The trajectories presented for each s_{0L} have the same T_S and different phases $\frac{t}{T}$. For $s_{0L} = s_{\min}$ [Fig. 11(a)], a case familiar from Sec. IV A, the fictitious particle does not oscillate and thus the trajectories are independent of the phase. For the value of T_S chosen here, this set of trajectories constitutes a single dissociated state of type A. Increasing the relative energy (decreasing s_{0L}), the trajectories for various phases start to separate, but still their type remains the same [Fig. 11(b)]. A further increment of E_s [Fig. 11(c)] has as a result the formation of dissociative states of type B for certain values of phases. Finally, for s_{0L} sufficiently close to the potential barrier [Fig. 11(d)], the amplitude of the relative oscillation increases dramatically, allowing for the emergence of all the three types of trajectories, including finally bound states.

Energy transfer. Throughout this section, we have come across intriguing effects originating from the coupling between the c.m. and the relative coordinate. The key ingredient allowing for these effects is the energy transfer between the two degrees of freedom inside the inhomogeneous region. Let us therefore point out some basic features of the energy exchange process. To do so, we consider the change of the kinetic energy of the c.m. T_S. The latter is zero in the uniform regime of the helix. From the equations of motion for the Hamiltonian (14), we obtain $\dot{T}_S = -\dot{S}\frac{\partial V}{\partial S}$, where $V = V(S,s)$. Although this relation for $\dot{T}_S$ refers to certain time evolving trajectories, we find it instructive to analyze its contour plot for a certain value of $\dot{S} = 1$.

We observe in Fig. 12(a) that for a constant value of the c.m. velocity, the rate of change of T_S is nonzero only

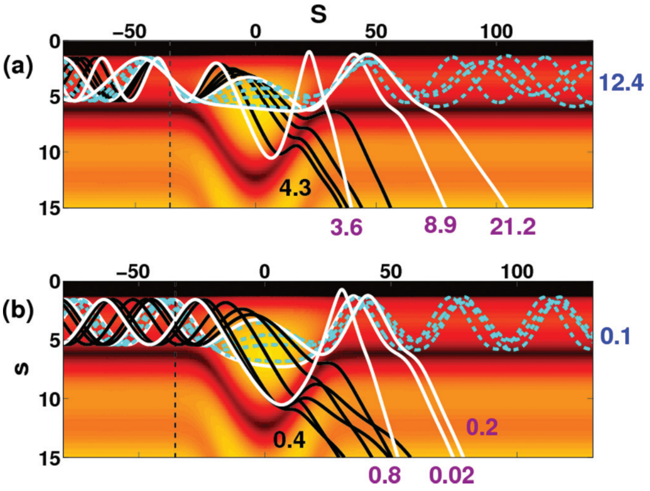

FIG. 10. (Color online) (a) Trajectories with different c.m. kinetic energies T_S for $s_{0L} \approx 1.56$ and $\frac{t}{T} = 0.22$. The numerical values presented in the diagram correspond to the values of T_S for the different kinds of trajectories. (b) Trajectories with different phases of relative oscillation $\frac{t}{T}$ for $T_S = 8.88$ and $s_{0L} \approx 1.56$. The numerical values presented in the diagram correspond to the values of $\frac{t}{T}$ for the different kinds of trajectories. In both cases, the dissociative trajectories of type A are shown with solid white lines, while those of type B are represented with solid black lines. The finally bound trajectories are presented with dashed cyan lines. The vertical black dashed line indicates the position S_{hL} at which the hump starts (by definition).

in the inhomogeneous regime as expected. Moreover, it is antisymmetric with respect to the center of the hump $S = 0$, meaning that if at $(-S,s)$ the particle gains T_S, it loses at (S,s). Therefore, almost symmetric trajectories ($S \rightarrow -S$), as those for very large or very small initial c.m. velocity $\dot{S}_0$, will have finally almost zero energy transfer. However, since T_S, moving from a positive $\dot{T}_S$ value to a negative one, reaches a maximum for these trajectories inside the inhomogeneity (at $S \approx 0$), the average kinetic energy of the c.m. motion inside the hump will be larger than that in the homogeneous regime. This in turn leads to a larger effective $\dot{S}$ within the inhomogeneity and a smaller dwell time (defined as the time interval during which the fictitious particle moves from $-S_h$ to S_h) than the one expected by $\dot{S}_0$. This effect is evident [Fig. 12(b)] only in the case of small $\dot{S}_0$, where even a slight increment in the velocity affects substantially the value of the dwell time.

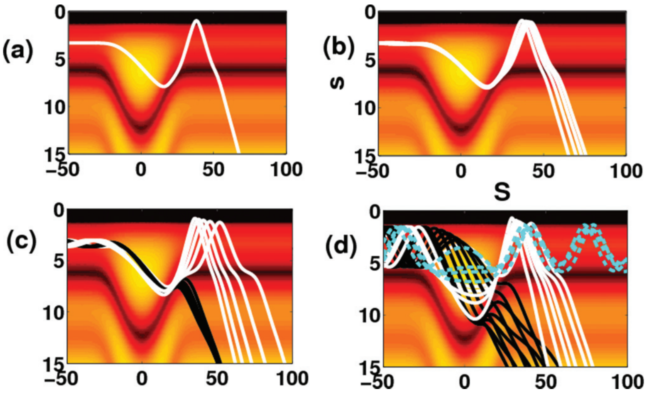

FIG. 11. (Color online) Trajectories for various phases of relative oscillation $\frac{t}{T}$ for $T_S = 8.88$ and (a) $s_{0L} = s_{\min} = 3.34$, (b) $s_{0L} = 3.26$, (c) $s_{0L} = 2.53$, (d) $s_{0L} = 1.56$. Solid white lines stand for finally dissociated states of type A, solid black lines for type B, and dashed cyan lines for finally bound states.

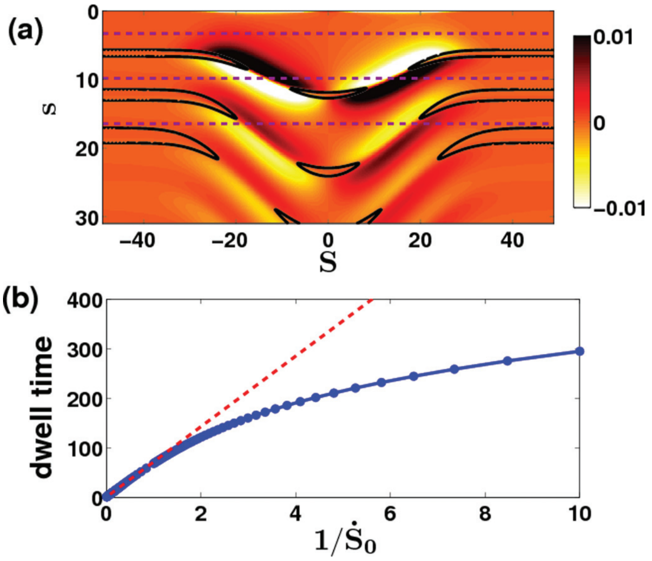

FIG. 12. (Color online) (a) The rate of change of the kinetic c.m. energy $\dot{T}_S$ as a function of S,s for $\dot{S} = 1$. The solid black lines depict the position of the maxima of the three potential barriers, while the dashed brown lines indicate the position of the minima of the three potential wells in the uniform regime (see also Fig. 3). (b) The dwell time as a function of the initial c.m. velocity $\dot{S}_0$ for the particles starting at the minimum of the first potential well with zero relative velocity (blue line with circles). For small $\dot{S}_0$, the deviation from a motion with constant $\dot{S} = \dot{S}_0$ dictated by the red dashed line is evident.

The greatest amount of energy can be gained or lost when the fictitious particle passes deep in the potential well, close to the potential barrier, since the gradient $\frac{\partial V}{\partial S}$ acquires there its largest values [Figs. 3 and 12(a)]. For $\dot{S} > 0$, which is always true for particles passing from the left homogeneous regime to the right one, the c.m. gains kinetic energy while being in the first potential well in the region $S < 0$, and it loses for $S > 0$. This causes highly asymmetric trajectories as some with $\dot{S}_0 > 1$ (Figs. 10 and 11) overall to lose an amount of c.m. kinetic energy, which after reaching the uniform regime appears as a gain in the total relative energy. Trajectories that dissociate within the hump (type B), after crossing the top of the potential barrier for $S > 0$, regain c.m. kinetic energy T_S [Figs. 3 and 12(a)], but since they continue moving at lower values of the potential this does not always result in lower final values of total relative energy. Therefore, we may conclude that all the dissociative trajectories with a lowered final E_s belong to type B, but not vice versa.

Overall, it is evident that the energy transfer consists of subsequent losses and gains of T_S and T_s induced by the variations of the potential $V(S,s)$ inside the inhomogeneous region, leading to a final asymptotic effective gain or loss.

V. PHASE SPACE ANALYSIS

We explore now the structure of the underlying phase space of the scattering process and in particular of bound states in the inhomogeneity of the helix. Since the three potential wells display similar characteristics, with the first one allowing for more variations in energy since it is the deepest one, it will be the only one we consider here. For Hamiltonian systems with two degrees of freedom, the standard tool for such an analysis is the Poincaré surface of section (PSOS), taking advantage of the conservation of energy. Here, we will choose $S = 0$ ($P > 0$) as the intersection through the energy shell. We note that the PSOS shown in the following report only the bound state trajectories.

Let us inspect the regions of bound and unbound motion within the inhomogeneous helix. The only part of the potential landscape $V(S,s)$ that can support bounded motion is that of the inhomogeneity, i.e., inside the hump, in the neighborhood of $S \approx 0$. Since the potential wells possess finite barriers, it is evident that for energies beyond a certain amount the fictitious particle can escape to infinity concerning either the c.m. S or the relative coordinate s, leading to dissociation.

For the first potential well, this fact is clearly depicted (Fig. 13) through the equipotential lines (EPLs). For $E \leqslant E_{c_1} = 0.476$, with E_{c_1} being the energy of the minimum of the first potential well in the uniform domain, the EPLs are closed both in the S and s directions [Figs. 13(a)–13(c)] leading to exclusively bounded motion inside the hump. Figure 13(c) presents the critical case, a fact that is reflected in the substantial elongation of the wings of the EPL. A further increment of the energy leads to EPLs extending to $|S| \to \infty$ [Figs. 13(d)–13(f)] which allows for escaping trajectories from the center of the hump to the homogeneous regime of the helix. This holds until the second critical value $E_{c_2} = 0.744$ [Fig. 13(e)] is reached. From then on, two additional openings are formed in the EPL inside the central region of the hump [Fig. 13(f)] allowing also for escapes in the relative coordinate.

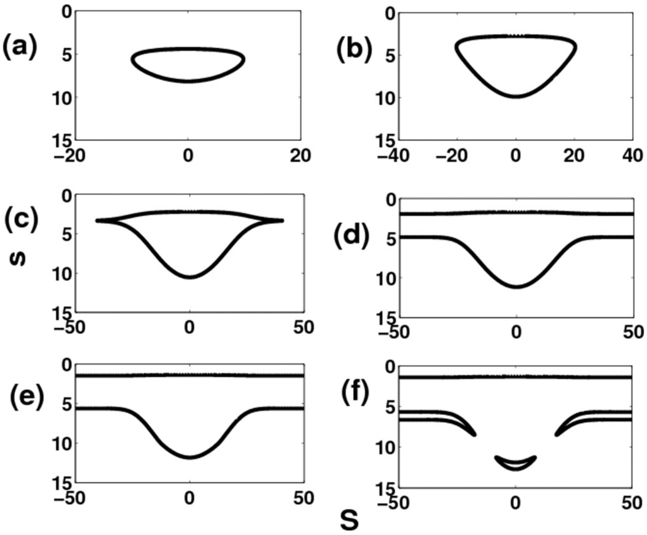

FIG. 13. EPLs of the first potential well for representative total energies: (a) $E = 0.28$, (b) $E = 0.39$, (c) $E = 0.476$, (d) $E = 0.6$, (e) $E = 0.744$, and (f) $E = 0.76$.

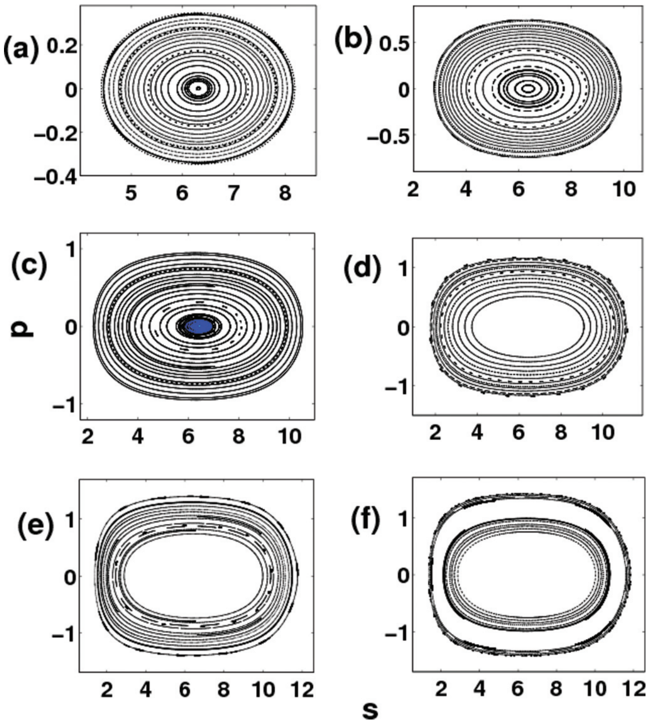

FIG. 14. (Color online) Poincaré surfaces of section for representative total energies: (a) $E = 0.28$, (b) $E = 0.39$, (c) $E = 0.476$, (d) $E = 0.6$, (e) $E = 0.744$, and (f) $E = 0.76$. The inner region of (c) (blue dots) consists of chaotic trajectories.

For energies larger than the maximum value of the first potential well $V_{\max} = 0.81$, of course, the particles' motion is in principle unbounded.

Figure 14 shows PSOS for different energies. For $E < E_{c_1}$ [Figs. 14(a) and 14(b)], we observe an elliptic island. Close to the first transition point $E = E_{c_1}$ [Fig. 14(c)] it develops in its inner region, i.e., for small p and s close to the absolute minimum of the first potential well, a chaotic portion. A further increase of the energy leads to escaping trajectories, which is evident in Fig. 14(d) where a large part of the inner region of the surface of section (empty region) belongs to escaping trajectories ($|S| \to \infty$) through the respective openings of the EPL [Fig. 13(d)]. As the energy approaches its second critical value E_{c_2} [Fig. 14(e)], the basin of escape becomes larger and finally for $E > E_{c_2}$ [Fig. 14(f)], a second area of the surface of section empties, this time in the center of the region of bounded motion. This corresponds to trajectories that escape in the s direction (dissociation) through the two additional openings on the lower side of the corresponding EPL [Fig. 13(f)].

Figures 15, 16, and 17 provide further details enriching the above analysis in terms of specific trajectories. First, we remark that the turning points of the trajectories both in the s and S directions lie on the EPLs of the respective energy. Trajectories with a larger S elongation and a reduced s amplitude follow obviously the bending of the potential landscape and are the ones that map to the inner region of the Poincaré surface of section. As we move to the outer region of the surface of section, the amplitude in s increases with a respective decrease of the amplitude in the S direction. For energies $E_{c_1} < E < E_{c_2}$ trajectories can escape from the left and right openings

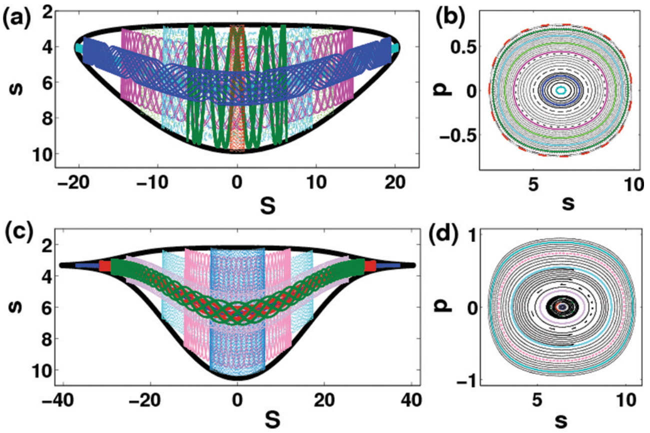

FIG. 15. (Color online) Selected trajectories (a), (c) and respective PSOS (b), (d) for the energies: (a), (b) $E = 0.39$, (c), (d) $E = 0.4761$. The color of the trajectories corresponds to their position in the PSOS. In (a), (c) the EPLs are also depicted as in Fig. 13.

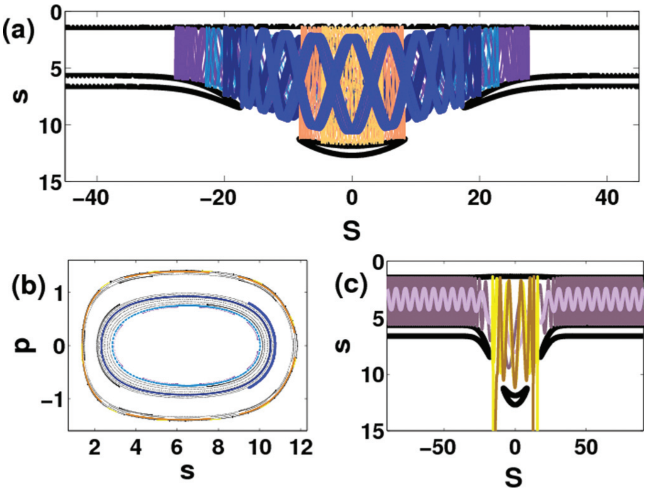

FIG. 17. (Color online) (a) Selected bound trajectories, (b) PSOS, and (c) escaping trajectories both in the c.m. S (bound states) and in the relative coordinate s (free states) for energy $E = 0.76$.

of the respective EPL [Fig. 16(c)]. In order to be bound, the trajectories should have an amplitude of the relative motion exceeding the width of the openings of the EPL [Fig. 16(a)]. This is the reason why for the PSOS the regime of bounded motion is located in the outer part, with the inner one being empty and corresponding to escaping trajectories [Fig. 16(b)].

A more detailed nonlinear dynamical analysis would most probably reveal two unstable periodic orbits that provide the connection between the bounded and escaping motion. To explore this in detail goes, however, beyond the scope of this work, which has its emphasis on the main phenomena appearing in the helical dynamics investigated here.

Bridging between bound and unbound there are "resonant" trajectories, i.e., trajectories that remain within the hump performing oscillatory c.m. and relative motion, for a large time interval and finally escaping to the homogeneous asymptotic region. They have typical initial conditions in the empty region of the PSOS [Fig. 16(b)], close to the innermost bound trajectory. Such a trajectory is presented in Fig. 18. It escapes to the left opening of the potential well ($S < 0$) both in forward and in backward propagation time, i.e., it is reflected at the helical hump.

A more complex structure of the PSOS is encountered for $E_{c_2} < E < V_{\max}$. In such a case, as we have remarked earlier, there are four openings of the EPL. Subsequently, four unstable periodic orbits exist and thus four possibilities for escape symmetric with respect to $S = 0$ [Fig. 17(c)]: two in the c.m. coordinate direction (S openings) as before and two in the relative one (s openings). The escape in the S direction (small s, large S, i.e., $s_1 s_2 > 0$) both in forward and in backward propagation time, corresponds to a bound pair of particles that after scattering within the hump remains bound, a case that has been referred to in the previous section as a bound state. On the contrary, escapes in the s direction (large s, small S) correspond to free particles that come from opposite sides

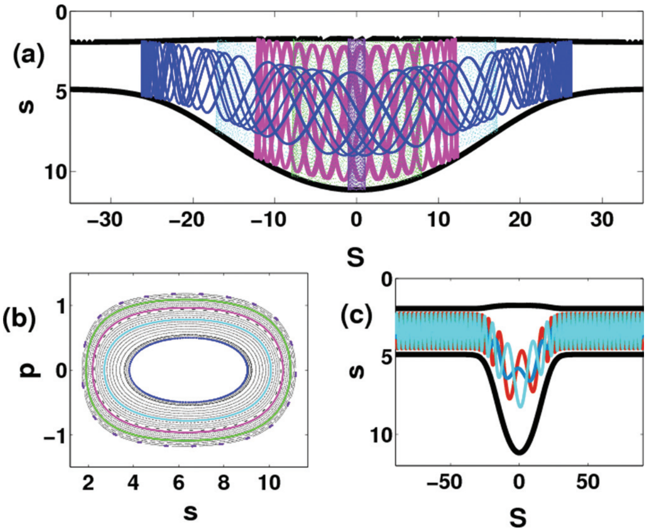

FIG. 16. (Color online) (a) Selected bound trajectories, (b) PSOS, and (c) escaping trajectories in the c.m. S coordinate for the energy $E = 0.6$.

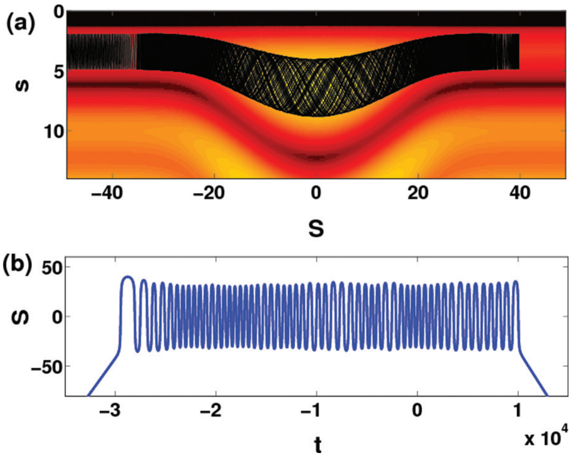

FIG. 18. (Color online) A resonant trajectory for $E = 0.6$ and initial conditions $S = 0$, $s = 5.134$, $\dot{S} = 0.549$, $\dot{s} = -0.387$: (a) plot of the trajectory on the potential landscape, (b) time evolution of the c.m. coordinate S of the trajectory.

of the helical trap ($s_1 s_2 < 0$), scatter within the hump, and return backwards in opposite directions. They thus account for conventional scattering of free particles and are different from the peculiar dissociative states we have observed so far.

Between the regimes of escapes, there are two distinct regions of bounded trajectories [blue (dark gray) and orange (light gray), Fig. 17(a)]. The first of them consists of trajectories supported by the side parts of the EPL. Their relative oscillation s amplitude is bounded both from below, by the width of the S opening in the uniform domain, and from above by its edge width inside the inhomogeneous region. The second consists of bound states with somewhat larger relative s amplitude dictated by the width of the central part of the EPL. These considerations give rise to the two-ring structure of the PSOS [Fig. 17(b)].

VI. SUMMARY AND OUTLOOK

We have investigated the classical scattering of Coulomb interacting particles in a helix. First, we have proven that for two particles interacting via a potential that depends exclusively on their Euclidean distance, a separation of the c.m., leading to a conservation of the total momentum, is provided if and only if the confining curve is a homogeneous helix. Having this result in mind, we investigated the scattering of charged particles from a local inhomogeneity of the helix. In such a system, the coupling between the c.m. and the relative degrees of freedom induces intriguing effects. The most important of them is the dissociation of initially bound states of the two repulsively interacting charged particles through scattering. Due to the time reversal symmetry imprinted in the equations of motion, this leads to the conclusion that initially unbound charged particles can become bound when scattered, a fact counterintuitive regarding especially the repulsive character of the interaction.

The underlying mechanism for such a behavior was found to be the effective energy transfer between the relative and the c.m. motion occurring due to their coupling. It has been pointed out, nevertheless, that this transfer does not take place in a single step, but it is the final result of the continuous energy redistribution in the whole time interval in which the particles remain inside the hump. For this reason, the outcome of the scattering of initially bounded charged particles in terms of finally bound and dissociated states depends in a rather complex way on the initial conditions. The dissociation regimes depending on these conditions have been identified and analyzed in detail. The most important parameter is shown to be the value of the initial kinetic energy of the c.m. T_S. In most cases, for very small or very large values of T_S the particles remain bound after the scattering, with dissociation occurring only in the intermediate regime. This is attributed to the little amount of energy available for transfer and to the small dwell time in the hump that prevents a strong coupling of the relative and c.m. degrees of freedom, respectively.

Our analysis has been completed with an exploration of the phase space structure of the deepest potential well that can support bound states. Regimes of bound regular motion inside the hump, as well as regimes of escapes, were identified by varying the total energy. This exploration provided us with bound states localized inside the hump, as well as with "resonant trajectories."

Further studies could be dedicated to a more detailed investigation of the phase space searching for stable and unstable periodic orbits and their asymptotic curves, a fact that would allow a rigorous and quantitative analysis of the escape procedure. A promising direction is the study of many-body systems which are expected to exhibit an intriguing dynamics as well as leading to exceptional transition phenomena.

ACKNOWLEDGMENTS

We thank M. Jüngling for many helpful discussions and his support concerning the theoretical conceptual aspects of this work. A.Z. thanks the International Max Planck Research School for Ultrafast Imaging and Structural Dynamics for support through a Ph.D. scholarship. J.S. and S.K. gratefully acknowledge funding by the Studienstiftung des deutschen Volkes.

APPENDIX: CONDITIONS ON THE CURVED 1D MANIFOLD FOR THE SEPARATION OF THE CENTER OF MASS FROM THE RELATIVE MOTION

Proposition. The condition

$$\partial_{s_1} R(s_1,s_2) + \partial_{s_2} R(s_1,s_2) = 0, \forall\, s_1,\, s_2 \in \mathbb{R}, \qquad \text{(A1)}$$

where $R(s_1,s_2) = |\mathbf{r}(s_1) - \mathbf{r}(s_2)|$ holds for a smooth, regular curve $\mathbf{r}(s)$ in arc length parametrization if and only if the curve is a homogeneous helix (including the degenerate cases of a circle or a straight line).

Proof. "$\Leftarrow$": By the discussion in Sec. II, condition (A1) is equivalent to separability of c.m. and relative motion, which has been demonstrated to hold for a homogeneous helix (see discussion in the main text).

"$\Rightarrow$": Assume that condition (A1) holds. The outline of the proof is as follows. We show that by virtue of Eq. (A1), for each $x \in \mathbb{R}$ the map

$$F_x : \mathcal{W} \mapsto \mathcal{W}, \quad F_x[\mathbf{r}(s)] = \mathbf{r}(s+x) \qquad \text{(A2)}$$

is an isometry (i.e., it preserves distances) on the submanifold $\mathcal{W} \subseteq \mathbb{R}^3$, which is defined as the image of the curve $\mathbf{r}$. We extend this family of isometries to a family of isometries $\{\Gamma_x\}_{x\in\mathbb{R}}$ from all of $\mathbb{R}^3$ into itself, with the property that the restriction $\Gamma_x\big|_{\mathcal{W}} = F_x$. The isometries of $\mathbb{R}^3$ form the group of Euclidean moves $E(3)$. Since the Γ_x are continuously deformed to the identity map for $x \to 0$, they belong to the identity component of $E(3)$, i.e., to $SE(3)$. Thus, by the classification theorem for Euclidean moves [22] each Γ_x is a screw operation or a degenerate case thereof, i.e., a pure rotation or translation. Furthermore, not all Γ_x can be the identity on $\mathbb{R}^3$. Thus, there is a nontrivial continuous family of screw operations $\{\Gamma_x\}_x$, including the identity, that map the curve $\mathcal{W}$ to itself. In particular, there is an infinitesimal screw operation whose repeated action on any point of $\mathcal{W}$ maps the point to $\mathcal{W}$ again. So $\mathcal{W}$, the image of $r(s)$, must be a (homogeneous) helix, which proves the proposition.

We now proceed to the detailed proof and first show that, given Eq. (A1), the map F_x as defined in (A2) is an isometry on $\mathcal{W}$. First, we prove that there is a function χ

such that $R(s_1,s_2) = \chi(s_1 - s_2)$. To see this, introduce new variables $\xi_- := s_1 - s_2$, $\xi_+ := s_1 + s_2$ and a function χ with the property $\chi(\xi_+,\xi_-) = R(s_1,s_2)$. Then, condition (A1) yields $\partial\chi/\partial\xi_+ = 0$, leading to $\chi(\xi_+,\xi_-) = \chi(\xi_-)$ or

$$R(s_1,s_2) = \chi(s_1 - s_2).$$

This, in turn, immediately implies $R(s_1,s_2) = R(s_1 + x, s_2 + x)$, or

$$|\mathbf{r}(s_1) - \mathbf{r}(s_2)| = |\mathbf{r}(s_1 + x) - \mathbf{r}(s_2 + x)|$$

for all $x,s_1,s_2 \in \mathbb{R}$, showing that indeed F_x as defined above is an isometry on $\mathcal{W}$.

We now assume without loss of generality that $\mathbf{0} \in \mathcal{W}$ and proceed to show that for all x the map

$$\tilde{F}_x : \mathcal{W} \mapsto \mathbb{R}^3, \quad \tilde{F}_x(\mathbf{r}) := F_x(\mathbf{r}) - F_x(\mathbf{0})$$

has the following properties:
(i) $|\tilde{F}_x(\mathbf{r})| = |\mathbf{r}| \quad \forall\, \mathbf{r} \in \mathcal{W}$.
(ii) $\sigma(\tilde{F}_x(\mathbf{r}_1),\tilde{F}_x(\mathbf{r}_2)) = \sigma(\mathbf{r}_1,\mathbf{r}_2) \quad \forall\, \mathbf{r}_1,\mathbf{r}_2 \in \mathcal{W}$.
(iii) $\tilde{F}(\alpha_1\mathbf{r}_1 + \alpha_2\mathbf{r}_2) = \alpha_1\tilde{F}_x(\mathbf{r}_1) + \alpha_2\tilde{F}_x(\mathbf{r}_2)$
$\forall\, \mathbf{r}_1,\mathbf{r}_2 \in \mathcal{W}$, $\alpha_1,\alpha_2 \in \mathbb{R}$ s.t. $\alpha_1\mathbf{r}_1 + \alpha_2\mathbf{r}_2 \in \mathcal{W}$.
Here, σ denotes the Euclidean scalar product. (i) immediately follows from F_x being an isometry on $\mathcal{W}$. (ii) follows from (i) and F_x being an isometry since $\forall\, \mathbf{r}_1,\mathbf{r}_2 \in \mathcal{W}$,

$$\begin{aligned}
&2\sigma(\tilde{F}_x(\mathbf{r}_1),\tilde{F}_x(\mathbf{r}_2))\\
&\quad = |\tilde{F}_x(\mathbf{r}_1)|^2 + |\tilde{F}_x(\mathbf{r}_2)|^2 - |\tilde{F}_x(\mathbf{r}_1) - \tilde{F}_x(\mathbf{r}_2)|^2\\
&\quad = |\mathbf{r}_1|^2 + |\mathbf{r}_2|^2 - |\mathbf{r}_1 - \mathbf{r}_2|^2 = 2\sigma(\mathbf{r}_1,\mathbf{r}_2).
\end{aligned}$$

Finally, using (i) and (ii) it is easily shown that

$$\begin{aligned}
&|\tilde{F}_x(\alpha_1\mathbf{r}_1 + \alpha_2\mathbf{r}_2) - \alpha_1\tilde{F}_x(\mathbf{r}_1) - \alpha_2\tilde{F}_x(\mathbf{r}_2)|^2\\
&\quad = |(\alpha_1\mathbf{r}_1 + \alpha_2\mathbf{r}_2) - \alpha_1\mathbf{r}_1 - \alpha_2\mathbf{r}_2|^2 = 0,
\end{aligned}$$

which proves (iii).

Now, we are in the position to construct the extended isometries Γ_x. Let us first assume that the curve $\mathbf{r}$ does not entirely lie in a plane. Then, we can form a basis of $\mathbb{R}^3$ with three linearly independent vectors $\mathbf{w}_i \in \mathcal{W}$. Hence, for each $\mathbf{x} \in \mathbb{R}^3$ there exists a unique expansion $\mathbf{x} = \sum_{i=1}^{3}\alpha_i\mathbf{w}_i$, $\alpha_i \in \mathbb{R}$. For any such $\mathbf{x}$ we define

$$\Gamma_x(\mathbf{x}) := F_x(\mathbf{0}) + \sum_{i=1}^{3}\alpha_i\tilde{F}_x(\mathbf{w}_i).$$

Evidently, for the special case of $\mathbf{r} = \sum_{i=1}^{3}\gamma_i\mathbf{w}_i \in \mathcal{W}$,

$$\begin{aligned}
\Gamma_x(\mathbf{r}) &= F_x(\mathbf{0}) + \sum_{i=1}^{3}\gamma_i\tilde{F}_x(\mathbf{w}_i) = F_x(\mathbf{0}) + \tilde{F}_x\left(\sum_{i=1}^{3}\gamma_i\mathbf{w}_i\right)\\
&= F_x(\mathbf{0}) + \tilde{F}_x(\mathbf{r}) = F_x(\mathbf{r}),
\end{aligned}$$

due to property (iii) of $\tilde{F}_x$, such that indeed the restriction $\Gamma_x|_{\mathcal{W}} = F_x$. Now, using property (ii) of $\tilde{F}_x$, it is straightforward to show that for any $\mathbf{x}$ and $\mathbf{y} = \sum_{i=1}^{3}\beta_i\mathbf{w}_i \in \mathbb{R}^3$,

$$\begin{aligned}
|\Gamma_x(\mathbf{x}) - \Gamma_x(\mathbf{y})|^2 &= \left|\sum_{i=1}^{3}(\alpha_i - \beta_i)\tilde{F}_x(\mathbf{w}_i)\right|^2\\
&= \left|\sum_{i=1}^{3}(\alpha_i - \beta_i)\mathbf{w}_i\right|^2 = |\mathbf{x} - \mathbf{y}|^2,
\end{aligned}$$

which proves that Γ_x is an isometry of $\mathbb{R}^3$.

Finally, we address the special case of a planar curve. Then either $\mathcal{W}$ is a straight line, in which case there is nothing to prove, since this is a degenerate case of a helix. Otherwise, we pick two linearly independent vectors $\mathbf{w}_i \in \mathcal{W}$ and a third vector $\mathbf{k}_3$ perpendicular to $\mathbf{w}_1,\mathbf{w}_2$. Since F_x maps $\mathcal{W}$ to itself, it is clear that $\sigma(\tilde{F}_x(\mathbf{w}_i),\mathbf{k}_3) = 0$ as well. For any vector $\mathbf{x} \in \mathbb{R}^3$, a representation $\mathbf{x} = \alpha_1\mathbf{w}_1 + \alpha_2\mathbf{w}_2 + \alpha_3\mathbf{k}_3$ is possible and we define

$$\Gamma_x(\mathbf{x}) = F_x(\mathbf{0}) + \alpha_1\tilde{F}_x(\mathbf{w}_1) + \alpha_2\tilde{F}_x(\mathbf{w}_2) + \alpha_3\mathbf{k}_3,$$

which for $\mathbf{x} \in \mathcal{W}$ (implying $\alpha_3 = 0$) using (iii) again leads to $\Gamma_x|_{\mathcal{W}} = F_x$. Furthermore, using the orthogonality of $\mathbf{k}_3$ to $\mathbf{w}_i,\tilde{F}_x(\mathbf{w}_i)$ as well as (ii), it follows for any $\mathbf{y} = \sum_{i=1}^{2}\beta_i\mathbf{w}_i + \beta_3\mathbf{k}_3$ that

$$\begin{aligned}
|\Gamma_x(\mathbf{x}) - \Gamma_x(\mathbf{y})|^2 &= \left|\sum_{i=1}^{2}(\alpha_i - \beta_i)\tilde{F}_x(\mathbf{w}_i) + (\alpha_3 - \beta_3)\mathbf{k}_3\right|^2\\
&= \left|\sum_{i=1}^{2}(\alpha_i - \beta_i)\mathbf{w}_i + (\alpha_3 - \beta_3)\mathbf{k}_3\right|^2\\
&= |\mathbf{x} - \mathbf{y}|^2.
\end{aligned}$$

Therefore, for this case, too, one can construct an isometry Γ_x of $\mathbb{R}^3$ which extends F_x. Evidently, in both cases tuning $x \to 0$ one can continuously transform the Γ_x to $\Gamma_{x=0} = id_{\mathbb{R}^3}$, such that all Γ_x lie in $SE(3)$.

[1] H. Totsuji and J.-L. Barrat, Phys. Rev. Lett. **60**, 2484 (1988).
[2] G. Vernizzi, K. L. Kohlstedt, and M. Olvera de la Cruz, Soft Matter **5**, 736 (2009).
[3] G. E. Desobry and P. K. Kabir, Am. J. Phys. **41**, 1350 (1973).
[4] F. Dufey, Chem. Phys. **330**, 326 (2006).
[5] R. C. T. da Costa, Phys. Rev. A **23**, 1982 (1981).
[6] P. Exner and M. Fraas, Phys. Lett. A **369**, 393 (2007).
[7] J. Goldstone and R. L. Jaffe, Phys. Rev. B **45**, 14100 (1992).
[8] O. V. Kibis *et al.*, Electromagnetics **25**, 425 (2005).
[9] K. T. Law and D. E. Feldman, Phys. Rev. Lett. **101**, 096401 (2008).
[10] V. Y. Prinz *et al.*, Phys. E (Amsterdam) **6**, 828 (2000).
[11] O. G. Schmidt and K. Eberl, Nature (London) **410**, 168 (2001).
[12] M. Bhattacharya, Opt. Commun. **279**, 219 (2007).
[13] A. Okulov, Phys. Lett. A **376**, 650 (2012).
[14] I. Ricardez-Vargas and K. Volke-Sepúlveda, J. Opt. Soc. Am. B **27**, 948 (2010).
[15] E. Vetsch, D. Reitz, G. Sague, R. Schmidt, S. T. Dawkins, and A. Rauschenbeutel, Phys. Rev. Lett. **104**, 203603 (2010).

[16] E. Vetsch *et al.*, IEEE J. Quantum Electron. **18**, 1763 (2012).
[17] D. Reitz and A. Rauschenbeutel, Opt. Commun. **285**, 4705 (2012).
[18] W. Paul, Rev. Mod. Phys. **62**, 531 (1990).
[19] Ch. Schneider, M. Enderlein, T. Huber, and T. Schaetz, Nat. Photonics **4**, 772 (2010).
[20] P. Schmelcher, Europhys. Lett. **95**, 50005 (2011).
[21] The property of having either a closed or infinitely extended curve can be formalized in terms of the arc length: For any arc length s, $\mathbf{r}(s)$ must be well defined, i.e., a point of the space curve under consideration.
[22] A. R. Tarrida, *Affine Maps, Euclidean Motions and Quadrics* (Springer, London, 2011).

2.2.2 Many-body problem of charges on a closed helix I: *Equilibrium and linearized behaviour*

PHYSICAL REVIEW A **91**, 023409 (2015)

Degeneracy and inversion of band structure for Wigner crystals on a closed helix

A. V. Zampetaki,[1] J. Stockhofe,[1] and P. Schmelcher[1,2]

[1]*Zentrum für Optische Quantentechnologien, Universität Hamburg, Luruper Chaussee 149, 22761 Hamburg, Germany*
[2]*The Hamburg Centre for Ultrafast Imaging, Luruper Chaussee 149, 22761 Hamburg, Germany*

(Received 18 September 2014; published 10 February 2015)

Constraining long-range interacting particles to move on a curved manifold can drastically alter their effective interactions. As a prototype we explore the structure and vibrational dynamics of crystalline configurations formed on a closed helix. We show that the ground state undergoes a pitchfork bifurcation from a symmetric polygonic to a zigzag-like configuration with increasing radius of the helix. Remarkably, we find that, for a specific value of the helix radius, below the bifurcation point, the vibrational frequency spectrum collapses to a single frequency. This allows for an essentially independent small-amplitude motion of the individual particles and, consequently, localized excitations can propagate in time without significant spreading. Upon increasing the radius beyond the degeneracy point, the band structure is inverted, with the out-of-phase oscillation mode becoming lower in frequency than the mode corresponding to the center-of-mass motion.

DOI: 10.1103/PhysRevA.91.023409 PACS number(s): 37.10.Ty, 37.90.+j, 61.50.−f, 63.20.D−

Introduction. A key ingredient for the formation of complex systems out of fundamental building blocks such as atoms or ions is the two-body interaction potential. Depending on its short- or long-range character, the corresponding many-body systems show very diverse properties and structural features [1–4]. Generically, the strength of the two-body potential decreases with increasing distance between the interacting particles. This situation changes drastically if the particles are not allowed to explore complete space but are forced to move on a curved manifold while keeping their original interactions. Hence the particles can interact via the dynamically forbidden dimensions, while their motional degree of freedom is constrained to the manifold.

A prototype system of this character is the helix, having constant curvature and torsion. Indeed, several works [5–10] have demonstrated unique novel features arising with respect to the structural and dynamical properties of charged (or dipolar) particles on a helix. First, one encounters that long-range interacting particles effectively experience forces of oscillatory character on the helix. Consequently, stable bound-state configurations exist for equally charged, repulsively interacting particles and can even be tuned in number and strength [5,8]. The resulting potential landscape for more particles is topologically very complex, leading to configurations with increasingly distorted symmetries. In the same line it has been shown that a zero-temperature second-order liquid-gas transition occurs at a critical field for interacting dipoles [7], and cluster formation as well as crystallization are possible [10]. Rendering the helix locally inhomogeneous, the center of mass (c.m.) of the particles couples to their relative motions, allowing for dissociation of bound states or binding of particles out of the scattering continuum [9].

In view of the structural complexity of helical long-range-interacting many-particle systems the natural but intriguing question emerges of what is the dynamical response and, in particular, the vibrational structure of such systems. To address this question we explore the properties and dynamics of crystalline configurations formed by identical charged particles, so-called Wigner crystals [11], confined on a closed helix. We find that tuning the geometry induces a structural transition reminiscent of the transverse zigzag buckling in linear Wigner crystals [12]. Due to the one-dimensional (1D) constraint that restricts the allowed excitations, this transition is accompanied by an unconventional deformation of the corresponding dispersion relation: For finite systems, there is a regime of inverted dispersion, with the out-of-phase mode being lowest in frequency. Even more, the transition passes through a stage where the complete linearization spectrum is essentially degenerate, such that *any* low-amplitude mode is an eigenmode of the system. Notably, localized excitations do not transfer energy into the rest of the chain.

Toroidal helix. We consider a system of N identical charged particles of mass m_0 interacting via the repulsive Coulomb interaction and confined to move on a 1D toroidal helix [see Fig. 1(a)] parametrized as

$$\mathbf{r}(u) = \begin{pmatrix} [R + r\cos(u)]\cos(au) \\ [R + r\cos(u)]\sin(au) \\ r\sin(u) \end{pmatrix}, \quad u \in [0,2M\pi], \qquad (1)$$

with R being the major radius of the torus, r denoting the radius of the helix (minor radius of the torus), and h referring to the helix pitch. The parameter $a = \frac{1}{M}$ is the inverse number of windings $M = \frac{2\pi R}{h}$. The effective Coulomb potential resulting from the confinement reads

$$V(u_1,u_2,\dots u_N) = \frac{1}{2}\sum_{i,j=1,i\neq j}^{N} \frac{\lambda}{|\mathbf{r}(u_i) - \mathbf{r}(u_j)|},$$

with λ being the coupling constant.

We perform a scaling transformation [9], measuring distances in units of $2h/\pi$ and time in units of $\left(\frac{8m_0h^3}{\lambda\pi^3}\right)^{1/2}$. This results in λ and m_0 being set to 1 in the following, while the dimensionless helix pitch is set to $h = \pi/2$. Note that the c.m. degree of freedom is coupled to the relative coordinates $\Delta_i = u_{i+1} - u_i$ for $r \neq 0$ since the confining manifold is not a homogeneous helix [9]. For $r = 0$ the toroidal helix degenerates to a ring of radius R where c.m. separation holds. In this ring limit, there is a single stationary state; namely, the totally symmetric polygonic configuration. In contrast, the potential landscape of charged particles confined on helical

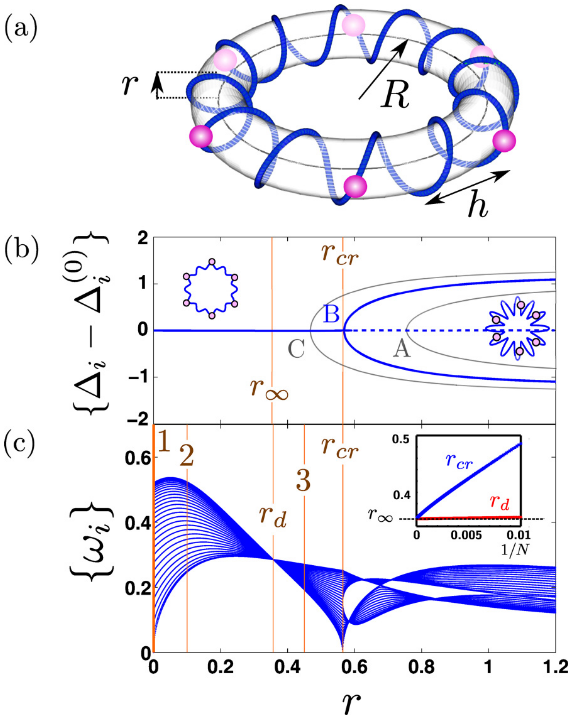

FIG. 1. (Color online) (a) Equidistant configuration of ions confined on the toroidal helix for $\nu = \frac{1}{2}$ and $N = 6$. (b) Equilibrium displacements of particles in stationary configurations as a function of helix radius r for filling $\nu = \frac{1}{2}$ and different numbers of particles: (A) $N = 30$, (B) $N = 60$, (C) $N = 120$. All values of $\Delta_i - \Delta_i^{(0)}$ are plotted on top of each other: For the polygonic configuration, all nearest-neighbor interparticle distances are identical, $\Delta_i = \Delta_i^{(0)}$ for all i, while in the zigzag-like configuration precisely two different distances are found; see the insets. The vertical lines indicate r_{cr} for $N = 60$ and the limiting value r_∞ of r_{cr} in the thermodynamic limit. (c) Linearization spectrum as a function of r of the stable solution (polygonic for $r < r_{\mathrm{cr}}$, zigzag-like for $r > r_{\mathrm{cr}}$) for $N = 60$. Degeneracy of all vibrational modes is observed at r_{d}. The inset depicts how r_{cr} and r_{d} converge to a common value r_∞ in the thermodynamic limit.

manifolds is very complex allowing for a large number of stationary states for given parameters [8,9].

Here, we focus on the low-energy crystalline configurations and their equilibrium properties for an even number of particles N which divides the number of windings M, i.e., $M = nN$ with $n = 1,2,\ldots$ and $\nu = 1/n \leqslant 1$ being the filling factor. Then, the polygonic configuration $u_j^{(0)} = 2(j-1)\pi n$ of the ring persists as a (stable or unstable) equilibrium configuration for all values of r with the charges being located equidistantly, $\Delta_j^{(0)} = 2\pi n$, at the outer circle of the toroidal helix [Fig. 1(a)]. However, for sufficiently large N (e.g., $N > 4$ for $\nu = \frac{1}{2}$) this configuration loses its stability at a finite $r = r_{\mathrm{cr}}$, undergoing a symmetry-breaking pitchfork bifurcation to a zigzag-like configuration [Fig. 1(b)] in which successive particles have alternatingly moved to positive and negative values of the z coordinate of the vector $\mathbf{r}$ [Eq. (1)]. For a fixed filling, here $\nu = \frac{1}{2}$, the bifurcation point r_{cr} shifts to lower values of r with increasing N (thus also increasing M), tending to a finite value r_∞ [Fig. 1(c), inset] in this thermodynamic limit, with a rather slow convergence rate. Surprisingly, it turns out that the value of r_∞ depends only on the helix pitch h; namely, $r_\infty = \frac{h}{\sqrt{2\pi}}$ in physical units (or $r_\infty = \frac{1}{2\sqrt{2}}$ in our dimensionless units), independently of ν.

Following the stable branch of solutions, we calculate the spectrum of vibrational modes in the harmonic approximation [Fig. 1(c)]. Intriguingly, in the regime $r < r_{\mathrm{cr}}$ (where the stable configuration is still symmetric) this spectrum exhibits a crossing point r_{d} where all modes are very close to degenerate. The value r_{d} also depends on the system size, decreasing for large N and tending to r_∞ in the thermodynamic limit [Fig. 1(c), inset], but much faster than r_{cr} does. Thus, for finite systems an interval $r_{\mathrm{d}} < r < r_{\mathrm{cr}}$ always exists. In this region the spectrum is inverted, and finally the lowest eigenvalue crosses zero at r_{cr}, rendering the symmetric configuration unstable and leading to the observed pitchfork bifurcation [Fig. 1(b)]. For $r > r_{\mathrm{cr}}$ two branches of frequencies separated by a gap are created, as a result of the new emergent solutions possessing a doubled unit cell.

Vibrational analysis. We now return to the frequency spectrum of the symmetric, polygonic configuration for $r < r_d$. This being a Wigner crystal with a one-particle unit cell, the corresponding dispersion relation consists of a single branch. For its evaluation, we introduce the arc length parametrization in which the kinetic energy and Euler–Lagrange equations assume the standard form [9]. The dispersion relation then reads

$$\omega^2(k) = \frac{1}{a^2(R+r)^2 + r^2}\sum_{l=1}^{N} H_{1,l}\exp[-ik(l-1)\Delta s], \quad (2)$$

with the Hessian at the equilibrium configuration $H_{i,j} = \frac{\partial^2 V}{\partial u_i \partial u_j}\big|_{\{u_j^{(0)}\}}$ (we can fix one index for symmetry reasons). The prefactor in Eq. (2) results from transforming to the arc length s, Δs denotes the arc length interparticle distance of the symmetric solution, and $k = \frac{2\pi m}{N\Delta s}$, $(m = 0, \pm 1, \ldots \pm \frac{N}{2})$ is the wave number of the corresponding excitation.

Results for $\omega(k)$ at different values of r are shown in Fig. 2. For $r = 0$ [Fig. 2(b)] the long-wavelength limit $k \to 0$, corresponding to identical displacements of all particles (c.m. mode [Fig. 2(a)]) has a vanishing frequency $\omega \to 0$, resulting from the c.m. decoupling in the ring geometry.

As the helix radius r increases, the spectrum at small k becomes smoother and a gap opens at $k = 0$ [Fig. 2(c)] due to the coupling of the c.m. to the relative motion for $r > 0$. This gap increases with increasing r, while the overall width of the spectrum decreases. At a critical point r_{d} [Fig. 2(d)] the spectrum is essentially flat as we have already seen in Fig. 1(c). A zoom at this point [Fig. 2(d), inset] reveals that the degeneracy is very close to, but not complete. To locate the near-degeneracy point r_{d} analytically, we go back to Eq. (2). Complete degeneracy would imply that all off-diagonal elements of the Hessian $H_{i,j}, i \neq j$, vanish (the diagonal elements are always identical by symmetry). Focusing on the nearest-neighbor contributions, we thus find an approximate analytical expression for r_{d} by demanding $H_{j,j+1}|_{r_{\mathrm{d}}} = 0$, which yields

$$r_d = aR\frac{\sqrt{3+\cos(2an\pi)}}{\sqrt{2} - a\sqrt{3+\cos(2an\pi)}}, \quad (3)$$

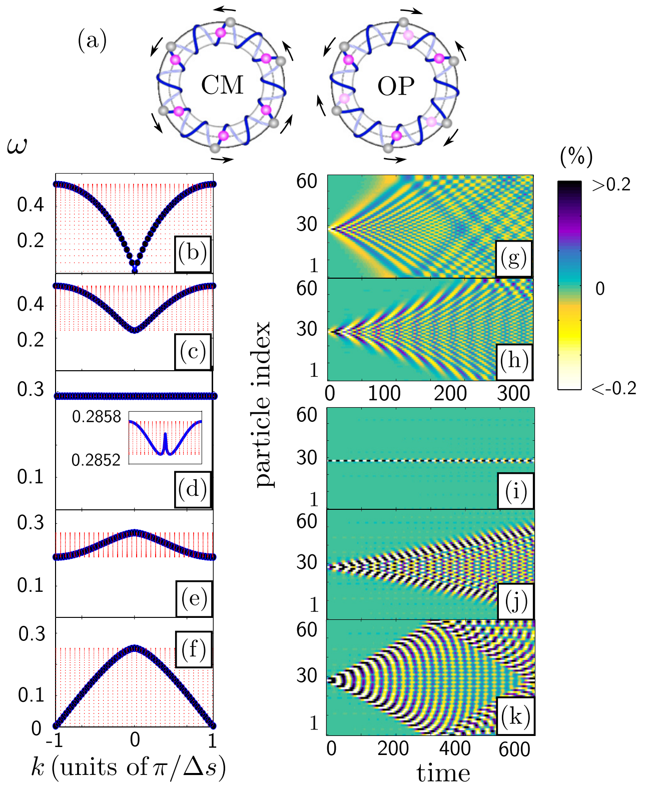

FIG. 2. (Color online) (a) Sketch of the center of mass (c.m., $k = 0$) and the out-of-phase (OP, $k = \pm\frac{\pi}{\Delta s}$) modes. (b)–(f) Dispersion relation curves $\omega(k)$ for $N = 60$ and increasing r corresponding to the points ($1,2,r_{\mathrm{d}},3,r_{\mathrm{cr}}$) marked in Fig. 1(c). For the same values of r, panels (g)–(k) present the time evolution following an initial displacement of the particle at $j_0 = 29$ by 1% of Δs. Colors encode the displacement from equilibrium in units of Δs.

in excellent agreement with the numerical findings. Indeed, in the thermodynamic limit $R \to \infty$, $a \to 0$, $aR = \frac{1}{4}$, r_{d} tends to $r_\infty = \frac{1}{2\sqrt{2}}$.

Beyond the crossing point, for $r > r_{\mathrm{d}}$, the curvature of the band changes sign permanently [Fig. 2(e)], implying that the OP mode [Fig. 2(a)] is now lower in frequency than the c.m. mode. The width of the spectrum increases again with increasing r until at $r = r_{\mathrm{cr}}$ the frequency of the OP mode at $k = \pm\pi/\Delta s$ reaches zero [Fig. 2(f)] and crosses to the imaginary axis for $r > r_{\mathrm{cr}}$, indicating the symmetric configuration becoming unstable due to the pitchfork bifurcation shown in Fig. 1(b). The condition $\omega(k = \pm\pi/\Delta s)|_{r_{\mathrm{cr}}} = 0$ can also be tackled analytically, giving an expression for r_{cr} which shows that it indeed tends to r_∞ in the thermodynamic limit.

The almost full degeneracy of the linearization spectrum at r_{d} implies a remarkable localization property in the small-amplitude dynamics, illustrated in Figs. 2(g)–2(k). Here we explore the time evolution following a displacement of a single particle at site j_0 by 1% of Δs. Generically, this initially localized excitation spreads over the whole crystal; see, e.g., Fig. 2(g) for the case of a ring. More precisely, a cone structure emerges indicating a finite velocity at which the excitation proliferates into the crystal. This cone becomes narrower with decreasing bandwidth of the spectrum, see Fig. 2(h), until at the point of near-degeneracy and thus near-zero bandwidth [Fig. 2(i)] the cone closes and the excitation no longer significantly spreads. This unique dynamical feature indicates the presence of an effective screening of interactions at $r = r_{\mathrm{d}}$, enabling essentially independent motion of the charged particles. We emphasize that, for this geometric configuration, *any* small initial excitation would maintain its shape for large times. Moving to larger radii $r > r_{\mathrm{d}}$, the degeneracy is lifted and the bandwidth of the spectrum increases again, thus reopening the cone [Figs. 2(j) and 2(k)].

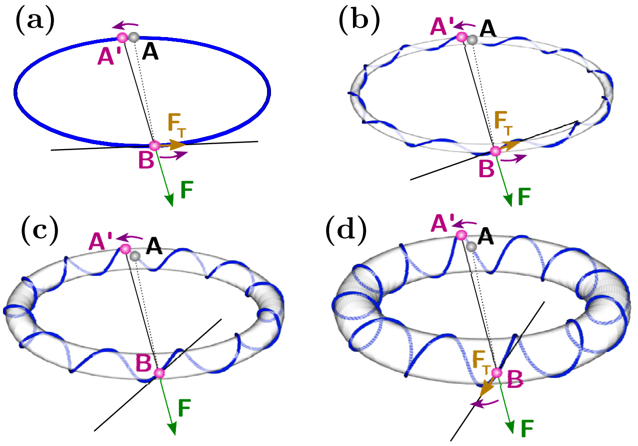

FIG. 3. (Color online) Schematic illustration of the response of a two-particle system A,B to a single-particle displacement AA' for the cases: (a) $r = 0$, (b) $r < r_{\mathrm{d}}$, (c) $r = r_{\mathrm{d}}$, and (d) $r > r_{\mathrm{d}}$. The total force F acting on particle B and its component F_T tangential to the toroidal helix are shown, whereas curved arrows indicate the directions of displacements.

Within the linearized equations, the initial dynamics of the spreading can be linked to $\omega(k)$ also on a formal level. The proliferation of the localized excitation can be quantified by the variance $S(t) = \sum_j j^2 e_j(t) - j_0^2$, where we employ the local energy $e_j(t)$ at site j as introduced in Ref. [13], with the time-independent normalization $\sum_j e_j = 1$. Then similar arguments as in Ref. [14] apply, leading to $S(t) \propto t^2 \int dk |\frac{d\omega}{dk}|^2$, assuming the crystal is large enough to approximate a sum over k with an integral over the first Brillouin zone. Consequently, the spreading of an initially localized excitation is ballistic, with a velocity determined by the square of the group velocity integrated over all k. If $\frac{d\omega}{dk}$ is close to zero globally, i.e., the dispersion is almost flat, $S(t)$ will grow only slowly with time and the excitation will spread only on very long timescales, which is what happens at r_{d}.

Degeneracy point. We now provide a geometrical interpretation for the emergence of the degeneracy point r_d in the spectrum. Let us examine the response of the simple $N = 2$ particle equilibrium configuration to a single-particle displacement (Fig. 3). A slight counterclockwise displacement of particle A towards the position A' results in a force acting on particle B. For the cases $r = 0$, $r < r_{\mathrm{d}}$ [Figs. 3(a) and 3(b)], this force possesses a component tangential to the confining manifold, causing a counterclockwise acceleration of particle B. At r_{d} [Fig. 3(c)], the geometry is such that the displacement AA' results in a force that has no component tangential to the toroidal helix curve at the equilibrium position of B and is therefore entirely compensated by the constraint. Thus, the small-amplitude motion of particle B is effectively decoupled from that of A. This simple geometric condition indeed leads to the same value of r_{d} as Eq. (3) for $N = 2$. For $r > r_{\mathrm{d}}$ the force acting on B again attains a nonvanishing projection onto the tangential but is now oriented in the opposite direction, causing a clockwise acceleration of particle B, in line with the observed inversion of the dispersion relations in this regime [Figs. 2(e) and 2(f)]. For $N > 2$, the geometry parameters can no longer be chosen such that all forces acting on the other particles after displacing a particular one are strictly compensated by the constraint. Still, it can be seen that the tangential projection of the force acting on particle j after particle i has been slightly displaced is proportional to the Hessian matrix element $H_{i,j}$. We have seen above that at r_{d} all these $H_{i,j} \approx 0$ for $i \neq j$. Thus, at the point of degeneracy, the geometry is such that if a single particle is displaced, all resulting force projections onto the local tangents where the other particles sit are very small simultaneously, resulting in the effective decoupling.

Conclusions. We have shown that, for charged particles confined on a 1D closed helix, a linear to zigzag-like bifurcation occurs when increasing the radius of the helix at commensurate fillings. Similar transitions are known for linear Wigner crystals under harmonic [15–20] or octupole trapping [21,22], where they are driven by the increment of dimensionality from one dimension to three dimensions controlled by the transverse trapping potential. In our case, however, the single-particle configuration space remains always strictly 1D, which manifests itself in the way in which the critical value r_{cr} is reached. In particular, for the transition to occur, the OP mode (ultimately causing the symmetry-breaking deformation of the crystal) has to cross zero at r_{cr}, in contrast to the ring limit $r = 0$ where the OP mode has the largest frequency. This necessarily implies an inversion of the dispersion relation when approaching r_{cr}, since the reduced dimensionality precludes a transverse branch which usually causes the bifurcation [17,18]. Notably, the deformation of the dispersion curve when increasing r towards r_{cr} passes through a point where all modes are essentially degenerate and the dispersion is flat. For this particular geometry, the (small-amplitude) dynamics of the particles is effectively decoupled, allowing for localized, nonspreading excitations.

The present setup offers unprecedented control over the vibrational band structure, suggesting its potential usefulness for applications in electronic nanodevices such as free-standing helix tubules [23–25]. The possibility of geometrically localizing excitations may be of interest for the design of acoustic meta-materials [26] and for applications in phononics such as sound isolation and cloaking [27] or even information storage [28]. Beyond this, helical structures are abundantly found in organic or inorganic molecules [29,30], and recent advances in optical trapping of ions [31] and helical trap design for neutral atoms [32–34] may pave the way for future experimental realizations with ultracold ions.

Acknowledgments. A.V.Z. thanks C. Morfonios and P. G. Kevrekidis for fruitful discussions and acknowledges support through a Ph.D. scholarship from the International Max Planck Research School for Ultrafast Imaging and Structural Dynamics (IMPRS-UFAST). J.S. gratefully acknowledges support from the *Studienstiftung des deutschen Volkes*.

---

[1] D. H. E. Dubin and T. M. O'Neil, Rev. Mod. Phys. **71**, 87 (1999).
[2] T. Lahaye, C. Menotti, L. Santos, M. Lewenstein, and T. Pfau, Rep. Prog. Phys. **72**, 126401 (2009).
[3] R. H. French *et al.*, Rev. Mod. Phys. **82**, 1887 (2010).
[4] M. Boninsegni and N. V. Prokof'ev, Rev. Mod. Phys. **84**, 759 (2012).
[5] O. V. Kibis, Phys. Lett. A **166**, 393 (1992).
[6] O. V. Kibis *et al.*, Electromagn. **25**, 425 (2005).
[7] K. T. Law and D. E. Feldman, Phys. Rev. Lett. **101**, 096401 (2008).
[8] P. Schmelcher, Europhys. Lett. **95**, 50005 (2011).
[9] A. V. Zampetaki, J. Stockhofe, S. Krönke, and P. Schmelcher, Phys. Rev. E **88**, 043202 (2013).
[10] J. K. Pedersen, D. V. Fedorov, A. S. Jensen, and N. T. Zinner, J. Phys. B: At., Mol. Opt. Phys. **47**, 165103 (2014).
[11] E. Wigner, Phys. Rev. **46**, 1002 (1934).
[12] R. C. Thomson, arXiv:1411.4945v1.
[13] P. B. Allen and J. Kelner, Am. J. Phys. **66**, 497 (1998).
[14] A. J. Martínez and M. I. Molina, J. Phys. A: Math. Theor. **45**, 275204 (2012).
[15] R. W. Hasse and J. P. Schiffer, Ann. Phys. (NY) **203**, 419 (1990).
[16] G. Birkl, S. Kassner, and H. Walther, Nature (London) **357**, 310 (1992).
[17] G. Piacente, I. V. Schweigert, J. J. Betouras, and F. M. Peeters, Phys. Rev. B **69**, 045324 (2004).
[18] S. Fishman, G. DeChiara, T. Calarco, and G. Morigi, Phys. Rev. B **77**, 064111 (2008).
[19] E. Shimshoni, G. Morigi, and S. Fishman, Phys. Rev. Lett. **106**, 010401 (2011).
[20] A. C. Mehta, C. J. Umrigar, J. S. Meyer, and H. U. Baranger, Phys. Rev. Lett. **110**, 246802 (2013).
[21] E. Yurtsever, E. D. Onal, and F. Calvo, Phys. Rev. A **83**, 053427 (2011).
[22] F. Cartarius, C. Cormick, and G. Morigi, Phys. Rev. A **87**, 013425 (2013).
[23] V. Y. Prinz *et al.*, Phys. E (Amsterdam, Neth.) **6**, 828 (2000).
[24] O. G. Schmidt and K. Eberl, Nature (London) **410**, 168 (2001).
[25] *Nanotubes and Nanofibers* edited by Y. Gogotsi (Taylor & Francis Group, LLC New York, 2006).
[26] P. A. Deymier, *Acoustic Metamaterials and Phononic Crystals*, Springer Series in Solid-State Sciences (Springer, Berlin, 2013).
[27] M. Maldovan, Nature (London) **503**, 209 (2013).
[28] T. J. G. Apollaro and F. Plastina, Open Sys. Info. Dyn. **14**, 41 (2007).
[29] A. A. Kornyshev, D. J. Lee, S. Leikin, and A. Wynveen, Rev. Mod. Phys. **79**, 943 (2007).

[30] Y. Wang, J. Xu, Y. Wang, and H. Chen, Chem. Soc. Rev. **42**, 2930 (2013).

[31] Ch. Schneider, M. Enderlein, T. Huber, and T. Schaetz, Nat. Photonics **4**, 772 (2010).

[32] A. Okulov, Phys. Lett. A **376**, 650 (2012).

[33] E. Vetsch, D. Reitz, G. Sagué, R. Schmidt, S. T. Dawkins, and A. Rauschenbeutel, Phys. Rev. Lett. **104**, 203603 (2010).

[34] D. Reitz and A. Rauschenbeutel, Opt. Commun. **285**, 4705 (2012).

2.2.3 Many-body problem of charges on a closed helix II: *Dynamics of nonlinear excitations*

PHYSICAL REVIEW E **92**, 042905 (2015)

Dynamics of nonlinear excitations of helically confined charges

A. V. Zampetaki,[1] J. Stockhofe,[1] and P. Schmelcher[1,2]
[1]*Zentrum für Optische Quantentechnologien, Universität Hamburg, Luruper Chaussee 149, 22761 Hamburg, Germany*
[2]*The Hamburg Centre for Ultrafast Imaging, Luruper Chaussee 149, 22761 Hamburg, Germany*

(Received 22 July 2015; published 2 October 2015)

We explore the long-time dynamics of a system of identical charged particles trapped on a closed helix. This system has recently been found to exhibit an unconventional deformation of the linear spectrum when tuning the helix radius. Here we show that the same geometrical parameter can affect significantly also the dynamical behavior of an initially broad excitation for long times. In particular, for small values of the radius, the excitation disperses into the whole crystal whereas within a specific narrow regime of larger radii the excitation self-focuses, assuming finally a localized form. Beyond this regime, the excitation defocuses and the dispersion gradually increases again. We analyze this geometrically controlled nonlinear behavior using an effective discrete nonlinear Schrödinger model, which allows us among others to identify a number of breatherlike excitations.

DOI: 10.1103/PhysRevE.92.042905 PACS number(s): 05.45.−a, 37.10.Ty, 37.90.+j, 45.90.+t

I. INTRODUCTION

Whereas the harmonic approximation of interactions provides valuable information about the stability and the propagation of small amplitude excitations in crystals formed by interacting particles, their real-time dynamics as well as their thermal and transport properties are typically subject to some degree of nonlinearity [1]. Among the most prominent manifestations of such a nonlinearity are the self-focusing or self-trapping [2–4] of initial wave packet excitations and the existence of nonspreading excitations such as breathers and kinks [5–7]. For discrete systems, a prototype equation incorporating these features is the so-called discrete nonlinear Schrödinger (DNLS) equation consisting of a linear (dispersive) coupling and a cubic nonlinear term [8], used to model plenty of systems ranging from coupled optical waveguides [9–11] and Bose-Einstein condensates [12–14] to transport in DNA molecules [15–17]. The standard spatial arrangement of sites in most of such one-dimensional (1D) studies is that of a straight equidistant chain in which the coupling (hopping) is restricted to nearest neighbors.

Nontrivial lattice geometries for 1D discrete nonlinear systems have also been studied and have been found to lead to intriguing new phenomena owing to the interplay between geometry and nonlinearity. In particular, in curved 1D lattices embedded in a 2D space the bending can act as a trap of excitations and induce a symmetry breaking of nontopological solitons [18]. For a 3D space, the helicoidal lattice structure, such as that of DNA molecules, is found to enhance the existence and stability of discrete breathers [19,20]. Furthermore, a curved geometry has been proven to induce nonlinearity in systems where the underlying interactions are harmonic [21,22].

In the present work we examine the interplay between nonlinearity and geometry in a system of identical charged particles, confined on a curved 1D manifold embedded in the 3D space, namely a closed (toroidal) helix. In a previous work [23], we have shown that in such a system, a tuning of the geometry controlled by the helix radius, leads to an unconventional deformation of the phononic band structure including a regime of strong degeneracy. As a consequence, the propagation of small amplitude localized excitations is affected significantly and a specific geometry exists at which the excitations remain localized up to long times. A natural question therefore arises as to what would be the long time dynamics of a general excitation and whether there is some geometrically controllable degree of nonlinearity inherent in the system, which can alter the propagation characteristics.

We provide an answer to this question by studying the time propagation of an initially broad excitation on the crystal of charges. We find that for values of the helix radius far from the degeneracy regime, the excitation initially spreads with multiple subsequent revivals due to the closed shape of the crystal. Within the degeneracy regime, however, the initial excitation focuses in the course of propagation reaching finally a rather localized state, serving as a hallmark of the existing nonlinearity. In order to quantify this nonlinearity we construct an effective DNLS model with additional nonlocal nonlinear terms [24,25]. Such a model is found to capture qualitatively well the localization and dispersion features of the original dynamics, providing a deeper insight into the observed effect. Even more, it gives us the opportunity to identify some discrete breatherlike excitations at the degenerate geometry, thus adding to the dynamical picture.

The structure of this work is as follows. In Sec. II we describe our system, commenting also on its linearized behavior. In Sec. III we present our results for the time evolution of an excitation in the crystal for different geometries. In Sec. IV we construct an effective DNLS model for our system at the geometries of interest and in Sec. V we use it to identify some breatherlike excitations. Finally, Sec. VI contains our conclusions.

II. SETUP AND LINEARIZATION

We consider a system of N identical charges of mass m_0, which interact via repulsive Coulomb interactions and are confined to move on a 1D toroidal helix, parametrized as

$$\mathbf{r}(u) = \begin{pmatrix} (R + r\cos(u))\cos(au) \\ (R + r\cos(u))\sin(au) \\ r\sin(u) \end{pmatrix}, \quad u \in [0,2M\pi]. \qquad (1)$$

In Eq. (1) R denotes the major radius of the torus [Fig. 1(a)], h is the helix pitch, and r the radius of the helix (minor

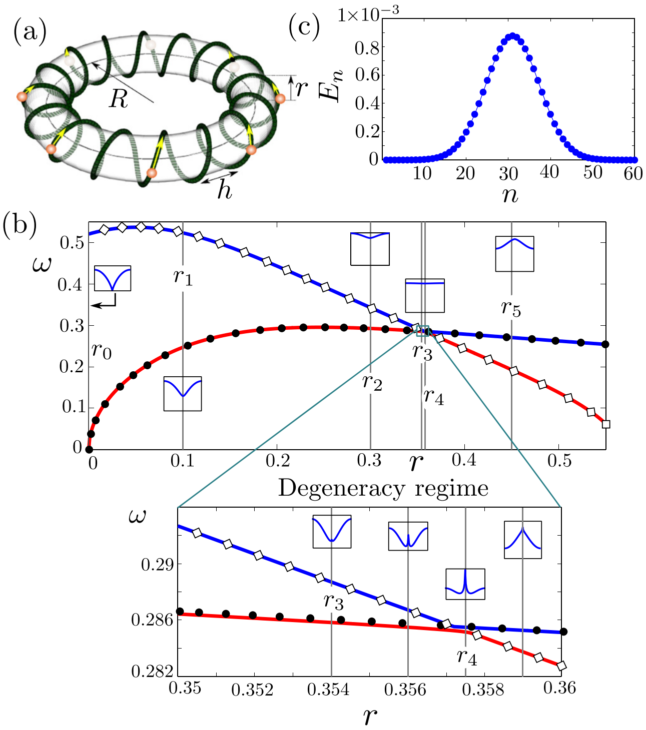

FIG. 1. (Color online) (a) Equidistant configuration of ions confined on the toroidal helix for $\nu = \frac{1}{2}$ and $N = 8$. The yellow arrows indicate the initial velocities of the particles. (b) Highest (solid blue line) and lowest (solid red line) frequencies of the linearization spectrum around the equilibrium equidistant configuration as a function of r for $N = 60$ particles. The black dots and the empty diamonds refer to the frequencies corresponding to the center of mass and the out of phase mode respectively. The vertical lines mark the radii of the helix we use in our calculations. The small insets depict the form of the respective vibrational band structures $\omega(k)$ at the corresponding values of r. (c) Initial local energy E_n profile as a function of the particle index n.

radius of the torus), whereas $a = \frac{1}{M}$ stands for the inverse number of windings $M = \frac{2\pi R}{h}$. The total effective interaction potential, which results from the constrained motion of the charges on the helical manifold, reads $V(u_1,u_2,\dots u_N) = \frac{1}{2}\sum_{i,j=1,i\neq j}^{N}\frac{\lambda}{|\mathbf{r}(u_i)-\mathbf{r}(u_j)|}$, where u_j denotes the coordinate of particle j and λ is the coupling constant characterizing the standard Coulomb interactions.

Then the Lagrangian of the system in terms of the u_i coordinates is given by

$$L(\{u_i,\dot{u}_i\}) = \frac{1}{2}m_0\sum_{i=1}^{2}|\partial_{u_i}\mathbf{r}(u_i)|^2\dot{u}_i^2 - \frac{1}{2}\sum_{i,j=1,i\neq j}^{N}\frac{\lambda}{|\mathbf{r}(u_i)-\mathbf{r}(u_j)|}, \qquad (2)$$

where $\mathbf{r}(u)$ refers to the parametrization of the toroidal helix given in Eq. (1). Note that the geometry of the constraint manifold enters the Lagrangian of Eq. (2) in both the interaction and the kinetic energy, due to the position-dependent factor $|\partial_{u_i}\mathbf{r}(u_i)|^2$. If desired, the latter factor can be removed by transforming to arc-length parametrization $s(u) = \int|\partial_u\mathbf{r}(u)|du$, resulting in the familiar second time derivative terms in the Euler-Lagrange equations of motion for the $s_i(t) = s[u_i(t)]$ [26], at the cost, however, of losing the explicit analytical form for the interaction energy.

We choose dimensionless units by scaling all our physical quantities (e.g., position x, time t, and energy E) with λ, m_0, and $2h/\pi$ as follows:

$$\tilde{x} = \frac{x\pi}{2h}, \quad \tilde{t} = t\sqrt{\frac{\lambda\pi^3}{8m_0h^3}}, \quad \tilde{E} = \frac{2Eh}{\lambda\pi}, \quad \tilde{m}_0 = 1, \quad \tilde{\lambda} = 1,$$

omitting in the following the tilde for simplicity.

At commensurate fillings, i.e., $M = nN$, $n = 1,2,\dots$ with the filling factor being $\nu = 1/n \leqslant 1$, it is found that for values of the helix radius r up to a critical point r_c the ground-state configuration of such a system is the equidistant polygonic configuration $u_j^{(0)} = 2(j-1)\pi n$ [Fig. 1(a)]. This configuration loses its stability at r_c undergoing a zigzag bifurcation [23].

We focus in this work on the dynamical behavior of charged particles confined on the toroidal helix in the region $r < r_c$, where the ground state is still the polygonic one. We have shown in Ref. [23] that in such a region the linear spectrum of the system changes dramatically with tuning the radius of the helix r, a fact that crucially affects the propagation of small amplitude localized excitations. Specifically, it was found that the width of the linear spectrum decreases as one approaches a point r_d of strong degeneracy from below and increases again beyond that point, while interchanging the character between the eigenmodes corresponding to the highest and the lowest frequencies [Fig. 1(b)]. In fact, since the degeneracy is not complete, it is better to refer to a degeneracy regime within which the inversion of the spectrum is gradually achieved while its width remains small [Fig. 1(b) (inset)]. We consider in this work six different geometries, each corresponding to a different value of r, covering all the regions with a qualitatively different linear spectrum [Fig. 1(b)] from the ring limit ($r_0 = 0$) to the degeneracy (r_3,r_4) and the inversion (r_5) regime. We focus on the case of half filling $\nu = \frac{1}{2}$ for $N = 60$ particles.

III. TIME PROPAGATION OF A GAUSSIAN EXCITATION

In this section we present and discuss the dynamical response of our system to an initial excitation. Although the physical results are in principle independent of the exact character of this excitation and the means used for its quantification, the determination of both is essential for the illustration and the theoretical description of our findings.

Dealing with classical systems and seeking an excitation measure whose total amount is conserved in time, the natural choice is a (to be defined) energy distribution associated with each particle, referred to hereafter as local energy E_n. Whereas the kinetic energy K consists of parts allocated to each individual particle, the potential energy cannot be uniquely partitioned, yielding different definitions of local energy [27–29]. Aiming for them to be strictly positive for all possible excitations (a considerably nontrivial requirement for systems with Coulomb interactions), we define our local energies E_n in a rather unconventional way, focusing on a

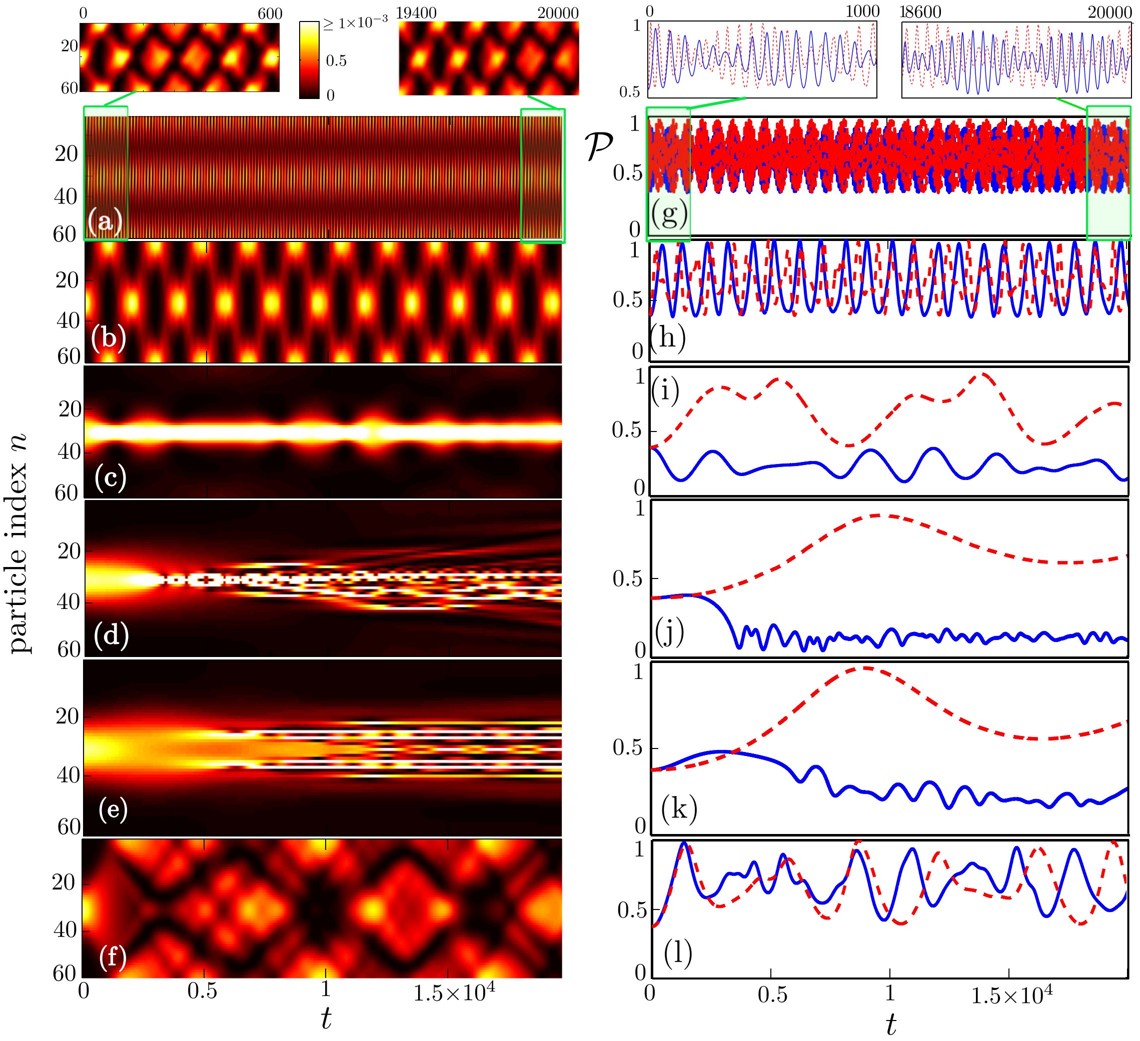

FIG. 2. (Color online) (a)–(f) Time evolution of the initial Gaussian excitation presented in Fig. 1(c) for $N = 60$, $\nu = 1/2$ for increasing r corresponding to the points (a) r_0, (b) r_1, (c) r_2, (d) r_3, (e) r_4, and (f) r_5 marked in Fig. 1(b). Colors encode the values of local energy E_n for each particle n and time t. For the same values of r panels (g)–(l) depict the time evolution of the normalized participation ratio $\mathcal{P}$ of the excitation. The solid blue lines are the results from our numerical simulations corresponding to (a)–(f), whereas the dashed red lines correspond to the results for a harmonic approximation of the potential.

positive decomposition of the harmonic interaction term [29]. Our complete definition and a more detailed discussion of local energies are provided in the Appendix.

We start with an initially broad excitation of a Gaussian profile in terms of local energies [Fig. 1(c)]. Since the local energies E_n depend trivially on the particles' velocities (contrary to what is the case for the particles' positions), the most straightforward way to obtain such a Gaussian local energy profile is by exciting the particles with a suitable velocity distribution. Of course, for a given local energy profile the magnitude of such a velocity distribution can be uniquely determined, but there is a freedom in the direction of the velocity for each particle. We choose here all the velocities to point in the positive direction [Fig. 1(a)].

The ensuing dynamics is shown in Figs. 2(a)–2(f). Obviously, the time evolution of the Gaussian excitation possesses a drastic dependence on the geometry, controlled by the helix radius r. In particular, for $r < r_d$ [Figs. 2(a), 2(b)] the excitation spreads into the whole crystal and refocuses almost periodically at the time instants when the left and the right propagating parts of the excitation meet and superimpose at the diametrically opposite point of the closed helix. As discussed in Ref. [23] the spreading velocity decreases as r is increased, following the width of the linear spectrum [Fig. 1(b)]. As the width becomes smaller the features of the time evolution alter significantly. Already at the point r_2 the excitation does not spread any more into the crystal, but it alternately focuses and again defocuses to its initial shape [Fig. 2(c)]. Even more surprisingly, within the degeneracy region [Figs. 2(d), 2(e)] the initial excitation undergoes a focusing after some time scale t_F [$t_F \approx 4000$ for Fig. 2(d), $t_F \approx 6000$ for Fig. 2(e)]. Subsequently, the wave packet loses its smooth envelope and fragments into a number of highly localized excitations. Depending on r, the routes towards such a localized state can be different, with the wave packet evolving initially one central peak [Fig. 2(d)] or two side peaks [Fig. 2(e)]. Another interesting feature within the degeneracy regime is that the reflection symmetry of the initial excitation profile can break in the course of propagation, attaining after some time a significantly asymmetric form [Fig. 2(d)]. The direction of the asymmetry depends on the direction of the initial velocities of the particles. Beyond the degeneracy [Fig. 2(f)] the spreading of the excitation into the crystal reappears with a periodic refocusing but the propagation pattern is much different owing to the inverted form of the vibrational band structure.

In order to quantify the degree of focusing or localization of the excitation, we examine the time dependence of the normalized participation ratio

$$\mathcal{P} = \frac{1}{N}\frac{\left(\sum_{n=1}^{N} E_n\right)^2}{\sum_{n=1}^{N} E_n^2}. \tag{3}$$

Evidently, this quantity can take values between $1/N$ and 1, with $\mathcal{P} = 1$ signifying the case of a completely extended excitation where the energy is equipartitioned between all the particles and $\mathcal{P} = 1/N$ marking the opposite case of a fully localized excitation in a single particle. Note that the local energies E_n in (3) should be non-negative for the definition to make sense.

Our results, presented in Figs. 2(g)–2(l), support our discussion above. Especially the focusing of the excitation after t_F is evident in Figs. 2(j)–2(k). However, the subsequent drop in $\mathcal{P}$ is much stronger in Fig. 2(j) than in Fig. 2(k), in line with the observation that at $r = r_3$ the final localized state consists of less excited particles [Fig. 2(d)] than at $r = r_4$ [Fig. 2(e)].

In Ref. [23] it was demonstrated that a small localized initial excitation does not spread significantly for short times at the degeneracy point, in contrast to the behavior for other geometries. This fact was understood solely by an inspection of the linearization spectrum. Here, however, the situation is different. Not only the complete absence of spreading, but especially the existence of self-focusing calls for an account of the underlying nonlinearity. This is further emphasized and supported by Figs. 2(g)–2(l) where the results of the propagation within the harmonic approximation of the potential are also displayed. As long as the total amplitude of the initial excitation is small enough, the harmonic approximation works well. As the amplitude is increased this approximation will start to fail, and nonlinear effects are expected to show up. The results of the present work suggest that except for the amplitude, also the geometry allows to control the importance of the nonlinearity. Specifically, for the given amplitude and for geometries far from the degeneracy regime [Figs. 2(g), 2(h), 2(l)] the harmonic approximation qualitatively reproduces the exact time evolution of the participation ratio, although, as should be expected, there are quantitative deviations. In contrast, close to and within the degeneracy regime the harmonic approximation fails completely, predicting a spreading and an extended form of the excitation, instead of localization. This makes it clear that regarding the focusing, we indeed encounter a nonlinear phenomenon.

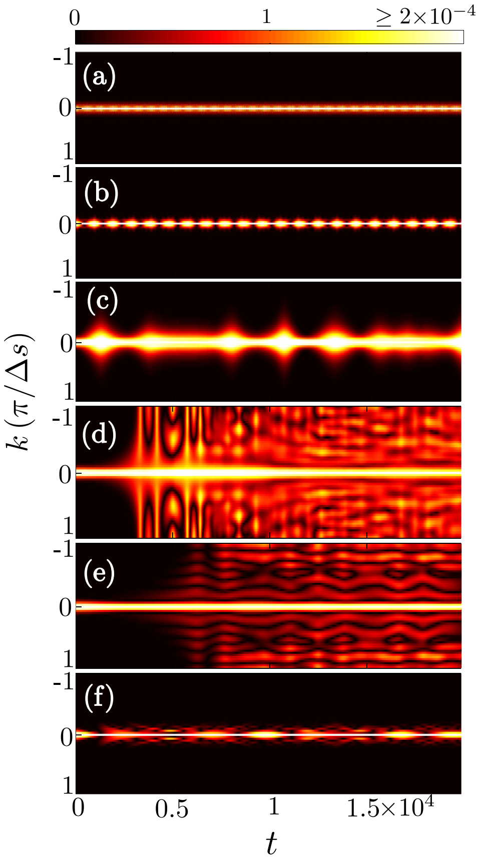

FIG. 3. (Color online) Absolute value of the discrete Fourier transform of the local energy excitation profile as a function of time and wave number k. (a)–(f) correspond to increasing r, ranging from r_0 to r_5 as indicated in Fig. 1(b).

Complementary information about the spreading or localization of the Gaussian excitation can be obtained from its time evolution in the reciprocal space, i.e.. in terms of the wave numbers $k \in [-\frac{\pi}{\Delta s}, \frac{\pi}{\Delta s}]$, where Δs denotes the arc length interparticle distance of the equidistant ground-state configuration. To this extent, we examine how the discrete Fourier transform of the local energy profile evolves in the reciprocal space [Figs. 3(a)–3(f)]. The initial excitation, being overall extended in the coordinate space [Fig. 1(c)], appears to be rather localized around the wave vector $k = 0$ in the k space. It remains localized as expected for $r < r_d$ [Figs. 3(a), 3(b)], but when approaching r_d more wave vectors in the vicinity of $k = 0$ become excited [Fig. 3(c)]. At the degenerate geometries [Figs. 3(d), 3(e)] the excitation expands rapidly in the reciprocal space, populating after the characteristic time t_F almost all the wave numbers k. The space localized solution consists therefore of most of the k modes, with the population of the initial $k = 0$ mode being dominant. At $r > r_d$ [Fig. 3(f)] the excitation remains, as for small r, in the narrow vicinity of the $k = 0$ mode.

Before proceeding with our study of the nonlinear behavior, let us note that for the results presented here we have used a rather small initial excitation with a total energy of the order of 1% of the ground-state energy per particle E_{GS}/N. For larger amplitudes the self-focusing can occur also for smaller radii, i.e., at a greater distance from the degeneracy region.

IV. EFFECTIVE NONLINEAR MODEL

The dynamics analyzed in the previous section is characterized by a self-focusing process of excitations for the case of degenerate geometries and therefore suggests a prominent role of the nonlinearity. We aim in this section to identify and quantify the leading nonlinear terms as well as to derive a DNLS effective model in the region of degeneracy. As a result we will, among others, gain insight into the excitation amplitudes and the time scale t_F for localization.

A. Dominant nonlinear terms

Since the initial excitation is small enough we attempt to identify the dominant anharmonic terms by expanding the potential around the equilibrium configuration $\{u^{(0)}\}$ up to fourth order. It is advantageous to do so in the arc length parametrization s so that the final Euler-Lagrange equations of motion and particularly the kinetic terms would assume the standard form [26]. To this purpose we calculate the matrices

$$H_{ij} = \left.\frac{\partial^2 V}{\partial s_i \partial s_j}\right|_{\{s^{(0)}\}}, \quad G_{ij} = \left.\frac{\partial^3 V}{\partial s_i^2 \partial s_j}\right|_{\{s^{(0)}\}} \tag{4}$$

corresponding to the Hessian and the matrix of the third derivatives respectively. Terms involving more than two different positions are equal to zero, since the total potential V is a sum of exclusively two-body potential terms.

For the fourth derivative terms we define two further matrices as

$$M_{ij} = \left.\frac{\partial^4 V}{\partial s_i^2 \partial s_j^2}\right|_{\{s^{(0)}\}}, \quad Q_{ij} = \left.\frac{\partial^4 V}{\partial s_i^3 \partial s_j}\right|_{\{s^{(0)}\}} \tag{5}$$

for $i \neq j$ and

$$M_{ii} = Q_{ii} = \frac{1}{2}\left.\frac{\partial^4 V}{\partial s_i^4}\right|_{\{s^{(0)}\}},$$

separating the derivatives of the same order in s_i, s_j from those with a different order and splitting the diagonal derivative terms (involving differentiation with respect to a single position) in two. The calculation of the above derivatives in the arc length parametrization can be carried out by using the respective derivatives in the u coordinate space as well as the known relations for derivatives of inverse functions. Under these considerations and denoting $s_j - s_j^{(0)} = x_j$ the potential reads

$$\begin{aligned} V \approx E_{GS} &+ \frac{1}{2}\sum_{i,j=1}^{N} x_i H_{ij} x_j + \frac{1}{6}\sum_{i,j=1}^{N} x_i^2 G_{ij} x_j \\ &+ \frac{1}{24}\sum_{i,j=1}^{N} x_i^2 M_{ij} x_j^2 + \frac{1}{24}\sum_{i,j=1}^{N} x_i^3 Q_{ij} x_j \end{aligned} \tag{6}$$

leading to the equations of motion

$$\begin{aligned} \ddot{x}_n = &-\sum_{j\neq n} H_{nj} x_j - H_{nn} x_n - \frac{1}{3}\sum_{j\neq n} x_n G_{nj} x_j \\ &- \frac{1}{6}\sum_{j\neq n} G_{jn} x_j^2 - \frac{1}{6}\sum_{j\neq n} x_n M_{nj} x_j^2 - \frac{1}{3} M_{nn} x_n^3 \\ &- \frac{1}{8}\sum_{j\neq n} x_n^2 Q_{nj} x_j - \frac{1}{24}\sum_{j\neq n} Q_{jn} x_j^3, \end{aligned} \tag{7}$$

which consist of harmonic, quadratic, and third-order nonlinear terms. All the matrices appearing in these equations are symmetric except for the matrix G_{ij}, relating to the quadratic force terms, which is fully antisymmetric. This can affect significantly the symmetry of the expected solutions. If the quadratic nonlinear force terms are ignored then the equations of motion (7) possess the symmetry $x_n \to -x_n$ which also results in symmetric excitations keeping their symmetry in the course of propagation. The quadratic force terms, however, break the reflection symmetry and allow for an asymmetric evolution of initially symmetric excitations as the one observed in Fig. 2(d).

Let us mention at this point that in the ring limit $r = r_0 = 0$, where a separation of the center of mass holds, the matrices involved in Eq. (7) are not independent but obey the relations

$$H_{nn} = -\sum_{j\neq n} H_{nj}, M_{nn} = -\frac{1}{8}\sum_{j\neq n} Q_{nj}, M_{nj} = -\frac{3}{4} Q_{nj}$$

yielding

$$\begin{aligned} \ddot{x}_n = &-\sum_{j\neq n} H_{nj}(x_j - x_n) - \frac{1}{6}\sum_{j\neq n} G_{jn}(x_j - x_n)^2 \\ &- \frac{1}{24}\sum_{j\neq n} Q_{nj}(x_j - x_n)^3, \end{aligned} \tag{8}$$

which for only nearest-neighbor (NN) couplings leads to a Fermi-Pasta-Ulam kind of equations of motion [30], with both quadratic and cubic nonlinear interactions.

Before proceeding, we note that the matrix elements $H_{ij}, G_{ij}, M_{ij}, Q_{ij}$ depend, due to the symmetry of the ground-state configuration, only on the index difference $m = i - j$. Therefore, when referring to these elements in the following we will use the notation H_m, G_m, M_m, Q_m.

B. DNLS model

The effect of localization of the initial wave packet occurs, as we have observed in Sec. III, in the regime close to degeneracy. There, the diagonal terms of the Hessian provide the dominant contribution to the linear spectrum as the off-diagonal ones are very small. Since $|H_0| \gg 2|H_1|$ [Fig. 4(a)], one can use in that regime the so-called rotating wave approximation (RWA) [31], assuming that the position coordinate can be described as

$$x_n(t) = \Psi_n(t)e^{-i\omega_0 t} + \Psi_n^*(t)e^{i\omega_0 t}, \tag{9}$$

with $\Psi_n(t)$ a slowly varying amplitude and $\omega_0^2 = H_0$ yielding a fast oscillating phase $e^{\pm i\omega_0 t}$. Apart from the requirement of a weak dispersion, a condition for a sufficiently weak nonlinearity has also to be satisfied [31], namely $|H_0| \gg \frac{1}{3}|M_0| \max[x_i(0)]^2$ with $\max[x_i(0)]$ the maximum initial displacement (or respectively momentum) of a single particle. This criterion is satisfied as well in our case, since the initial conditions we have used lead to $|H_0|$ of about 100 times larger than $\frac{1}{3}|M_0| \max[x_i(0)]^2$.

Using the ansatz (9) and making the assumption $|\frac{d\Psi_n}{dt}| \ll \omega_0|\Psi_n|$, as well as neglecting the rapidly oscillating terms with

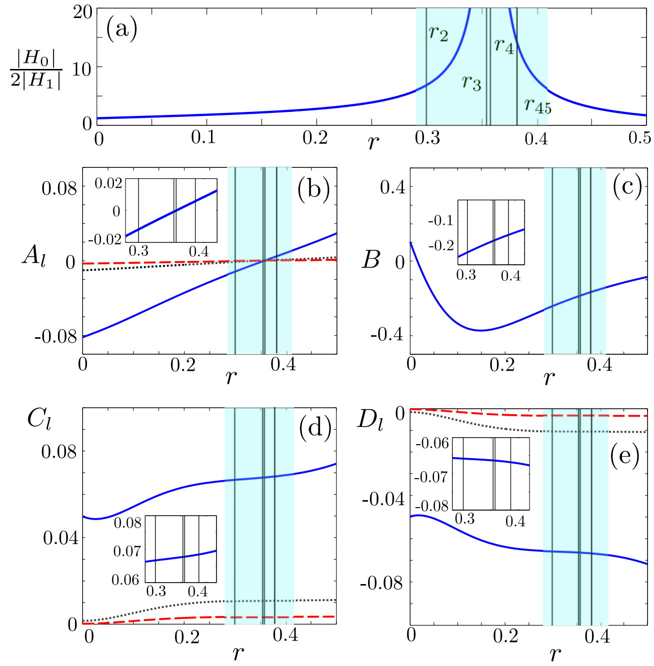

FIG. 4. (Color online) (a) The ratio between the diagonal and off diagonal elements of the Hessian $\frac{|H_0|}{2|H_1|}$ as a function of r. (b)–(e) Coefficients A_l, B, C_l, D_l defined in Eq. (11) as a function of r. The solid blue lines depict the coefficient values for $l = 1$, whereas the black doted lines for $l = 2$ and the red dashed ones for $l = 3$. The cyan (shaded) area marks the region of applicability of the RWA as derived from (a). The vertical lines correspond to the values of r we study with the DNLS model. Note that three of them namely r_2, r_3 and r_4 are the same as those studied in the previous section [Fig. 1(b)] whereas r_{45} lies between r_4 and r_5. The insets provide a zoom into the region of interest.

frequency $3\omega_0$, the equations of motion (7) acquire the form

$$\begin{aligned} i\dot{\Psi}_n = & \sum_{l=1}^{N/2} A_l(\Psi_{n-l} + \Psi_{n+l}) + B|\Psi_n|^2\Psi_n \\ & + \sum_{l=1}^{N/2} C_l\big[2\Psi_n(|\Psi_{n-l}|^2 + |\Psi_{n+l}|^2) + \Psi_n^*\big(\Psi_{n-l}^2 + \Psi_{n+l}^2\big)\big] \\ & + \sum_{l=1}^{N/2} D_l[2|\Psi_n|^2(\Psi_{n-l} + \Psi_{n+l}) + \Psi_n^2(\Psi_{n-l}^* + \Psi_{n+l}^*) \\ & + |\Psi_{n-l}|^2\Psi_{n-l} + |\Psi_{n+l}|^2\Psi_{n+l}] \\ & + \sum_{l=1}^{N/2} F_l\big[\big(2\Psi_n(\Psi_{n+l} - \Psi_{n-l}) - \Psi_{n+l}^2 + \Psi_{n-l}^2\big)e^{-i\omega_0 t} \\ & + (2\Psi_n(\Psi_{n+l}^* - \Psi_{n-l}^*) - |\Psi_{n+l}|^2 + |\Psi_{n-l}|^2)e^{i\omega_0 t}\big] \end{aligned} \tag{10}$$

with

$$\begin{aligned} A_l &= \frac{H_l}{2\omega_0}, \quad B = \frac{M_0}{2\omega_0}, \quad C_l = \frac{M_l}{12\omega_0} \\ D_l &= \frac{Q_l}{16\omega_0}, \quad F_l = \frac{G_l}{12\omega_0}. \end{aligned} \tag{11}$$

The last term in Eq. (10) comes from the quadratic nonlinear force term, which is responsible for generating second harmonics and breaking the reflection symmetry of the equations. Within the RWA this term is also neglected due to its fast oscillation in time in comparison to the other slowly varying terms. Of course such an approximation limits our consideration to the general focusing/defocusing behavior of the wave-packet excitation, not accounting for secondary propagation features such as the exact shape of the excitation pulse during the time evolution.

The actual numerical values of the remaining coefficients A_l, B, C_l, D_l for our system are shown in Figs. 4(b)–4(e) as a function of r. All the coefficients in the region of validity of our approximation have a definite sign except for A_l, which changes sign within the degeneracy regime. It is also obvious that an increasing index l leads to coefficients closer and closer to zero, with even the coefficients of $l = 2$ being already very small. Since the major contribution stems from $l = 1$, we can proceed performing a NN approximation, which yields

$$\begin{aligned} i\dot{\Psi}_n = & A(\Psi_{n-1} + \Psi_{n+1}) + B|\Psi_n|^2\Psi_n \\ & + C\big[2\Psi_n(|\Psi_{n-1}|^2 + |\Psi_{n+1}|^2) + \Psi_n^*\big(\Psi_{n-1}^2 + \Psi_{n+1}^2\big)\big] \\ & + D\big[2|\Psi_n|^2(\Psi_{n-1} + \Psi_{n+1}) + \Psi_n^2(\Psi_{n-1}^* + \Psi_{n+1}^*) \\ & + |\Psi_{n-1}|^2\Psi_{n-1} + |\Psi_{n+1}|^2\Psi_{n+1}\big], \end{aligned} \tag{12}$$

where we have omitted the index 1 from the coefficients for clarity. Equation (12) can be recognized as a DNLS equation with additional nonlinear couplings studied in the literature [24,25] and will be the point of reference in the following discussion.

In order to check the validity of our approximation we propagate the Gaussian excitation illustrated in Fig. 1(c) according to Eq. (12). Note that the quantity Ψ is by definition complex, with its real part at $t = 0$ relating to the displacement $\mathrm{Re}(\Psi_n(0)) = \frac{x_n(0)}{2}$ [Eq. (9)] and its imaginary part to the momentum $\mathrm{Im}(\Psi_n(0)) = \frac{p_n(0)}{2\omega_0}$ [Eq. (9) within the RWA], both in the arc length parametrization. Furthermore, the local energy $E_n = \frac{1}{2}(\omega_0^2 x_n^2 + p_n^2)$ can be expressed as $E_n = 2\omega_0^2|\Psi_n|^2$, the conservation of the total energy being thus linked directly with the conservation of $\sum_n |\Psi_n|^2$. A comparison between Figs. 5(a)–5(c) and Figs. 2(c)–2(e) makes it clear that the NN DNLS model captures qualitatively very well the features of the exact excitation propagation, exhibiting focusing and defocusing at r_2 [Fig. 5(a)] and localization after a certain time for r within the degeneracy region [Figs. 5(b), 5(c)]. Beyond the point r_4, but still very close to the degeneracy [Fig. 4(a)], the excitation, although keeping its shape for a long time, eventually disperses into the whole crystal [Fig. 5(d)]. Note that the profile of the excitation remains reflection symmetric (with respect to the central particle) in the course of propagation for all geometries [Figs. 5(a)–5(d)], in contrast to what is observed in Fig. 2(d), which we attribute primarily to the neglected quadratic nonlinear term.

Most of these results can already be inferred from an inspection of Eq. (12) and the parameter $A(r)$ as shown in Fig. 4(b). When increasing the radius, A changes its sign from negative (same sign as B) to positive. Correspondingly, with increasing r the effective nonlinearity changes from attractive (hopping A and nonlinearity B of the same sign), leading to

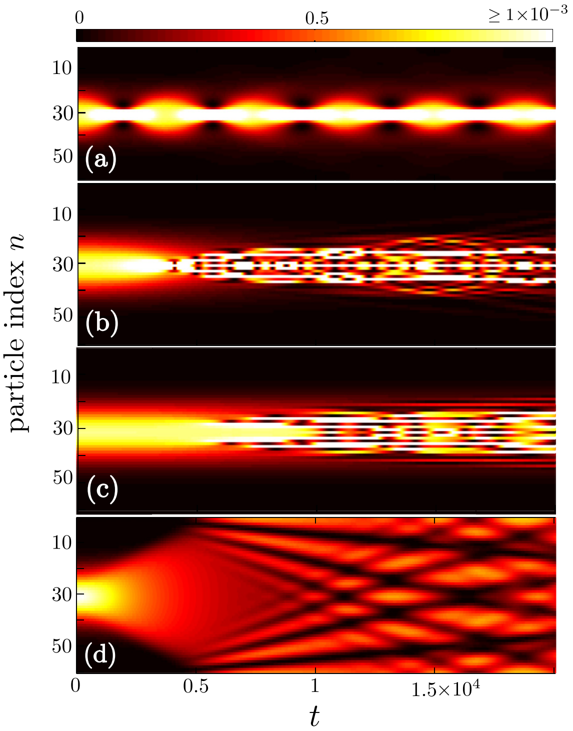

FIG. 5. (Color online) (a)–(d) Time propagation of the initial Gaussian excitation of Fig. 1(c) under the DNLS equation (12) for increasing r corresponding to the points (a) r_2, (b) r_3, (c) r_4, and (d) r_{45} marked in Fig. 4(a). Colors encode the values of local energy $E_n = 2\omega_0^2|\Psi_n|^2$ for each particle n and time t.

self-focusing dynamics [Figs. 5(a)–5(c)], to repulsive (hopping A and nonlinearity B of opposite sign), leading to defocusing [Fig. 5(d)].

The change of the magnitude of the parameter A affects also the degree and the time scale of the wave-packet localization. A small hopping term is expected to slow down the dynamical behavior of the system since it accounts for reduced mobility. A decrease in its magnitude leads also to an enhancement of the general nonlinear behavior since it shifts the weight of the dynamics to the nonlinear terms. On a more formal level, these statements can be justified within a multiple scale analysis [32].

In fact, one can arrive at the RWA by assuming that all the terms of Eq. (7) are much smaller than the $H_{nn}x_n$ term. Introducing the small parameter $\epsilon = |A|$, due to the weak coupling and weak nonlinearity conditions a slow time scale can be defined $\tilde{t} = \epsilon t = |A|t$, which is characteristic for the time evolution of Ψ_n. A further rescaling of Ψ_n with $\sqrt{|\frac{B}{A}|}$ leads to the standard form of our DNLS [24,25] with $\tilde{A} = \text{sgn(A)}$, $\tilde{B} = \text{sgn}(\frac{\text{B}}{\text{A}})$, $\tilde{C} = \frac{C}{B}$, $\tilde{D} = \frac{D}{B}$ and $\tilde{\Psi}_n = \sqrt{|\frac{B}{A}|}\Psi_n$ in which the strength of the nonlinearity is primarily controlled by the amplitude of the initial excitation $\tilde{\Psi}_n(0)$. In the degeneracy regime, due to the factor $\sqrt{|\frac{B}{A}|}$, this is about one order of magnitude larger than its value for other parameter values of r resulting in the observed strong localization of the excitation. In the same regime the time scale of the time evolution becomes very large, scaling as $\frac{1}{|A|}$ and yielding in our case a characteristic time t_F of the order of 10^3.

The simple picture above of the DNLS within the NN approximation gradually fails in the limit $|A| \to 0$, and the dispersion coefficients A_l from all the neighbors have to be incorporated into Eq. (12). This can be seen, for instance, from the intricate nonmonotonic features in the linear dispersion of the full model there [Fig. 1(b) (inset) below and close to r_4], which are not predicted by the NN DNLS model. Notably, however, even at r_4 our results within the NN DNLS model [Fig. 5(c)] capture satisfactorily the dynamics of the full system [Fig. 2(e)]. This can be attributed to the nonlinear coupling terms (C,D), which become stronger than the linear one (A) within this narrow parameter region and dominate the dispersion. As a last remark, we note that for long times the weak nonlinearity condition may also start to fail (if substantial amplitude has localized on a single site), such that the existence of higher harmonics becomes more prominent, which may lead to effects such as breaking of the parity symmetry.

V. BREATHERLIKE EXCITATIONS

Having constructed an effective DNLS model we can finally pose the question of the existence of breatherlike solutions in our system in the regime of degeneracy. If the coefficients C,D of Eq. (12) were zero, our system could be described within the so-called anticontinuum limit of weakly coupled oscillators, since the linear coupling is already very small. In this limit, it has been proven that discrete breather solutions exist if there is a substantial degree of anharmonicity and no resonances with the linear spectrum [33]. In our case with $C,D \neq 0$ one can still search for breathers provided, as well, that their frequency does not belong to the phonon spectrum [24]. To this end the frequency in the ansatz of Eq. (9) should be changed from ω_0 to $\omega < \omega_0$ out of the phonon band, i.e.,

$$x_n(t) = \Psi_n(t)e^{-i\omega t} + \Psi_n^*(t)e^{i\omega t}. \tag{13}$$

Repeating the steps of the previous section assuming that still the RWA holds, we arrive at Eq. (14) with an additional local term $\Lambda\Psi_n$

$$\begin{aligned} i\dot{\Psi}_n &= A'(\Psi_{n-1} + \Psi_{n+1}) + \Lambda\Psi_n + B'|\Psi_n|^2\Psi_n \\ &\quad + C'\big[2\Psi_n(|\Psi_{n-1}|^2 + |\Psi_{n+1}|^2) + \Psi_n^*\big(\Psi_{n-1}^2 + \Psi_{n+1}^2\big)\big] \\ &\quad + D'\big[2|\Psi_n|^2(\Psi_{n-1} + \Psi_{n+1}) + \Psi_n^2(\Psi_{n-1}^* + \Psi_{n+1}^*) \\ &\quad + |\Psi_{n-1}|^2\Psi_{n-1} + |\Psi_{n+1}|^2\Psi_{n+1}\big], \end{aligned} \tag{14}$$

where $\Lambda = (\omega_0^2 - \omega^2)/2\omega$, $A' = A\frac{\omega_0}{\omega}$, $B' = B\frac{\omega_0}{\omega}$, $C' = C\frac{\omega_0}{\omega}$ and $D' = D\frac{\omega_0}{\omega}$. In the anticontinuum limit $A',C',D' = 0$ this equation can be easily checked to have the solutions $\Psi_n \in \{0, \sqrt{\frac{\Lambda}{B}}e^{i\phi_n}\}$ with arbitrary phases $\phi_n \in \mathbb{R}$. Simple real breather solutions can thus be constructed iteratively as strings of the elements 0 and $\pm\sqrt{\frac{\Lambda}{B}}$. Starting from such a breather solution and following the solution trajectories in the parameter space A',C',D' with a Newton method [24,34] we can find possible breather solutions for different values of r corresponding to the geometries of interest. The natural step then is to transform back to the x_n, p_n coordinates and use these as an initial

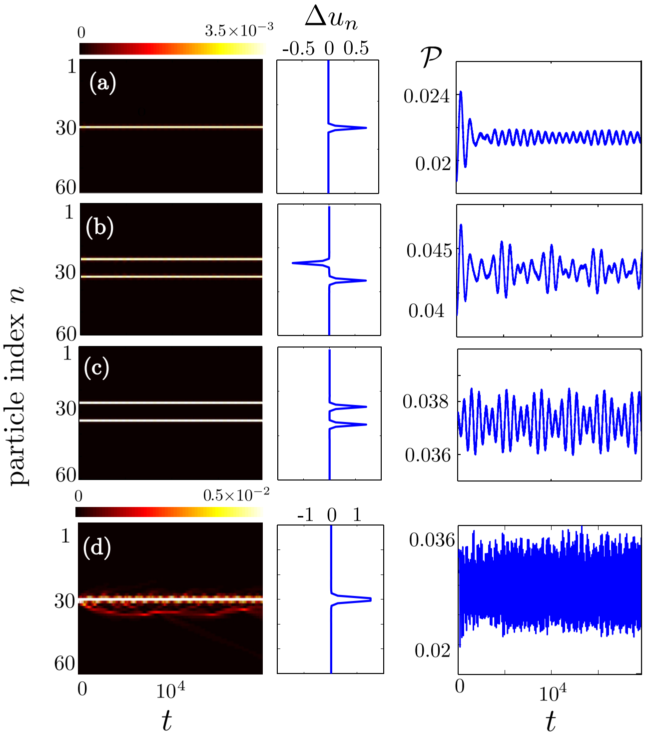

FIG. 6. (Color online) (a)–(d) Time propagation of breatherlike excitations in the degeneracy regime, at $r = r_3$ in (a), (b), (d), and $r = r_4$ in (c). The color plots of the first column depict the values of the local energy E_n whereas the second column provides the initial profiles of the excitation in position coordinates, i.e., $\Delta u_n = u_n - u_n^{(0)}$ as a function of the particle index n. The third column illustrates the time evolution of the participation ratio $\mathcal{P}$ for the degenerate geometries and the initial conditions of (a)–(d). In (a)–(d) the initial excitation comes only from the displacement Δu_n of particles from their equilibrium.

excitation in our system, simulating their time evolution within the full model equations as done in Sec. III. In this way, we aim to further substantiate the link between the effective DNLS equation and the full charges-on-a-helix model governed by the Lagrangian of Eq. (2), demonstrating that the prominent localized excitations of the DNLS also preserve their character in the full model.

Our results are presented in Fig. 6 for different initial conditions at the degenerate geometries. Evidently, many of them [Figs. 6(a)–6(c)] keep their solitonic character in the presence of the full Coulomb interactions, a fact that can be justified also by inspecting the time evolution of the participation ratio. Indeed, the local energy profile of the excitations changes negligibly with oscillating potential and kinetic energy parts, mapping to oscillating displacements Δu_n and momenta p_n. These breatherlike excitations include a single-particle excitation [Fig. 6(a)] as well as two-particle excitations with both opposite [Fig. 6(b)] and equal displacements [Fig. 6(c)].

Surprisingly enough, we have observed that the excited particles should always be separated by a distance [Figs. 6(b), 6(c)] for the solitonic character to persist, otherwise, if neighboring particles are excited there is always a small dispersion and a part of the excitation that focuses on a single particle, acquiring finally a rather asymmetric profile [Fig. 6(d)]. This picture is also valid within the DNLS framework where such solutions are found to undergo a spontaneous symmetry breaking in the course of propagation.

VI. SUMMARY AND CONCLUSIONS

We have shown that a system of charged particles confined on a toroidal helix can react in qualitatively different ways when exposed to an initial excitation, depending on the geometric properties of the confining manifold. In particular, while dispersion is the major feature of the dynamics for very small helix radii r, the excitation self-focuses and localizes for values of r in the so-called degeneracy regime, where the linear coupling is very small. Beyond this regime, the time evolution of the excitation is characterized by a defocusing, which is gradually dominated again by dispersion. Especially the self-focusing of the excitation observed for the degenerate geometries constitutes a hallmark of the existing nonlinearity in the system. Interestingly enough, the nonlinear part of the interactions (both local and nonlocal) does not approach zero in this regime, nor does it undergo a change in sign with increasing r, contrary to the behavior of the respective linear part. It is primarily this contrast between the robustness of the nonlinearity and the variability of the linear part, which induces the variety of dynamics in the system, allowing for its control through the tuning of the underlying geometry.

Furthermore, we have identified the character of the leading nonlinear terms and constructed an effective discrete nonlinear Schrödinger model with additional nonlinear couplings, which has allowed us to predict and interpret the different responses of the helical chain to its excitation. Through this model it has also been possible to identify some special breatherlike excitations in our system which propagate in time keeping their shape. Overall, we emphasize that the present setup offers many possibilities for the implementation of various nonlinear models ranging from the Fermi-Pasta-Ulam to different discrete nonlinear Schrödinger models with both attractive and repulsive nonlinearities only by the tuning of a single geometrical parameter, i.e., the radius r of the helix.

Regarding its possible experimental realization, it relies on the challenging task of constructing a helical trap for charged particles. Although such a construction might not be straightforward, there have been certain advances towards this direction in different contexts, such as the realization of freestanding helical nanostructures [35–37] and the design of helical traps for neutral atoms [38,39]. Moreover, our results could be of relevance in studies of energy and excitation transfer in helical molecules, such as DNA. Finally, macroscopic realizations of our system could also be possible by using for example charged beads as done for the study of polymers [40,41].

ACKNOWLEDGMENTS

A.Z. thanks the International Max Planck Research School for Ultrafast Imaging and Structural Dynamics for support in the form of a scholarship. J.S. gratefully acknowledges support from the Studienstiftung des deutschen Volkes.

APPENDIX: DEFINITION OF LOCAL ENERGIES

As briefly mentioned in Sec. III the definition of local energies E_n in a system of interacting particles is not unique. For a general potential $V = \frac{1}{2}\sum_{i,j,i\neq j}^{N} W(u_i,u_j)$ the most common partition consists in equally distributing each part of the potential energy among the particles involved

$$E_n = \frac{1}{2}\sum_{i,i\neq n}^{N} W(u_i,u_n) + K_n - E_n^{(0)}, \tag{A1}$$

with $E_n^{(0)} = \frac{1}{2}\sum_{i,i\neq n}^{N} W(u_i^{(0)},u_n^{(0)})$ the local energy of the equilibrium configuration $\{u_i^{(0)}\}$ and K_n the kinetic energy of the particle n. Although such a definition is very useful in describing systems with nearest-neighbor interactions such as oscillator chains [27,28], it can lead to problems concerning the description of long-range interacting systems and particularly those involving Coulomb interactions, as the one we consider in this paper. The major problem is that it generally leads to both positive and negative values of E_n and thus demands a handling of both positive and negative excitations. Negative local energies should be avoided if we wish to interpret the local energy as the amount or probability of the corresponding particle being excited and proceed in defining quantities such as the participation ratio $\mathcal{P}$ of Eq. (3).

Let us demonstrate this fact with a simple example of a Coulomb system consisting of three identical charges moving on a ring [Fig. 7(a)]. The equilibrium configuration of such as system is the equidistant one with the charges sitting in the corners of an equilateral triangle with a side of length y. Evidently then $E_n^{(0)} = \frac{1}{y}, n = 1,2,3$. If particle 1 is clockwise displaced from equilibrium up to the point 1′ the resulting local excitation energies would be

$$E_1 = \frac{1}{2y_+} + \frac{1}{2y_-} - \frac{1}{y}, \quad E_2 = \frac{1}{2y_-} - \frac{1}{2y},$$
$$E_3 = \frac{1}{2y_+} - \frac{1}{2y},$$

where $y_+ > y > y_-$. Obviously $E_1, E_2 > 0$, whereas $E_3 < 0$, demonstrating that following this definition the local energy can become negative. Another minor disadvantage of this definition of local energy for long-range interacting particles is that it is highly nonlocal, meaning that if a single particle is displaced from equilibrium, the local energies of other particles even those far apart will acquire a finite value.

A way to fix this last issue is to construct the local energy E_n so that it contains: all the parts of the potential depending solely on u_n, none of the parts that are independent of u_n, and half of the terms involving both u_n and any other u_i. This can be written in a compact form

$$E_n = \frac{1}{2}\sum_{i,i\neq n}^{N}\left[W(u_n,u_i) + W\left(u_n,u_i^{(0)}\right)\right]$$
$$-\frac{1}{2}\sum_{i,i\neq n}^{N}\left[W\left(u_n^{(0)},u_i\right) + W\left(u_n^{(0)},u_i^{(0)}\right)\right] + K_n, \tag{A2}$$

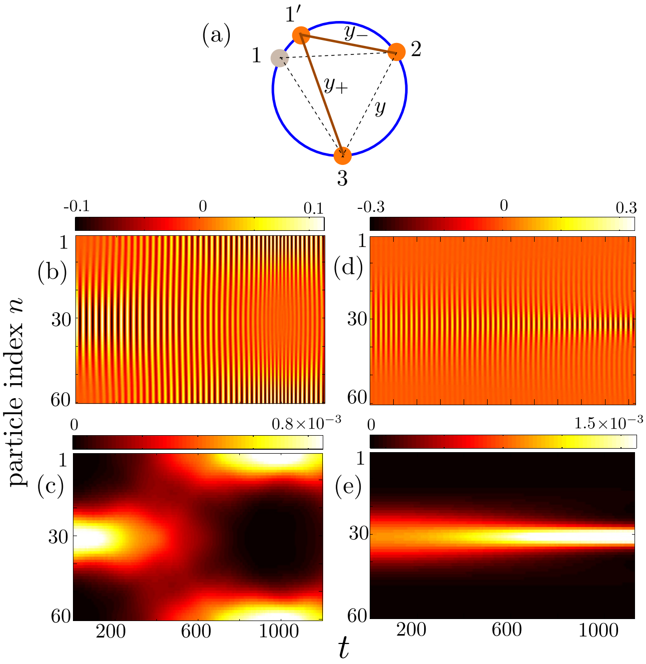

FIG. 7. (Color online) (a) A schematic illustration of three charges on a ring at equilibrium (1, 2, 3) and after particle 1 has been displaced (1′, 2, 3). The dashed lines denote the Euclidean distances in equilibrium, whereas the solid ones, the distances after the displacement. (b), (c) The time evolution of a Gaussian excitation for $r = r_1$. (d), (e) The time evolution of a Gaussian excitation for $r = r_2$. The colors in (b), (d) encode the values of the displacement from equilibrium x_n whereas in (c), (e) the values of the local energies E_n defined in Eq. (A5). (b)–(e) show simulation results for $N = 60$ particles and $\nu = 1/2$.

which can be checked to sum up to the total excitation energy, i.e., $\sum_{n=1}^{N} E_n = E$. Such a definition solves the problem of nonlocality since it distributes all single-particle potential terms to the corresponding particles, yielding for example $E_n = 0$ for $u_n = u_n^{(0)}$ and $K_n = 0$. It can also be checked to solve the problem of negativity in many cases, such as the one of the above three-particle example. There are however still special cases in which negative local energies can be encountered, where the negativity originates from the harmonic part of the total potential contained in each E_n

$$V_n^{(2)} = \frac{1}{2}\left.\frac{\partial^2 V}{\partial u_n^2}\right|_{(0)}\left(u_n - u_n^{(0)}\right)^2$$
$$+\frac{1}{2}\sum_{i,i\neq n}^{N}\left.\frac{\partial^2 V}{\partial u_n \partial u_i}\right|_{(0)}\left(u_n - u_n^{(0)}\right)\left(u_i - u_i^{(0)}\right), \tag{A3}$$

which can assume negative values at a given n. To fix this, one can make use of the overall stability of the equilibrium, which leads to the existence of a different decomposition of the harmonic contributions to the potential into purely positive parts in the form [29]

$$\tilde{V}_n^{(2)} = \frac{1}{2}\left[\sum_{j=1}^{N}\Omega_{nj}\left(u_j - u_j^{(0)}\right)\right]^2, \tag{A4}$$

where Ω denotes the square root of the Hessian. We thus adjust our definition (A2) by subtracting $V_n^{(2)}$ and adding instead $\tilde{V}_n^{(2)}$, i.e.,

$$\begin{aligned} E_n = &\frac{1}{2}\sum_{i,i\neq n}^{N}\left[W(u_n,u_i) + W\left(u_n,u_i^{(0)}\right)\right] \\ &-\frac{1}{2}\sum_{i,i\neq n}^{N}\left[W\left(u_n^{(0)},u_i\right) + W\left(u_n^{(0)},u_i^{(0)}\right)\right] \\ &+ K_n - V_n^{(2)} + \tilde{V}_n^{(2)}. \end{aligned} \tag{A5}$$

This definition provides a sufficiently local (although not entirely, due to the term $\tilde{V}_n^{(2)}$), positive decomposition of the excitation energy, which still satisfies $\sum_{n=1}^{N} E_n = E$. Its use can be further justified by comparing the time evolution of E_n with the time evolution of the displacement of the particle n from equilibrium $x_n = s_n - s_n^{(0)}$. A comparison of Figs. 7(b), 7(d) with 7(c), 7(e) respectively, leads to the conclusion that the time evolution of E_n captures nicely all the features of the propagating excitation such as the focusing and the spreading and only filters out the fast oscillations in Figs. 7(b), 7(d) caused by the fast continuous conversion of potential to kinetic energy and vice versa.

---

[1] A. C. Scott, *Nonlinear Science* (Oxford University Press, Oxford, 1999).

[2] S. A. Akhmanov, A. P. Aukhorukov, and R. V. Khokhlov, Sov. Phys. Usp. **10**, 609 (1968).

[3] J. C. Eilbeck, P. S. Lomdahl, and A. C. Scott, Physica D **16**, 318 (1985).

[4] M. Johansson, M. Hörnquist, and R. Riklund, Phys. Rev. B **52**, 231 (1995).

[5] A. J. Sievers and S. Takeno, Phys. Rev. Lett. **61**, 970 (1988).

[6] M. Remoissenet, *Waves Called Solitons: Concepts and Experiments* (Springer-Verlag, Berlin, 1999).

[7] D. K. Campbell, S. Flach, and Yu S. Kivshar, Phys. Today **57**, 43 (2004).

[8] P. G. Kevrekidis, *The Discrete Nonlinear Schrödinger Equation* (Springer-Verlag, Heidelberg, 2009).

[9] D. N. Christodoulides and R. I. Joseph, Opt. Lett. **13**, 794 (1988).

[10] R. Morandotti, U. Peschel, J. S. Aitchison, H. S. Eisenberg, and Y. Silberberg, Phys. Rev. Lett. **83**, 4756 (1999).

[11] A. A. Sukhorukov, Yu S. Kivshar, H. S. Eisenberg, and Y. Silberberg, IEEE J. Quantum Electro. **39**, 31 (2003).

[12] A. Trombettoni and A. Smerzi, Phys. Rev. Lett. **86**, 2353 (2001).

[13] F. Kh. Abdullaev, B. B. Baizakov, S. A. Darmanyan, V. V. Konotop, and M. Salerno, Phys. Rev. A **64**, 043606 (2001).

[14] H. Hennig, J. Dorignac, and D. K. Campbell, Phys. Rev. A **82**, 053604 (2010).

[15] S. F. Mingaleev *et al.*, J. Biol. Phys. **25**, 41 (1999).

[16] M. Peyrard, Nonlinearity **17**, R1 (2004).

[17] A. Dang Koko *et al.*, Chaos **22**, 043110 (2012).

[18] Yu B. Gaididei, S. F. Mingaleev, and P. L. Christiansen, Phys. Rev. E **62**, 53(R) (2000).

[19] J. F. R. Archilla, P. L. Christiansen, and Yu B. Gaididei, Phys. Rev. E **65**, 016609 (2001).

[20] B. Sánchez-Rey, J. F. R. Archilla, F. Palmero, and F. R. Romero, Phys. Rev. E **66**, 017601 (2002).

[21] P. G. Kevrekidis, S. V. Dmitriev, S. Takeno, A. R. Bishop, and E. C. Aifantis, Phys. Rev. E **70**, 066627 (2004).

[22] S. Takeno, S. V. Dmitriev, P. G. Kevrekidis, and A. R. Bishop, Phys. Rev. B **71**, 014304 (2005).

[23] A. V. Zampetaki, J. Stockhofe, and P. Schmelcher, Phys. Rev. A **91**, 023409 (2015).

[24] M. Öster, M. Johansson and A. Eriksson, Phys. Rev. E **67**, 056606 (2003).

[25] M. Öster and M. Johansson, Phys. Rev. E **71**, 025601(R) (2005).

[26] A. V. Zampetaki, J. Stockhofe, S. Krönke, and P. Schmelcher, Phys. Rev. E **88**, 043202 (2013).

[27] A. Sarmiento, R. Reigada, A. H. Romero, and K. Lindenberg, Phys. Rev E **60**, 5317 (1999).

[28] D. Hennig, S. Fugmann, L. Schimansky-Geier, and P. Hänggi, Phys. Rev E **76**, 041110 (2007).

[29] P. B. Allen and J. Kelner, Am. J. Phys. **66**, 497 (1998).

[30] E. Fermi, J. Pasta, and S. Ulam, Los Alamos, Report No. LA-1940 (1955); G. P. Berman and F. M. Izrailev, Chaos **15**, 015104 (2005).

[31] Yu. S. Kivshar and M. Peyrard, Phys. Rev. A **46**, 3198 (1992).

[32] C. M. Bender and S. A. Orszag, *Advanced Mathematical Methods for Scientists and Engineers* (McGraw-Hill, New York, 1978).

[33] R. S. MacKay and S. Aubry, Nonlinearity **7**, 1623 (1994).

[34] J. L. Marín and S. Aubry, Nonlinearity **9**, 1501 (1996).

[35] V. Y. Prinz *et al.*, Physica E **6**, 828 (2000).

[36] O. G. Schmidt and K. Eberl, Nature (London) **410**, 168 (2001).

[37] *Nanotubes and Nanofibers* edited by Y. Gogotsi (Taylor & Francis, New York, 2006).

[38] E. Vetsch, D. Reitz, G. Sagué, R. Schmidt, S. T. Dawkins, and A. Rauschenbeutel, Phys. Rev. Lett. **104**, 203603 (2010).

[39] D. Reitz and A. Rauschenbeutel, Opt. Comm. **285**, 4705 (2012).

[40] M. Reches, P. W. Snyder, and G. M. Whitesides, Proc. Nat. Acad. Sci. USA **106**, 17644 (2009).

[41] S. Tricard *et al.*, Phys. Chem. Chem. Phys. **14**, 9041 (2012).

Chapter 3

Conclusions and outlook

In this cumulative dissertation we have explored the equilibrium properties and dynamics of 1D Coulomb systems, focusing on the case of charged particles confined in helical geometries [O2–O4]. In all the cases, the reduced dimensionality and the long-range character of the underlying interactions provide us with a strongly correlated system. Our trapping manifolds include a finite line segment, an inhomogeneous helix and a toroidal helix, each one allowing for an exhibition of different effects.

Concerning the trapping of a large number of charges in a finite line segment (1D box), we have identified a crystalline to a cluster phase crossover driven by the increment of temperature. In the crystal phase, our findings bare similarities with those obtained for a finite ion chain under a harmonic trapping [81–83], including an inhomogeneity of the crystalline structure and a non-extensivity of the thermodynamic functions. The estimation of this deviation from extensivity allows us to make a finite prediction of the transition temperature in the thermodynamic limit. Interestingly enough, the main features of the phenomenology attached to this problem, are expected to be valid for every classical interacting system which supports a single equilibrium state at zero temperature. An appealing question would then be, how this phenomenology would change for systems which support multiple equilibrium configurations of different energy, as those encountered for helically confined charges.

The confinement of repulsively interacting charges on helical geometries affects significantly their behaviour, starting from their two-body interaction potential, which becomes oscillatory, allowing for a plethora of bound states, whose number is tuned by the geometrical parameters of the trap. If the helical trap is inhomogeneous the center-of-mass motion couples to the relative one permitting an energy transfer between these degrees of freedom. For a localized inhomogeneity, this energy transfer can cause a dissociation of an initially bound pair of particles through scattering. Due to the time reversal symmetry of the equations of motion, it is equally possible that two separate particles develop a bond through scattering. An analysis of the phase space of the two-body problem allows for identifying regimes of bound motion and escape. A more detailed investigation of the phase space, complemented by a search for stable and unstable periodic orbits is expected to provide a rigorous analysis of the interesting escaping procedure. Moreover, the study of the many-body analogue of the system, could reveal further interesting dynamical features, associated with an energy exchange between multiple degrees of freedom.

A different aspect of the many-body physics of helically confined charges was studied throughout this thesis by assuming a confinement on a toroidal helix. At commensurate fillings and for small values of the helix radius, the ground state of such a system is an equidistant configuration, similar to that found for a ring geometry. Beyond a critical value of the radius this loses its stability and bifurcates to a zigzag configuration. Below the transition, the reduced dimensionality of the system allows only for a single longitudinal branch of phononic excitations. This deforms continuously with the radius increment, opening a gap and passing through stages of degeneracy and inversion. Remarkably, at the degenerate geometry the interactions between the particles are effectively screened to a linear approximation, allowing for an essentially independent small-amplitude motion. Thus, a localized excitation can evolve in time almost without transferring energy to the rest of the chain up to long times.

The variability of the linear spectrum with the helix radius for charges confined in a closed helix has motivated a study of the system's response in the nonlinear regime. We have observed that many different dynamical behaviours can be encountered for different geometries, mapping to various nonlinear models. In the ring-limit the leading terms of the resulting equations of motion are of the Fermi-Pasta-Ulam type [240] involving long-range couplings. At the degenerate geometry the time evolution of the excitation can be at best described by a discrete nonlinear Schrödinger equation of the focusing type whereas beyond this geometry, at the regime of inversion, it is characterized by defocusing. This provides an explanation of the observed focusing of excitations within the region of degeneracy and allows for an identification of breather-like excitations in the system, which propagate in time keeping their energy profile.

General considerations and outlook

The major outcome of this thesis is the emergence of unique effects and dynamical behaviours controlled by the underlying geometry, for systems of strongly long-range interacting particles. These effects originate mostly by the "mixed dimensionality" of our setups, which involve on the one hand interactions through the full 3D space and on the other hand a constrained motion in 1D. We achieve such a property by imposing a confinement on a helical manifold, which has a reduced dimensionality but is embedded in the Euclidean 3D space. The degree of periodicity inherent to such systems adds significantly to their features, introducing a geometrical length scale, in analogy to lattice systems. Interestingly enough, the tuning of geometry parameters allows for a continuous transition from-and-to different manifolds of trivial geometry, such as the straight line or the circle.

Such characteristics, are advantageous, especially for many-body physical systems, since they can generate different degrees of complexity in a controlled manner. We have studied specific aspects of such systems, by exploring the low energy behaviour of charges on a commensurately filled closed helix within a certain regime of geometrical parameters. Our findings show that the character of interactions can be highly varied through geometry, allowing for a coupling or not of center-of-mass to the relative coordinate, and for different degrees and kinds of nonlinearity. A study of thermal transport could thus be of interest in such systems, given especially the existing debate about the essential and sufficient requirements for normal heat conduction [241–243]. Usually the existing theoretical studies deal with Fermi-Pasta-Ulam [240] or Frenkel-Kontorova lattice models [97], as different representatives of cases providing or not a center-of-mass separation. Our system, depending on the geometry parameters, can provide both cases. Although it generically possesses a periodicity which links it to a lattice model of the Frenkel-Kontorova type, it differs substantially from it, since it induces the center-of-mass coupling through interactions and not by means of an external potential. Furthermore, being 1D, it is embedded in the 3D space in contrast to the common 1D lattices and the lattice-like systems [91] in the form of sinusoidal waves, which lie in 2D. It can thus permit an additional dimension to get involved in the dynamics. In the same line of arguments, the inclusion of external fields can enrich the dynamical picture and even induce thermoelectric effects, such as those described in [93]. Explorations of this kind of toroidal systems at other fillings and parameter regimes are also expected to lead to interesting physical behaviours, associated with the existence of incommensurate phases and inter-winding couplings.

We note that in all the helical systems of charged particles, the potential landscape, becomes, beyond a parameter regime, very complex, supporting a plethora of different equilibrium states with very small energy differences, reminiscent of the structural complexity of glasses [244]. The implications of such a property have not been explored so far. To this extent, studies of the out-of-equilibrium dynamics, as well as, studies of the statistical behaviour and thermodynamics of such systems would be appealing. These could reveal intriguing aging and non-ergodic effects, as well as, unusual transitions between different metastable states.

Last but not least, we point out that a study of the quantum analogue of helically confined charges could be of considerable interest. Already the results for two particles confined on a uniform helix have revealed the possibility of forming fermionic pairs of large stability, which could allow for an exploration of Bose gases of bi-electron molecules [36]. The existence of multiple potential minima of different depths could induce unconventional collective excitations and dynamical mechanisms involving several time scales, originating from the tunneling between the different local minima. As stated above these might be quite different from the phenomena observed in lattice systems, since the oscillatory behaviour is a characteristic of the interactions rather than a property of the external potential. Further possibilities for enriching the physical behaviour of such quantum systems could be provided by the inclusion of spin [195] and the consideration of interactions with light [207]. The underlying picture would become even more complex, if one allows for deviations of the helical manifold from uniformity, since the insertion of an external geometric potential would be then essential [8, 10].

As it can be inferred from the above, the systems considered in this cumulative dissertation are of significant theoretical interest, a part of which is uncovered through our scientific contributions. A direct experimental realization of them, however, seems to be a demanding task with the currently available techniques, relying strongly on the experimental challenge of constructing a helical trap for charged particles. Nevertheless, there have been certain advances towards this direction, in different contexts, e.g. nanofabrication, optical trapping (see Sec. 1.3), which are promising for the future.

Appendix A

Supplementary material

A.1 Thermodynamic limit considerations

As a supplementary material to [O3] we present here some results relating to the thermodynamic limit $N, R \to \infty, a \to 0, aR = \frac{h}{2\pi}$ of the linear-to-zigzag bifurcation, found for charges confined on a toroidal helix. Below the critical value of the helix radius, r_{cr}, the lowest and the highest frequency of the system, corresponding to the center-of-mass (CM) and the out-of-phase (OP) modes respectively, read

$$\begin{aligned} \omega_{CM}^2 &= \frac{C(a,r,R)}{2^{3/2}\,(R+r)^2} r S_0(a,N) \\ \omega_{OP}^2 &= \frac{C(a,r,R)}{2^{5/2}\,(R+r)^3} \left(c_1(a,N)r^2 + 2c_2(a,N)Rr + c_3(a,N)R^2\right) \end{aligned} \tag{A.1}$$

with

$$\begin{aligned} C(a,r,R) &= \left(a^2(R+r)^2 + r^2\right)^{-1} \\ c_1(a,N) &= c_3(a,N) - 2(S_3(a,N) - S_2(a,N)) \\ c_2(a,N) &= c_3(a,N) + (S_1(a,N) - S_3(a,N)) \\ c_3(a,N) &= 3a^2(S_1(a,N) - S_2(a,N)) + a^2(S_3(a,N) - S_4(a,N)) \end{aligned} \tag{A.2}$$

and

$$\begin{aligned} S_0(a,N) &= \sum_{j=1}^{N-1} \left(1-\cos(au_j)\right)^{-1/2} \\ S_1(a,N) &= \sum_{j=1}^{N-1} \left(1-\cos(au_j)\right)^{-3/2} \\ S_2(a,N) &= \sum_{j=1}^{N-1} (-1)^j \left(1-\cos(au_j)\right)^{-3/2} \end{aligned}$$

$$
\begin{aligned}
S_3(a,N) &= \sum_{j=1}^{N-1} \cos(au_j)\,(1-\cos(au_j))^{-3/2} \\
S_4(a,N) &= \sum_{j=1}^{N-1} (-1)^j \cos(au_j)\,(1-\cos(au_j))^{-3/2} \qquad \text{(A.3)}
\end{aligned}
$$

In the thermodynamic limit the sums $S_i(a,N)$ diverge, due to $a \to 0$ with the following leading order contributions in terms of a

$$
\begin{aligned}
S_0(a,N) &\sim 2^{1/2}\pi^{-1}n^{-1}a^{-1} \\
S_1(a,N) &\sim S_3(a,N) \sim 2^{-1/2}\pi^{-3}n^{-3}a^{-3} \\
S_2(a,N) &\sim S_4(a,N) \sim -2^{-5/2}3\pi^{-3}n^{-3}a^{-3}. \qquad \text{(A.4)}
\end{aligned}
$$

In the same limit $C(a,r,R) \sim \left(\frac{h^2}{4\pi^2}+r^2\right)^{-1}$, i.e. it obtains finite values, independent of a, R.

These result in the following expressions for the center-of-mass and out-of-phase frequencies

$$
\begin{aligned}
\omega_{CM}^2 &\sim \frac{C(r)r}{2hnR} \to 0 \\
\omega_{OP}^2 &\sim \frac{7C(r)}{4nh^3\pi^3}\left(\frac{h^2}{\pi^2}-2r^2\right). \qquad \text{(A.5)}
\end{aligned}
$$

Evidently, the center-of-mass frequency becomes zero for all the values of the helix radius r in the thermodynamic limit, a fact that should be expected as the toroidal helix tends to an infinite homogeneous helix for which a center-of-mass separation is provided. The out-phase frequency becomes zero at the point $r_{cr} = \frac{h}{\sqrt{2}\pi}$, crossing thereafter to the imaginary axis. This point can be identified as the critical radius for the zigzag transition, denoted as r_∞ in [O3]. Since in the thermodynamic limit the point of degeneracy is also located at $r_d = r_\infty$ [O3], the linear spectrum is degenerate at zero frequency for $r = r_\infty = \frac{h}{\sqrt{2}\pi}$. In such a case, an analysis of the higher-order nonlinear terms is essential in order to extract information about the dynamical behaviour of the system.

The degeneracy at zero frequency generates questions about the form of the linear spectrum beyond the critical point. How can two frequency branches emerge from a single point at zero? As shown in Fig. A.1, directly after the bifurcation, one of the emergent branches of the zigzag solution consists of imaginary frequencies ($\omega^2 < 0$), rendering the corresponding configuration unstable in a narrow regime of r. Since within that regime both the polygonic and the zigzag configurations are unstable, a third equilibrium state exists, which for the specific parameters is the ground state. Such a state could emerge possibly from a saddle-node bifurcation for $r < r_\infty$ and thus be completely detached from the branch of the polygonic solution.

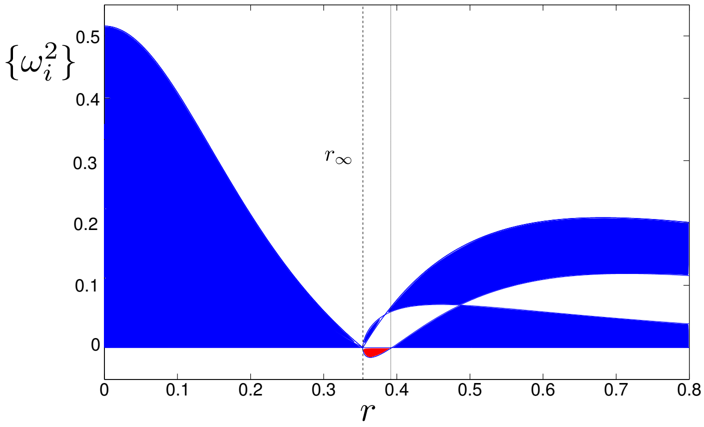

Figure A.1: The square values of the linearization spectrum as a function of r for the polygonic ($r < r_\infty$) and the zigzag ($r > r_\infty$) solution, as calculated in the thermodynamic limit for filling $\nu = 1/2$ and pitch $h = \pi/2$. The dashed line marks the critical point r_∞ and the red area the $\{\omega_i^2\} < 0$.

Although the detection of this third state is beyond the scope of the current thesis, some instructive conclusions can be drawn from the study of a finite system with a larger filling, namely a system of filling $\nu = 1$. Our results are presented in the following section.

A.2 Ground states for filling $\nu = 1$

We have observed in [O3] that for filling $\nu = 1/2$, even for a large number of particles ($N = 120$), the dependence of the ground state structure on the helix radius r can be described within the picture of a pitchfork bifurcation. Below the critical point r_{cr} the ground state is polygonic whereas beyond r_{cr} it is of a zigzag form. This picture was shown in the previous section to fail in the thermodynamic limit, since the zigzag configuration becomes unstable directly after the bifurcation, pointing to the existence of another ground state at this region.

It turns out that a similar behaviour is supported by commensurate systems with a greater filling than 1/2, namely for systems with $\nu = 1$. Although in such a case the zigzag configuration does not become unstable, it becomes apparent that close to the bifurcation point r_{cr}, another stable configuration exists with energy lower than the zigzag (Fig. A.2 (a),(b)). This configuration (C) has a mixed structure between the zigzag and the polygonic, in the sense that every third particle occupies the same position as in the polygonic case (at the outer circle of the torus), whereas the two particles in between are displaced in a zigzag-like manner.

In contrast to the zigzag configuration which emerges through a pitchfork bifur-

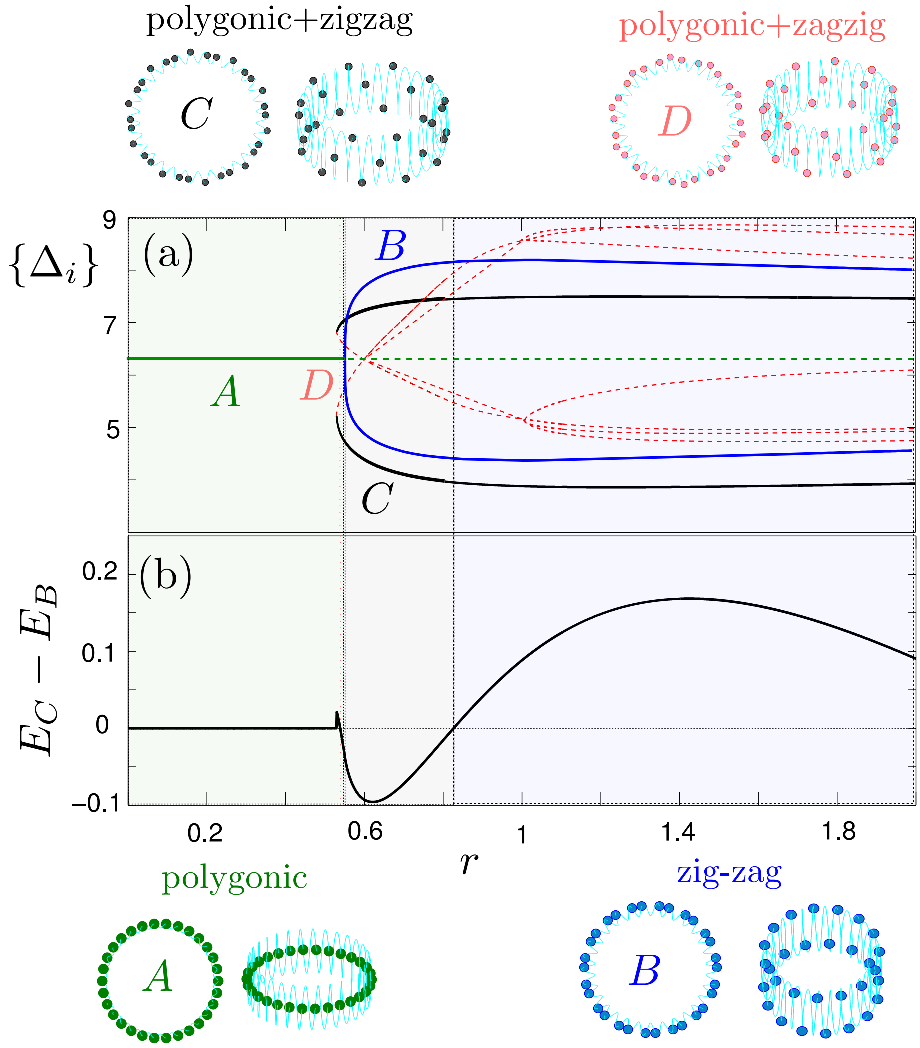

Figure A.2: (a) Equilibrium interparticle distances of particles $\Delta_i = u_{i+1} - u_i$ as a function of the helix radius r for filling $\nu = 1$ and $N = 30$ particles. For the polygonic configuration (A) all the nearest-neighbour distances Δ_i^A are equal. For the zigzag configuration (B) there are two different kinds of distances, half of which are greater and half lower than Δ_i^A. There is another state (C) which is a mixture of the polygonic and the zigzag phase and has again two kinds of distances, with the larger one (upper branch) appearing twice as frequently as the lower branch. The configuration D is the unstable pair of C. Note that all the distances are plotted on top of each other. The dashed lines correspond to unstable solutions. (b) The energy difference between the configuration C and B as a function of the helix radius r. In the region where it is negative (gray area) the state C is the ground state of the system.The colour of each area marks the corresponding ground state configuration (green → polygonic, blue → zigzag). All the relevant configurations are depicted in the borders of the figure.

cation from the polygonic solution, the new state C arises independently through a saddle-node bifurcation together with its unstable pair D (Fig. A.2 (a)). In a narrow region around r_{cr} it attains an energy E_C less than that the energy of the zigzag state E_B and therefore becomes the ground state of the system (Fig. A.2 (b)). A configuration of a mixed-zigzag-and-polygonic type such as C, might be the ground state configuration missing in the thermodynamic limit description, in the regime where the zigzag solution is unstable.

The results in this subsection, obtained for $N = 30$, suggest that even for commensurate cases (which are dense enough), the system of the charges confined on a toroidal helix has a large structural complexity. The study of the geometrical dependence of the equilibrium structures for different number of particles N and different fillings ν as well as the analysis of the corresponding structural transitions, could be an interesting subject for further investigation.

Acknowledgements

First and foremost, I would like to thank my supervisor Prof. Peter Schmelcher for introducing me to the field of cold ion physics and to the beautiful aspects of constrained motion in curved manifolds. I am grateful to him for inspiring me and teaching me how to pursue my ideas in research in a scientifically sound way. His advices and support these three years have been essential elements for the completion of this thesis.

I would also like to express my gratitude to Prof. Fotis Diakonos and Prof. Panagiotis Kevrekidis for several fruitful discussions and for providing me with insight into various numerical techniques.

Many thanks are also due to Jan Stockhofe for numerous constructive and enjoyable discussions, for his valuable comments and suggestions concerning most of the works presented here and for his helpful remarks regarding this thesis.

My sincere thanks to the International Max Planck Research School for Ultrafast Imaging and Structural Dynamics (IMPRS-UFAST) for supporting me through a PhD scholarship these three years.

I am indebted to Christian Morfonios for his valuable comments, as well as to Simos Mistakidis and Giorgis Koutentakis for proofreading this thesis.

I am heartfully thankful to my friends and colleagues Christian, Simos, Panos, Yannis, Lia, Giorgis and Vaggelis for many extended and insightful discussions (scientific or not), for supporting me in difficulties and for making my life in and out the office nicer.

Concerning especially the time in the office, I would like to thank my colleagues Johannes K., Gaoren, Benno, Valentin, Johannes S., Lushuai, Sven, Jan, Andrea, Thomas, Malte, Markus, Christian F. and Tobias for knowledge exchange and for many enjoyable moments. I am particularly grateful to Johannes K. for his initiative to teach me the German word of the day the last two years and for the enlightening discussions that followed, adding a different “colour” to each office-day.

Thanks are also due to all the IMPRS-students for the nice moments and the interchange of scientific knowledge from different disciplines. I am especially thankful to Sharareh Sayyad for our joint presentations which apart from fun have been a source of learning about different concepts in modern physics.

Outside of my direct scientific environment I had the pleasure to get to know Maria, Eleni, Monika, Elina, Sonja, Lena, Kleopatra, Jasone, Antonia and many others which with their friendship have contributed in making my moments of sorrow half and my moments of joy double.

Last but by no means least, I would like to express my heartfelt gratitude to my family for being always there, or better “here”, despite the long distance and for providing me with their constant love and support which make everything so much easier.

Bibliography

[1] K. von Klitzing. The quantized Hall effect. *Rev. Mod. Phys.*, 58(3):519–531, 1986.

[2] A. K. Geim and K. S. Novoselov. The rise of graphene. *Nature Materials*, 6(3):183–191, 2007.

[3] A. H. Castro Neto, F. Guinea, N. M. R. Peres, K. S. Novoselov, and A. K. Geim. The electronic properties of graphene. *Rev. Mod. Phys.*, 81(1):109–162, 2009.

[4] Jean-Christophe Charlier, Xavier Blase, and Stephan Roche. Electronic and transport properties of nanotubes. *Rev. Mod. Phys.*, 79(2):677–732, 2007.

[5] E. A. Laird, F. Kuemmeth, G. A. Steele, K. Grove-Rasmussen, J. Nygrd, K. Flensberg, and L. P. Kouwenhoven. Quantum transport in carbon nanotubes. *Rev. Mod. Phys.*, 87(3):703–764, 2015.

[6] M. Reibold, P. Paufler, A. A. Levin, W. Kochmann, N. Ptzke, and D. C. Meyer. Materials: Carbon nanotubes in an ancient Damascus sabre. *Nature*, 444(7117):286–286, 2006.

[7] L. P. Kouwenhoven, C. M. Marcus, P. L. McEuen, S. Tarucha, R. M. Westervelt, and N. S. Wingreen. *Electron Transport in Quantum Dots*. Springer Netherlands, 1997.

[8] P. Exner and H. Kovařík. *Quantum Waveguides*. Springer, 2015.

[9] H. Jensen and H. Koppe. Quantum mechanics with constraints. *Annals of Physics*, 63(2):586–591, 1971.

[10] R. C. T. da Costa. Quantum mechanics of a constrained particle. *Phys. Rev. A*, 23(4):1982–1987, 1981.

[11] P. Exner and P. Seba. Bound states in curved quantum waveguides. *J. Math. Phys.*, 30(11):2574–2580, 1989.

[12] P. Duclos and P. Exner. Curvature-induced bound states in quantum waveguides in two and three dimensions. *Rev. Math. Phys.*, 07(1):73–102, 1995.

[13] L. I. Magarill and M. V. Entin. Electrons in a curvilinear quantum wire. *Journal of Experimental and Theoretical Physics*, 96(4):766–774, 2003.

[14] P. Exner and M. Fraas. A remark on helical waveguides. *Phys. Lett. A*, 369(56):393–399, 2007.

[15] C. Ortix and J. van den Brink. Effect of curvature on the electronic structure and bound-state formation in rolled-up nanotubes. *Phys. Rev. B*, 81(16):165419, 2010.

[16] C. Ortix, S. Kiravittaya, O. G. Schmidt, and J. van den Brink. Curvature-induced geometric potential in strain-driven nanostructures. *Phys. Rev. B*, 84(4):045438, 2011.

[17] V. Atanasov and R. Dandoloff. Curvature-induced quantum behaviour on a helical nanotube. *Phys. Lett. A*, 372(40):6141–6144, 2008.

[18] V. Atanasov, R. Dandoloff, and A. Saxena. Geometry-induced charge separation on a helicoidal ribbon. *Phys. Rev. B*, 79(3):033404, 2009.

[19] D. A. Wharam and T. Heinzel. *Coulomb Blockade in Quantum Dots.* Number 291. Springer Netherlands, 1995.

[20] H. L. Stormer, D. C. Tsui, and A. C. Gossard. The fractional quantum hall effect. *Rev. Mod. Phys.*, 71(2):S298–S305, 1999.

[21] G. Zs K. Horvath, R. C. Thompson, and P. L. Knight. Fundamental physics with trapped ions. *Contemporary Physics*, 38(1):25–48, 1997.

[22] M. Knoop, I. Marzoli, and G. Morigi. *Ion Traps for Tomorrows Applications.* IOS Press, 2015.

[23] I. Bloch, J. Dalibard, and W. Zwerger. Many-body physics with ultracold gases. *Rev. Mod. Phys.*, 80(3):885–964, 2008.

[24] S. Fishman, G. De Chiara, T. Calarco, and G. Morigi. Structural phase transitions in low-dimensional ion crystals. *Phys. Rev. B*, 77(6):064111, 2008.

[25] T. Kinoshita, T. Wenger, and D. S. Weiss. Observation of a One-Dimensional Tonks-Girardeau Gas. *Science*, 305(5687):1125–1128, 2004.

[26] B. Paredes, A. Widera, V. Murg, O. Mandel, S. Fölling, I. Cirac, G. V. Shlyapnikov, Theodor W. Hänsch, and I. Bloch. Tonks-Girardeau gas of ultracold atoms in an optical lattice. *Nature*, 429(6989):277–281, 2004.

[27] M. Köhl, H. Moritz, T. Stöferle, C. Schori, and T. Esslinger. Superfluid to Mott insulator transition in one, two, and three dimensions. *Journal of Low Temperature Physics*, 138(3-4):635–644, 2005.

[28] F. G. Major, V. N. Gheoerghe, and G. Werth. *Charged Particle Traps: Physics and Techniques of Charged Particle Field Confinement.* Springer, Berlin, New York, 2005 edition, 2004.

[29] P. K. Ghosh. *Ion Traps.* Clarendon Press, Oxford : New York, 1 edition, 1996.

[30] R. Grimm, M. Weidemüller, and Y. B. Ovchinnikov. Optical Dipole Traps for Neutral Atoms. *Adv. At. Mol. Opt. Phys*, 42:95–170, 2000.

[31] O. Morsch, J. H. Mller, M. Cristiani, D. Ciampini, and E. Arimondo. Bloch Oscillations and Mean-Field Effects of Bose-Einstein Condensates in 1d Optical Lattices. *Phys. Rev. Lett.*, 87(14):140402, 2001.

[32] Ph. Courteille, R. S. Freeland, D. J. Heinzen, F. A. van Abeelen, and B. J. Verhaar. Observation of a Feshbach Resonance in Cold Atom Scattering. *Phys. Rev. Lett.*, 81(1):69–72, 1998.

[33] S. Inouye, M. R. Andrews, J. Stenger, H.-J. Miesner, D. M. Stamper-Kurn, and W. Ketterle. Observation of Feshbach resonances in a Bose-Einstein condensate. *Nature*, 392(6672):151–154, 1998.

[34] K. C. Wright, R. B. Blakestad, C. J. Lobb, W. D. Phillips, and G. K. Campbell. Driving Phase Slips in a Superfluid Atom Circuit with a Rotating Weak Link. *Phys. Rev. Lett.*, 110(2):025302, 2013.

[35] S. Viefers, P. Koskinen, P. Singha Deo, and M. Manninen. Quantum rings for beginners: energy spectra and persistent currents. *Physica E*, 21(1):1–35, 2004.

[36] O. V. Kibis. Electron-electron interaction in a spiral quantum wire. *Phys. Lett. A*, 166(5):393–394, 1992.

[37] K. T. Law and D. E. Feldman. Quantum phase transition between a Luttinger liquid and a gas of cold molecules. *Phys. Rev. Lett.*, 101(9):096401, 2008.

[38] P. Schmelcher. Effective long-range interactions in confined curved dimensions. *Europhys. Lett.*, 95(5):50005, 2011.

[39] J. K. Pedersen, D. V. Fedorov, A. S. Jensen, and N. T. Zinner. Formation of classical crystals of dipolar particles in a helical geometry. *J. Phys. B*, 47(16):165103, 2014.

[40] K. H. Kingdon. A Method for the Neutralization of Electron Space Charge by Positive Ionization at Very Low Gas Pressures. *Phys. Rev.*, 21(4):408–418, 1923.

[41] F. M. Penning. Die Glimmentladung bei niedrigem Druck zwischen koaxialen Zylindern in einem axialen Magnetfeld. *Physica*, 3(9):873–894, 1936.

[42] W. Paul, H. P. Reinhard, and U. von Zahn. Das elektrische Massenfilter als Massenspektrometer und Isotopentrenner. *Zeitschrift für Physik*, 152(2):143–182, 1958.

[43] E. Fischer. Die dreidimensionale Stabilisierung von Ladungstrgern in einem Vierpolfeld. *Zeitschrift für Physik*, 156(1):1–26, 1959.

[44] H. G. Dehmelt and F. L. Walls. "Bolometric" Technique for the rf Spectroscopy of Stored Ions. *Phys. Rev. Lett.*, 21(3):127–131, 1968.

[45] H. G. Dehmelt. Radiofrequency Spectroscopy of Stored Ions I: Storage. *Adv. At. Mol. Phys.*, 3:53–72, 1968.

[46] H. G. Dehmelt. Radiofrequency Spectroscopy of Stored Ions II: Spectroscopy*. In D. R. Bates and Immanuel Estermann, editor, *Advances in Atomic and Molecular Physics*, volume 5, pages 109–154. Academic Press, 1969.

[47] G. Graff, F. G. Major, R. W. H. Roeder, and G. Werth. Method for Measuring the Cyclotron and Spin Resonance of Free Electrons. *Phys. Rev. Lett.*, 21(6):340–342, 1968.

[48] W. D. Phillips. Laser cooling and trapping of neutral atoms. *Rev. Mod. Phys.*, 70(3):721, 1998.

[49] W. Neuhauser, M. Hohenstatt, P. E. Toschek, and H. G. Dehmelt. Visual observation and optical cooling of electrodynamically contained ions. *Applied physics*, 17(2):123–129, 1978.

[50] W. Neuhauser, M. Hohenstatt, P. Toschek, and H. Dehmelt. Optical-Sideband Cooling of Visible Atom Cloud Confined in Parabolic Well. *Phys. Rev. Lett.*, 41(4):233–236, 1978.

[51] J. Eschner, B. Appasamy, and P. E. Toschek. Stochastic Cooling of a Trapped Ion by Null Detection of Its Fluorescence. *Phys. Rev. Lett.*, 74(13):2435–2438, 1995.

[52] J. Eschner, G. Morigi, F. Schmidt-Kaler, and R. Blatt. Laser cooling of trapped ions. *J. Opt. Soc. Am. B*, 20(5):1003, 2002.

[53] D. J. Wineland, W. M. Itano, and R. S Vandyck. High-Resolution Spectroscopy of Stored Ions. *Advances in Atomic and Molecular Physics*, 19:135–186, 1983.

[54] D. J. Wineland. Trapped Ions, Laser Cooling, and Better Clocks. *Science*, 226(4673):395–400, 1984.

[55] P. E. Toschek and W. Neuhauser. Spectroscopy on Localized and Cooled Ions. In Daniel Kleppner and Francis M. Pipkin, editors, *Atomic Physics 7*, pages 529–552. Springer US, 1981.

[56] B. Appasamy, Y. Stalgies, and P. E. Toschek. Measurement-Induced Vibrational Dynamics of a Trapped Ion. *Phys. Rev. Lett.*, 80(13):2805–2808, 1998.

[57] W. Neuhauser, M. Hohenstatt, P. E. Toschek, and H. Dehmelt. Localized visible Ba^+ mono-ion oscillator. *Phys. Rev. A*, 22(3):1137–1140, 1980.

[58] E. Wigner. On the Interaction of Electrons in Metals. *Phys. Rev.*, 46:1002–1011, 1934.

[59] M. Bonitz et al. Classical and quantum Coulomb crystals. *Physics of Plasmas*, 15(5):055704, 2008.

[60] J. P. Hansen. Statistical Mechanics of Dense Ionized Matter. I. Equilibrium Properties of the Classical One-Component Plasma. *Phys. Rev. A*, 8(6):3096–3109, 1973.

[61] E. L. Pollock and J. P. Hansen. Statistical Mechanics of Dense Ionized Matter. II. Equilibrium Properties and Melting Transition of the Crystallized One-Component Plasma. *Phys. Rev. A*, 8(6):3110–3122, 1973.

[62] S. Ichimaru. Strongly coupled plasmas: high-density classical plasmas and degenerate electron liquids. *Rev. Mod. Phys.*, 54(4):1017–1059, 1982.

[63] J. P. Schiffer. Order in confined ions. *J. Phys. B*, 36(3):511, 2003.

[64] F. J. Rogers and H. E. Dewitt. *Strongly Coupled Plasma Physics*. Springer Science & Business Media, 2013.

[65] R. W. Hasse and V. V. Avilov. Structure and Madelung energy of spherical Coulomb crystals. *Phys. Rev. A*, 44(7):4506–4515, October 1991.

[66] D. H. E. Dubin and T. M. O'Neil. Trapped nonneutral plasmas, liquids, and crystals (the thermal equilibrium states). *Rev. Mod. Phys.*, 71(1):87–172, 1999.

[67] H. Totsuji, T. Kishimoto, C. Totsuji, and K. Tsuruta. Competition between Two Forms of Ordering in Finite Coulomb Clusters. *Phys. Rev. Lett.*, 88(12):125002, 2002.

[68] C. C. Grimes and G. Adams. Evidence for a Liquid-to-Crystal Phase Transition in a Classical, Two-Dimensional Sheet of Electrons. *Phys. Rev. Lett.*, 42(12):795–798, 1979.

[69] Y. Monarkha and K. Kono. *Two-Dimensional Coulomb Liquids and Solids*. Springer Science & Business Media, 2013.

[70] M. W. Cole. Electronic surface states of liquid helium. *Rev. Mod. Phys.*, 46(3):451–464, 1974.

[71] Yu. E. Lozovik and V. A. Mandelshtam. Classical and quantum melting of a Coulomb cluster in a trap. *Phys. Lett. A*, 165(56):469–472, 1992.

[72] V. M. Bedanov and F. M. Peeters. Ordering and phase transitions of charged particles in a classical finite two-dimensional system. *Phys. Rev. B*, 49(4):2667–2676, 1994.

[73] J. J. Thomson. On the structure of the atom. *Philos. Mag.*, 7(2):237, 1904.

[74] R. Backofen, A. Voigt, and T. Witkowski. Particles on curved surfaces: A dynamic approach by a phase-field-crystal model. *Phys. Rev. E*, 81(2):025701, 2010.

[75] T. Erber and G. M. Hockney. Equilibrium configurations of N equal charges on a sphere. *Journal of Physics A: Mathematical and General*, 24(23):L1369, 1991.

[76] E. L. Altschuler and A. Pérez-Garrido. Global minimum for Thomson's problem of charges on a sphere. *Phy. Rev. E*, 71(4):047703, 2005.

[77] E. L. Altschuler and A. Pérez-Garrido. Defect-free global minima in Thomson's problem of charges on a sphere. *Phys. Rev. E*, 73(3):036108, 2006.

[78] T. Müller and J. Frauendiener. Charged particles constrained to a curved surface. *Eur. J. Phys.*, 34(1):147, 2013.

[79] M. J. Bowick and L. Giomi. Two-dimensional matter: order, curvature and defects. *Advances in Physics*, 58(5):449–563, 2009.

[80] H. J. Schulz. Wigner crystal in one dimension. *Phys. Rev. Lett.*, 71(12):1864–1867, 1993.

[81] D. H. E. Dubin. Minimum energy state of the one-dimensional Coulomb chain. *Phys.Rev. E*, 55(4):4017–4028, 1997.

[82] G. Morigi and S. Fishman. Eigenmodes and Thermodynamics of a Coulomb Chain in a Harmonic Potential. *Phys. Rev. Lett.*, 93(17):170602, 2004.

[83] G. Morigi and S. Fishman. Dynamics of an ion chain in a harmonic potential. *Phys. Rev. E*, 70(6):066141, 2004.

[84] G. Morigi and S. Fishman. One-dimensional Coulomb crystals at low temperatures. *J. Phys. B*, 39(10):S221, 2006.

[85] I. García-Mata, O. V. Zhirov, and D. L. Shepelyansky. Frenkel-Kontorova model with cold trapped ions. *Eur. Phys. J. D*, 41(2):325–330, 2006.

[86] V. V. Deshpande and M. Bockrath. The one-dimensional Wigner crystal in carbon nanotubes. *Nature Physics*, 4(4):314–318, 2008.

[87] J. S. Meyer and K. A. Matveev. Wigner crystal physics in quantum wires. *Journal of Physics: Condensed Matter*, 21(2):023203, 2009.

[88] V. V. Deshpande, M. Bockrath, L. I. Glazman, and A. Yacoby. Electron liquids and solids in one dimension. *Nature*, 464(7286):209–216, 2010.

[89] K. A. Matveev, A. V. Andreev, and M. Pustilnik. Equilibration of a One-Dimensional Wigner Crystal. *Phys. Rev. Lett.*, 105(4):046401, 2010.

[90] T. Pruttivarasin, M. Ramm, I. Talukdar, A. Kreuter, and H. Häffner. Trapped ions in optical lattices for probing oscillator chain models. *New J. Phys.*, 13(7):075012, 2011.

[91] O. V. Zhirov and D. L. Shepelyansky. Wigner crystal in snaked nanochannels. *Eur. Phys. J. B*, 82(1):63–67, 2011.

[92] J. Lin, K. A. Matveev, and M. Pustilnik. Thermalization of Acoustic Excitations in a Strongly Interacting One-Dimensional Quantum Liquid. *Phys. Rev. Lett.*, 110(1):016401, 2013.

[93] O. V. Zhirov and D. L. Shepelyansky. Thermoelectricity of Wigner crystal in a periodic potential. *Europhys. Lett.*, 103(6):68008, 2013.

[94] P. C. Hohenberg. Existence of Long-Range Order in One and Two Dimensions. *Phys. Rev.*, 158(2):383–386, 1967.

[95] G. Birkl, S. Kassner, and H. Walther. Multiple-shell structures of laser-cooled 24 Mg+ ions in a quadrupole storage ring. *Nature*, 357(6376):310–313, 1992.

[96] M. G. Raizen, J. M. Gilligan, J. C. Bergquist, W. M. Itano, and D. J. Wineland. Ionic crystals in a linear Paul trap. *Physical Review A*, 45(9):6493–6501, 1992.

[97] O. M. Braun and Yu. Kivshar. *The Frenkel-Kontorova Model: Concepts, Methods, and Applications.* Springer Science & Business Media, 2013.

[98] Ch. Schneider, M. Enderlein, T. Huber, and T. Schaetz. Optical trapping of an ion. *Nature Photonics*, 4(11):772–775, 2010.

[99] D. Gerlich. Inhomogeneous RF Fields: A Versatile Tool for the Study of Processes with Slow Ions. In *Advances in Chemical Physics*, pages 1–176. John Wiley & Sons, Inc., 1992.

[100] C. Champenois. About the dynamics and thermodynamics of trapped ions. *J. Phys. B*, 42(15):154002, 2009.

[101] K. Okada, K. Yasuda, T. Takayanagi, M. Wada, H. A. Schuessler, and S. Ohtani. Crystallization of Ca^+ ions in a linear rf octupole ion trap. *Phys. Rev. A*, 75(3):033409, 2007.

[102] K. Okada, T. Takayanagi, M. Wada, S. Ohtani, and H. A. Schuessler. Observation of ion Coulomb crystals in a cryogenic linear octupole rf ion trap. *Phys. Rev. A*, 80(4):043405, 2009.

[103] E. Yurtsever, E. D. Onal, and F. Calvo. Structure and dynamics of ion clusters in linear octupole traps: Phase diagrams, chirality, and melting mechanisms. *Phys. Rev. A*, 83(5):053427, 2011.

[104] F. Cartarius, C. Cormick, and G. Morigi. Stability and dynamics of ion rings in linear multipole traps. *Phys. Rev. A*, 87(1):013425, 2013.

[105] M. Fujimoto. *The Physics of Structural Phase Transitions.* Springer-Verlag, New York, 1997.

[106] G. Piacente, I. V. Schweigert, J. J. Betouras, and F. M. Peeters. Generic properties of a quasi-one-dimensional classical Wigner crystal. *Phys. Rev. B*, 69(4):045324, 2004.

[107] R. W Hasse and J. P Schiffer. The structure of the cylindrically confined Coulomb lattice. *Annals of Physics*, 203(2):419–448, 1990.

[108] N. Kjærgaard and M. Drewsen. Observation of a Structural Transition for Coulomb Crystals in a Linear Paul Trap. *Phys. Rev. Lett.*, 91(9):095002, 2003.

[109] M. Drewsen, I. S. Jensen, N. Kjærgaard, J. Lindballe, A. Mortensen, K. Mlhave, and Dirk V. Non-stationary Coulomb crystals in linear Paul traps. *J. Phys. B*, 36(3):525, 2003.

[110] M. Drewsen, I. Jensen, J. Lindballe, N. Nissen, R. Martinussen, A. Mortensen, P. Staanum, and D. Voigt. Ion Coulomb crystals: a tool for studying ion processes. *International Journal of Mass Spectrometry*, 229(12):83–91, 2003.

[111] D. H. E. Dubin. Theory of structural phase transitions in a trapped Coulomb crystal. *Phys. Rev. Lett.*, 71(17):2753–2756, 1993.

[112] J. E. Galván-Moya and F. M. Peeters. Ginzburg-Landau theory of the zigzag transition in quasi-one-dimensional classical Wigner crystals. *Phys. Rev. B*, 84(13):134106, 2011.

[113] R. Nigmatullin, A. del Campo, G. De Chiara, G. Morigi, M. B. Plenio, and A. Retzker. Formation of helical ion chains. *arXiv:1112.1305*, 2011.

[114] E. Shimshoni, G. Morigi, and S. Fishman. Quantum Zigzag Transition in Ion Chains. *Phys. Rev. Lett.*, 106(1):010401, 2011.

[115] P. Silvi, T. Calarco, G. Morigi, and S. Montangero. *Ab initio* characterization of the quantum linear-zigzag transition using density matrix renormalization group calculations. *Phys. Rev. B*, 89(9):094103, March 2014.

[116] J. S. Meyer, K. A. Matveev, and A. I. Larkin. Transition from a One-Dimensional to a Quasi-One-Dimensional State in Interacting Quantum Wires. *Phys. Rev. Lett.*, 98(12).

[117] D. Porras and J. I. Cirac. Effective Quantum Spin Systems with Trapped Ions. *Phys. Rev. Lett.*, 92(20):207901, 2004.

[118] E. Jané, G. Vidal, W. Dür, P. Zoller, and J. I. Cirac. Simulation of Quantum Dynamics with Quantum Optical Systems. *Quantum Info. Comput.*, 3(1):15–37, 2003.

[119] M. Johanning, A. F. Varón, and C. Wunderlich. Quantum simulations with cold trapped ions. *J. Phys. B*, 42(15):154009, 2009.

[120] R. Blatt and C. F. Roos. Quantum simulations with trapped ions. *Nature Physics*, 8(4):277–284, 2012.

[121] Ch. Schneider, D. Porras, and T. Schaetz. Experimental quantum simulations of many-body physics with trapped ions. *Rep. Prog. Phys.*, 75(2):024401, 2012.

[122] P. Schindler, M. Mller, D. Nigg, J. T. Barreiro, E. A. Martinez, M. Hennrich, T. Monz, S. Diehl, P. Zoller, and R. Blatt. Quantum simulation of dynamical maps with trapped ions. *Nature Physics*, 9(6):361–367, 2013.

[123] D. Leibfried, B. DeMarco, V. Meyer, M. Rowe, A. Ben-Kish, J. Britton, W. M. Itano, B. Jelenković, C. Langer, T. Rosenband, and D. J. Wineland. Trapped-Ion Quantum Simulator: Experimental Application to Nonlinear Interferometers. *Phys. Rev. Lett.*, 89(24):247901, 2002.

[124] H. Schmitz, R. Matjeschk, Ch. Schneider, J. Glueckert, M. Enderlein, T. Huber, and T. Schaetz. Quantum Walk of a Trapped Ion in Phase Space. *Phys. Rev. Lett.*, 103(9):090504, 2009.

[125] A. Friedenauer, H. Schmitz, J. T. Glueckert, D. Porras, and T. Schaetz. Simulating a quantum magnet with trapped ions. *Nature Physics*, 4(10):757–761, 2008.

[126] K. Kim, M.-S. Chang, S. Korenblit, R. Islam, E. E. Edwards, J. K. Freericks, G.-D. Lin, L.-M. Duan, and C. Monroe. Quantum simulation of frustrated Ising spins with trapped ions. *Nature*, 465(7298):590–593, 2010.

[127] R. Islam, E. E. Edwards, K. Kim, S. Korenblit, C. Noh, H. Carmichael, G.-D. Lin, L.-M. Duan, C.-C. Joseph Wang, J. K. Freericks, and C. Monroe. Onset of a quantum phase transition with a trapped ion quantum simulator. *Nature Communications*, 2:377, 2011.

[128] J. I. Cirac and P. Zoller. Quantum Computations with Cold Trapped Ions. *Phys. Rev. Lett.*, 74(20):4091–4094, 1995.

[129] D. Kielpinski, C. Monroe, and D. J. Wineland. Architecture for a large-scale ion-trap quantum computer. *Nature*, 417(6890):709–711, 2002.

[130] C. Monroe. Quantum information processing with atoms and photons. *Nature*, 416(6877):238–246, 2002.

[131] F. Schmidt-Kaler, H. Häffner, M. Riebe, S. Gulde, G. P. T. Lancaster, T. Deuschle, C. Becher, C. F. Roos, J. Eschner, and R. Blatt. Realization of the Cirac-Zoller controlled-NOT quantum gate. *Nature*, 422(6930):408–411, 2003.

[132] H. Häffner, C. F. Roos, and R. Blatt. Quantum computing with trapped ions. *Phys. Rep.*, 469(4):155–203, 2008.

[133] J. Benhelm, G. Kirchmair, C. F. Roos, and R. Blatt. Towards fault-tolerant quantum computing with trapped ions. *Nature Physics*, 4(6):463–466, 2008.

[134] J. M. Amini, H. Uys, J. H. Wesenberg, S. Seidelin, J. Britton, J. J. Bollinger, D. Leibfried, C. Ospelkaus, A. P. VanDevender, and D. J. Wineland. Toward scalable ion traps for quantum information processing. *New J. Phys.*, 12(3):033031, 2010.

[135] L.-M. Duan and C. Monroe. *Colloquium* : Quantum networks with trapped ions. *Rev. Mod. Phys.*, 82(2):1209–1224, 2010.

[136] D. J. Wineland and D. Leibfried. Quantum information processing and metrology with trapped ions. *Laser Physics Letters*, 8(3):175–188, 2011.

[137] C. Monroe and J. Kim. Scaling the Ion Trap Quantum Processor. *Science*, 339(6124):1164–1169, 2013.

[138] T. Choi, S. Debnath, T.A. Manning, C. Figgatt, Z.-X. Gong, L.-M. Duan, and C. Monroe. Optimal Quantum Control of Multimode Couplings between Trapped Ion Qubits for Scalable Entanglement. *Phys. Rev. Lett.*, 112(19):190502, 2014.

[139] T.P. Harty, D.T.C. Allcock, C.J. Ballance, L. Guidoni, H.A. Janacek, N.M. Linke, D.N. Stacey, and D.M. Lucas. High-Fidelity Preparation, Gates, Memory, and Readout of a Trapped-Ion Quantum Bit. *Phys. Rev. Lett.*, 113(22):220501, 2014.

[140] R. Blatt, P. Gill, and Thompson R. C. Current perspectives on the physics of trapped ions. *J. Mod. Opt.*, 39(7198):193–220, 1992.

[141] M. E. Poitzsch, J. C. Bergquist, W. M. Itano, and D. J. Wineland. Cryogenic linear ion trap for accurate spectroscopy. *Review of Scientific Instruments*, 67(1):129–134, 1996.

[142] R. C. Thompson. Spectroscopy of Trapped Ions. *Adv. At., Mol. Opt. Phys.*, 31:63–136, 1993.

[143] P. T. H. Fisk. Trapped-ion and trapped-atom microwave frequency standards. *Rep. Prog. Phys.*, 60(8):761, 1997.

[144] D. J. Berkeland, J. D. Miller, J. C. Bergquist, W. M. Itano, and D. J. Wineland. Laser-Cooled Mercury Ion Frequency Standard. *Phys. Rev. Lett.*, 80(10):2089–2092, 1998.

[145] A. N. Luiten. *Frequency Measurement and Control: Advanced Techniques and Future Trends.* Springer Science & Business Media, 2003.

[146] R. E. March and J. F. J. Todd. *Practical Aspects of Trapped Ion Mass Spectrometry, Volume V: Applications of Ion Trapping Devices.* CRC Press, 2009.

[147] F. Schlawin, M.l Gessner, S. Mukamel, and A. Buchleitner. Nonlinear spectroscopy of trapped ions. *Phys. Rev. A*, 90(2):023603, 2014.

[148] H. B. Pedersen, D. Strasser, S. Ring, O. Heber, M. L. Rappaport, Y. Rudich, I. Sagi, and D. Zajfman. Ion Motion Synchronization in an Ion-Trap Resonator. *Phys. Rev. Lett.*, 87(5):055001, 2001.

[149] P. Jurcevic, P. Hauke, C. Maier, C. Hempel, B.P. Lanyon, R. Blatt, and C.F. Roos. Spectroscopy of Interacting Quasiparticles in Trapped Ions. *Phys. Rev. Lett.*, 115(10):100501, 2015.

[150] R. S. Van Dyck, P. B. Schwinberg, and H. G. Dehmelt. Precise Measurements of Axial, Magnetron, Cyclotron, and Spin-Cyclotron-Beat Frequencies on an Isolated 1-meV Electron. *Phys. Rev. Lett.*, 38(7):310–314, 1977.

[151] R. S. Van Dyck, P. B. Schwinberg, and H. G. Dehmelt. Electron magnetic moment from geonium spectra: Early experiments and background concepts. *Phys. Rev. D*, 34(3):722–736, 1986.

[152] H. Dehmelt. Experiments with an isolated subatomic particle at rest. *Rev. Mod. Phys.*, 62(3):525–530, 1990.

[153] M. Herrmann, V. Batteiger, S. Knünz, G. Saathoff, Th. Udem, and T. W. Hänsch. Frequency Metrology on Single Trapped Ions in the Weak Binding Limit: The $3s_{1/2} - 3p_{3/2}$ Transition in $^{24}\mathrm{Mg}^{+}$. *Phys. Rev. Lett.*, 102(1):013006, 2009.

[154] N. Hermanspahn, H. Häffner, H.-J. Kluge, W. Quint, S. Stahl, J. Verdú, and G. Werth. Observation of the Continuous Stern-Gerlach Effect on an Electron Bound in an Atomic Ion. *Phys. Rev. Lett.*, 84(3):427–430, 2000.

[155] H. Dehmelt. Continuous Stern-Gerlach effect: Noise and the measurement process. *Proceedings of the National Academy of Sciences of the United States of America*, 83(10):3074–3077, 1986.

[156] R. Blümel, J. M. Chen, E. Peik, W. Quint, W. Schleich, Y. R. Shen, and H. Walther. Phase transitions of stored laser-cooled ions. *Nature*, 334(6180):309–313, 1988.

[157] R. G. Brewer, J. Hoffnagle, R. G. DeVoe, L. Reyna, and W. Henshaw. Collision-induced two-ion chaos. *Nature*, 344(6264):305–309, 1990.

[158] J. Hoffnagle and R. G. Brewer. Frequency-locked motion of two particles in a Paul trap. *Phys. Rev. Lett.*, 71(12):1828–1831, September 1993.

[159] C. Petri, S. Meyer, F. Lenz, and P. Schmelcher. Correlations and pair emission in the escape dynamics of ions from one-dimensional traps. *New J. Phys.*, 13(2):023006, 2011.

[160] T. E. Lee and M. C. Cross. Pattern Formation with Trapped Ions. *Phys. Rev. Lett.*, 106(14):143001, 2011.

[161] H. Landa, S. Marcovitch, A. Retzker, M. B. Plenio, and B. Reznik. Quantum Coherence of Discrete Kink Solitons in Ion Traps. *Phys. Rev. Lett.*, 104(4):043004, 2010.

[162] H. Landa, B. Reznik, J. Brox, M. Mielenz, and T. Schaetz. Structure, dynamics and bifurcations of discrete solitons in trapped ion crystals. *New J. Phys.*, 15(9):093003, 2013.

[163] A. Klumpp, Benno Liebchen, and P. Schmelcher. Quench Dynamics of Two Coupled Ionic Zig-Zag Chains. *arXiv:1508.07979 [physics]*, 2015.

[164] K. Pyka, J. Keller, H. L. Partner, R. Nigmatullin, T. Burgermeister, D. M. Meier, K. Kuhlmann, A. Retzker, M. B. Plenio, W. H. Zurek, A. del Campo, and T. E. Mehlstäubler. Topological defect formation and spontaneous symmetry breaking in ion Coulomb crystals. *Nature Communications*, 4:2291, 2013.

[165] S. Ulm, J. Roßnagel, G. Jacob, C. Degnther, S. T. Dawkins, U. G. Poschinger, R. Nigmatullin, A. Retzker, M. B. Plenio, F. Schmidt-Kaler, and K. Singer. Observation of the Kibble-Zurek scaling law for defect formation in ion crystals. *Nature Communications*, 4:2290, 2013.

[166] T. W. B. Kibble. Topology of cosmic domains and strings. *J. Phys. A*, 9(8):1387, 1976.

[167] T. W. B. Kibble. Some implications of a cosmological phase transition. *Phys. Rep.*, 67(1):183–199, 1980.

[168] W. H. Zurek. Cosmological experiments in superfluid helium? *Nature*, 317(6037):505–508, 1985.

[169] R. Schützhold, M. Uhlmann, L. Petersen, H. Schmitz, A. Friedenauer, and T. Schaetz. Analogue of Cosmological Particle Creation in an Ion Trap. *Phys. Rev. Lett.*, 99(20):201301, 2007.

[170] N. C. Menicucci, S. Jay Olson, and G. J. Milburn. Simulating quantum effects of cosmological expansion using a static ion trap. *New J. Phys.*, 12(9):095019, 2010.

[171] C. Fey and R. Schützhold. Momentum dependence in the dynamically assisted Sauter-Schwinger effect. *Phys. Rev. D*, 85(2):025004, January 2012.

[172] C. Tsallis. *Introduction to Nonextensive Statistical Mechanics: Approaching a Complex World.* Springer Science & Business Media, 2009.

[173] C. R Calladine, H. Drew, B. Luisi, and A. Travers. *Understanding DNA: The Molecule and How it Works.* Academic Press, 3 edition edition, 2004.

[174] G. D. Rose and J. P. Seltzer. A new algorithm for finding the peptide chain turns in a globular protein. *Journal of Molecular Biology*, 113(1):153–164, 1977.

[175] W. Kabsch and C. Sander. Dictionary of protein secondary structure: pattern recognition of hydrogen-bonded and geometrical features. *Biopolymers*, 22(12):2577–2637, 1983.

[176] D. J. Barlow and J. M. Thornton. Helix geometry in proteins. *Journal of Molecular Biology*, 201(3):601–619, 1988.

[177] N. D. Socci, W. S. Bialek, and J. N. Onuchic. Properties and origins of protein secondary structure. *Phys. Rev. E*, 49(4):3440–3443, 1994.

[178] D. P. Yee, H. S. Chan, T. F. Havel, and K. A. Dill. Does Compactness Induce Secondary Structure in Proteins?: A Study of Poly-alanine Chains Computed by Distance Geometry. *Journal of Molecular Biology*, 241(4):557–573, 1994.

[179] C. Micheletti, J. R. Banavar, A. Maritan, and F. Seno. Protein Structures and Optimal Folding from a Geometrical Variational Principle. *Phys. Rev. Lett.*, 82(16):3372–3375, 1999.

[180] A. Maritan, C. Micheletti, A. Trovato, and J. R. Banavar. Optimal shapes of compact strings. *Nature*, 406(6793):287–290, 2000.

[181] Ahmed Shaikjee and Neil J. Coville. The synthesis, properties and uses of carbon materials with helical morphology. *Journal of Advanced Research*, 3(3):195–223, 2012.

[182] D. S. Su. Inorganic Materials with Double-Helix Structures. *Angewandte Chemie International Edition*, 50(21):4747–4750, 2011.

[183] K. L. Kohlstedt, F. J. Solis, G. Vernizzi, and M. O. de la Cruz. Spontaneous Chirality via Long-Range Electrostatic Forces. *Phys. Rev. Lett.*, 99(3):030602, July 2007.

[184] G. Vernizzi, K. L. Kohlstedt, and M. O. de la Cruz. The electrostatic origin of chiral patterns on nanofibers. *Soft Matter*, 5(4):736–739, 2009.

[185] S. Srebnik and J. F. Douglas. Self-assembly of charged particles on nanotubes and the emergence of particle rings, chains, ribbons and chiral sheets. *Soft Matter*, 7(15):6897–6905, 2011.

[186] H. Himura, H. Wakabayashi, Y. Yamamoto, M. Isobe, S. Okamura, K. Matsuoka, A. Sanpei, and S. Masamune. Experimental verification of nonconstant potential and density on magnetic surfaces of helical nonneutral plasmas. *Physics of Plasmas*, 14(2):022507, 2007.

[187] H. Himura, H. Wakabayashi, Y. Yamamoto, A. Sanpei, S. Masamune, M. Isobe, S. Okamura, and K. Matsuoka. Hot electron plasmas trapped in helical magnetic surfaces. *Hyperfine Interactions*, 174(1-3):83–88, 2007.

[188] V. N. Tsytovich, G. E. Morfill, V. E. Fortov, N. G. Gusein-Zade, B. A. Klumov, and S. V. Vladimirov. From plasma crystals and helical structures towards inorganic living matter. *New J. Phys.*, 9(8):263, 2007.

[189] P. Drude. *Lehrbuch der Optik.* University of Michigan Library, 1900.

[190] J. I. Tinoco and R. W. Woody. Optical Rotation of Oriented Helices. IV. A Free Electron on a Helix. *Journal of Chemical Physics*, 40:160–165, 1964.

[191] G. E. Desobry and P. K. Kabir. Optical Rotatory Power in a Classical One-Electron Model. *Am. J. Phys.*, 41(12):1350–1357, 1973.

[192] F. Dufey. Optical activity in the Drude helix model. *Chemical Physics*, 330(12):326–332, 2006.

[193] S. Yeganeh, M. A. Ratner, E. Medina, and V. Mujica. Chiral electron transport: Scattering through helical potentials. *The Journal of Chemical Physics*, 131(1):014707, 2009.

[194] R. Gutierrez, E. Díaz, R. Naaman, and G. Cuniberti. Spin-selective transport through helical molecular systems. *Phys. Rev. B*, 85(8):081404, 2012.

[195] A.-M. Guo and Q. Sun. Spin-Selective Transport of Electrons in DNA Double Helix. *Phys. Rev. Lett.*, 108(21):218102, 2012.

[196] S. Iijima. Helical microtubules of graphitic carbon. *Nature*, 354(6348):56–58, 1991.

[197] V. Y. Prinz, V. A. Seleznev, A. K. Gutakovsky, A. V. Chehovskiy, V. V. Preobrazhenskii, M. A. Putyato, and T. A. Gavrilova. Free-standing and overgrown InGaAs/GaAs nanotubes, nanohelices and their arrays. *Physica E*, 6:828–831, 2000.

[198] Y. K. Pang, J. Lee, H. Lee, W. Y. Tam, C. Chan, and P. Sheng. Chiral microstructures (spirals) fabrication by holographic lithography. *Optics Express*, 13(19):7615–7620, 2005.

[199] M. Zhang and J. Li. Carbon nanotube in different shapes. *Materials Today*, 12(6):12–18, 2009.

[200] Z. Ren and P.-X. Gao. A review of helical nanostructures: growth theories, synthesis strategies and properties. *Nanoscale*, 6(16):9366–9400, 2014.

[201] J. W. Mintmire, B. I. Dunlap, and C. T. White. Are fullerene tubules metallic? *Phys. Rev. Lett.*, 68(5):631–634, 1992.

[202] O. M. Yevtushenko, G. Ya. Slepyan, S. A. Maksimenko, A. Lakhtakia, and D. A. Romanov. Nonlinear Electron Transport Effects in a Chiral Carbon Nanotube. *Phys. Rev. Lett.*, 79(6):1102–1105, August 1997.

[203] O. V. Kibis, S. V. Malevannyy, L. Huggett, D. G. W. Parfitt, and M. E. Portnoi. Superlattice Properties of Helical Nanostructures in a Transverse Electric Field. *Electromagnetics*, 25(5):425–435, 2005.

[204] A. A. Grigor'kin and S. M. Dunaevskii. Electronic spectrum and ballistic transport in a helical nanotube. *Physics of the Solid State*, 49(3):585–590, 2007.

[205] O. V. Kibis and M. E. Portnoi. Semiconductor nanohelix in electric field: A superlattice of the new type. *Technical Physics Letters*, 33(10):878–880, 2007.

[206] O. V. Kibis and M. E. Portnoi. Superlattice properties of semiconductor nanohelices in a transverse electric field. *Physica E*, 40(6):1899–1901, 2008.

[207] O. V. Kibis. Dissipationless Electron Transport in Photon-Dressed Nanostructures. *Phys. Rev. Lett.*, 107(10):106802, 2011.

[208] M. C. Rechtsman, J. M. Zeuner, Y. Plotnik, Y. Lumer, D. Podolsky, F. Dreisow, S. Nolte, M. Segev, and A. Szameit. Photonic Floquet topological insulators. *Nature*, 496(7444):196–200, 2013.

[209] M. Bhattacharya. Lattice with a twist: Helical waveguides for ultracold matter. *Optics Communications*, 279(1):219–222, 2007.

[210] D. Reitz and A. Rauschenbeutel. Nanofiber-based double-helix dipole trap for cold neutral atoms. *Optics Communications*, 285(23):4705–4708, 2012.

[211] E. Vetsch, D. Reitz, G. Sagué, R. Schmidt, S. T. Dawkins, and A. Rauschenbeutel. Optical Interface Created by Laser-Cooled Atoms Trapped in the Evanescent Field Surrounding an Optical Nanofiber. *Phys. Rev. Lett.*, 104(20):203603, 2010.

[212] L. S. Levitov. Energetic Approach to Phyllotaxis. *Europhys. Lett.*, 14(6):533, 1991.

[213] C. Nisoli, N. M. Gabor, P. E. Lammert, J. D. Maynard, and V. H. Crespi. Static and Dynamical Phyllotaxis in a Magnetic Cactus. *Phys. Rev. Lett.*, 102(18):186103, 2009.

[214] J. Farey. On a curious property of vulgar fractions. *Philos. Mag.*, 47(217):385–386, 1816.

[215] J. K. Pedersen, D. V. Fedorov, A. S. Jensen, and N. T. Zinner. Quantum few-body bound states of dipolar particles in a helical geometry. *arXiv:1507.08138*, 2015.

[216] H. Lodish, A. Berk, C. A. Kaiser, M. Krieger, M. P. Scott, and A. Bretscher. *Molecular Cell Biology*. Freeman, W. H., New York, 6th edition edition.

[217] A. Vologodskii. *Topology and Physics of Circular DNA the Series*. CRC Press, 1992.

[218] N. V. Hud and I. D. Vilfan. Toroidal DNA Condensates: Unraveling the Fine Structure and the Role of Nucleation in Determining Size. *Annual Review of Biophysics and Biomolecular Structure*, 34(1):295–318, 2005.

[219] A. A. Simpson, Y. Tao, P. G. Leiman, M. O. Badasso, Y. He, P. J. Jardine, N. H. Olson, M. C. Morais, S. Grimes, D. L. Anderson, T. S. Baker, and M. G. Rossmann. Structure of the bacteriophage ϕ29 DNA packaging motor. *Nature*, 408(6813):745–750, 2000.

[220] R. Kovall and B. W. Matthews. Toroidal Structure of λ-Exonuclease. *Science*, 277(5333):1824–1827, 1997.

[221] K. Olsen and J. Bohr. Geometry of the toroidal N-helix: optimal-packing and zero-twist. *New J. Phys.*, 14(2):023063, 2012.

[222] N. Papasimakis, V. A. Fedotov, K. Marinov, and N. I. Zheludev. Gyrotropy of a Metamolecule: Wire on a Torus. *Phys. Rev. Lett.*, 103(9):093901, 2009.

[223] J. C. Eilbeck, P. S. Lomdahl, and A. C. Scott. The discrete self-trapping equation. *Physica D*, 16(3):318–338, 1985.

[224] M. Johansson, M. Hörnquist, and R. Riklund. Effects of nonlinearity on the time evolution of single-site localized states in periodic and aperiodic discrete systems. *Phys. Rev. B*, 52(1):231–240, 1995.

[225] A. J. Sievers and S. Takeno. Intrinsic Localized Modes in Anharmonic Crystals. *Phys. Rev. Lett.*, 61(8):970–973, 1988.

[226] D. K. Campbell, S. Flach, and Yu. S. Kivshar. Localizing energy through nonlinearity and discreteness. *Physics Today*, 57(1):43–49, 2004.

[227] P. G. Kevrekidis. *The Discrete Nonlinear Schrdinger Equation: Mathematical Analysis, Numerical Computations and Physical Perspectives.* Springer Science & Business Media, 2009.

[228] D. N. Christodoulides and R. I. Joseph. Discrete self-focusing in nonlinear arrays of coupled waveguides. *Opt. Lett.*, 13(9):794–796, 1988.

[229] A.A. Sukhorukov, Yu. S. Kivshar, H.S. Eisenberg, and Y. Silberberg. Spatial optical solitons in waveguide arrays. *IEEE Journal of Quantum Electronics*, 39(1):31–50, 2003.

[230] A. Trombettoni and A. Smerzi. Discrete Solitons and Breathers with Dilute Bose-Einstein Condensates. *Phys. Rev. Lett.*, 86(11):2353–2356, 2001.

[231] H. Hennig, J. Dorignac, and D. K. Campbell. Transfer of Bose-Einstein condensates through discrete breathers in an optical lattice. *Phys. Rev. A*, 82(5):053604, 2010.

[232] S. F. Mingaleev, P. L. Christiansen, Yu B. Gaididei, M. Johansson, and K. Rasmussen. Models for Energy and Charge Transport and Storage in Biomolecules. *Journal of Biological Physics*, 25(1):41–63, 1999.

[233] M. Peyrard and A. R. Bishop. Statistical mechanics of a nonlinear model for DNA denaturation. *Phys. Rev. Lett.*, 62(23):2755–2758, June 1989.

[234] M. Peyrard. Nonlinear dynamics and statistical physics of DNA. *Nonlinearity*, 17(2):R1, 2004.

[235] Yu. B. Gaididei, S. F. Mingaleev, and P. L. Christiansen. Curvature-induced symmetry breaking in nonlinear schrödinger models. *Phys. Rev. E*, 62(1):R53–R56, 2000.

[236] M. Ibañes, J. M. Sancho, and G. P. Tsironis. Dynamical properties of discrete breathers in curved chains with first and second neighbor interactions. *Phys. Rev. E*, 65(4):041902, 2002.

[237] S. Zdravković. Helicoidal Peyrard-Bishop model of DNA dynamics. *Journal of Nonlinear Mathematical Physics*, 18.

[238] P. G. Kevrekidis, S. V. Dmitriev, S. Takeno, A. R. Bishop, and E. C. Aifantis. Rich example of geometrically induced nonlinearity: From rotobreathers and kinks to moving localized modes and resonant energy transfer. *Phys. Rev. E*, 70(6):066627, 2004.

[239] S. Takeno, S. V. Dmitriev, P. G. Kevrekidis, and A. R. Bishop. Nonlinear lattices generated from harmonic lattices with geometric constraints. *Phys. Rev. B*, 71(1):014304, 2005.

[240] G. P. Berman and F. M. Izrailev. The Fermi-Pasta-Ulam problem: Fifty years of progress. *Chaos*, 15(1):015104, 2005.

[241] S. Lepri, R. Livi, and A. Politi. Heat Conduction in Chains of Nonlinear Oscillators. *Phys. Rev. Lett.*, 78(10):1896–1899, 1997.

[242] B. Hu, B. Li, and H. Zhao. Heat conduction in one-dimensional chains. *Phys. Rev. E*, 57(3):2992–2995, 1998.

[243] Yu. Li, S. Liu, N. Li, P. Hänggi, and B. Li. 1d momentum-conserving systems: the conundrum of anomalous versus normal heat transport. *New J. Phys.*, 17(4):043064, 2015.

[244] P. G. Wolynes and V. Lubchenko. *Structural Glasses and Supercooled Liquids: Theory, Experiment, and Applications.* Wiley, Hoboken, New Jersey, 1 edition edition, April 2012.

Eidesstattliche Versicherung

Hiermit erkläre ich an Eides statt, dass ich die vorliegende Dissertationsschrift selbst verfasst und keine anderen als die angegebenen Quellen und Hilfsmittel benutzt habe.

I hereby declare, on oath, that I have written the present dissertation by my own and have not used other than the acknowledged resources and aids.

Hamburg, den